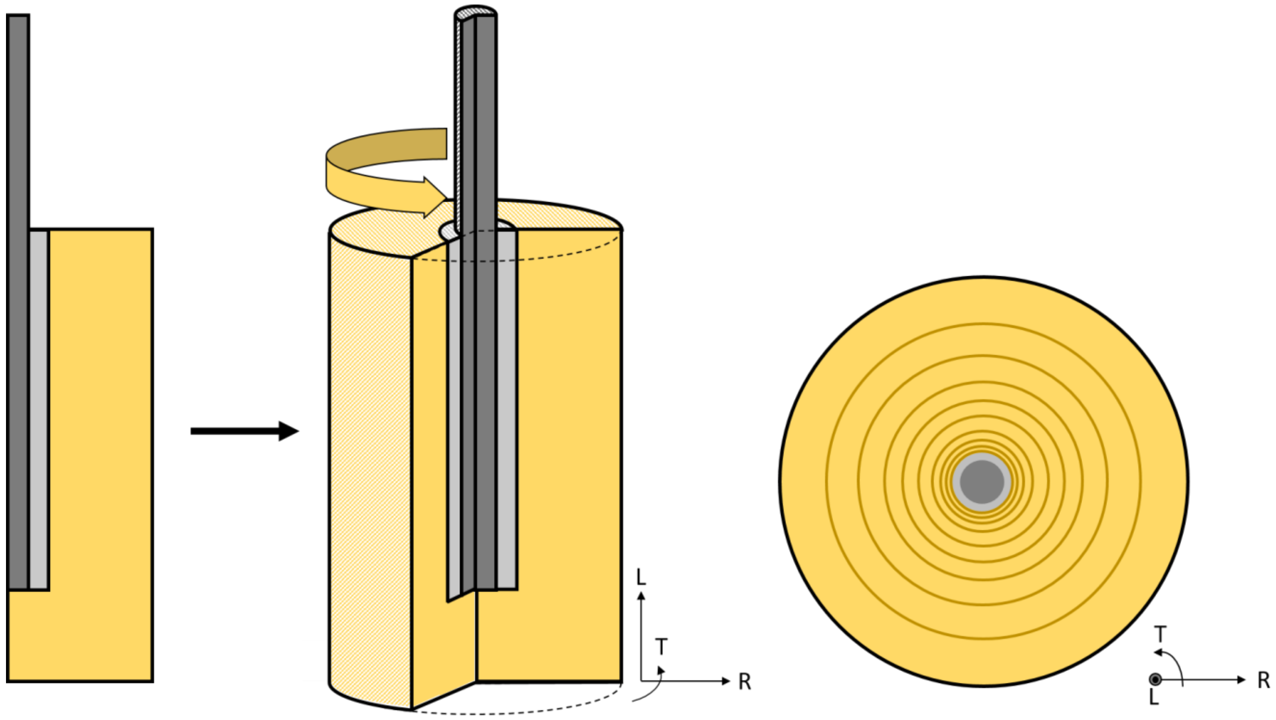

Glued-in Rods in Timber Structures

Finite Element Analyses of Adhesive Failure

Master's thesis in Structural Engineering

PER FELDT
AXEL THELIN

Department of Architecture and Civil Engineering
Division of Structural Engineering
Lightweight Structures
CHALMERS UNIVERSITY OF TECHNOLOGY
Master's Thesis ACEX30-18-20
Gothenburg, Sweden 2018

MASTER’S THESIS ACEX30-18-20

Glued-in rods in timber structures

Finite element analyses of adhesive failure

Master’s Thesis in the Master’s Programme Structural Engineering and Building Technology

PER FELDT

AXEL THELIN

Department of Architecture and Civil Engineering

Division of Structural Engineering

Lightweight Structures

CHALMERS UNIVERSITY OF TECHNOLOGY

Göteborg, Sweden 2018

Glued-in rod connections in timber structures
Finite element analyses of adhesive failure

Master's Thesis in the Master's Programme Structural Engineering and Building Technology

PER FELDT

AXEL THELIN

Examensarbete ACEX30-18-20
Institutionen för arkitektur och samhällsbyggnadsteknik
Chalmers tekniska högskola, 2018

Department of Architecture and Civil Engineering
Division of Structural Engineering
Lightweight Structures
Chalmers University of Technology
SE-412 96 Göteborg
Sweden
Telephone: + 46 (0)31-772 1000

Cover:
Conceptual overview of a glued-in rod, modelled on the basis of axisymmetry, see section 4.1.
Department of Architecture and Civil Engineering

Göteborg, Sweden, 2018

Glued-in rod connections in timber structures
Finite element analyses of adhesive failure
Master's thesis in the Master's Programme Structural Engineering and Building Technology

PER FELDT

AXEL THELIN

Department of Architecture and Civil Engineering
Division of Structural Engineering
Lightweight Structures
Chalmers University of Technology

Abstract

Using glued-in rods are generally seen as an efficient way to connect or reinforce timber elements. However, despite ongoing research since the 1980s, general and reliable design criteria for such connections are missing in the European standard for timber structures, Eurocode 5. Several design approaches have been proposed, but still no consensus has been reached on how to best evaluate the performance of glued-in rods.

The aim of this project was to effectively study how certain geometrical and material parameters affect the pull-out capacity of single rod connections. Ultimately, the purpose was to increase the knowledge of the load bearing capacity and mechanical behavior of glued-in rods, and contribute to an improved design approach.

The dominant failure mode for connections, glued with polyurethane or epoxy adhesives and loaded in axial tension, was identified as pull-out failure, in or near, the timber-adhesive interface. A finite element model, based on axisymmetry, describing timber-adhesive interface failure, was established, calibrated as well as verified against test results and numerical analyses found in literature. It was found that the axisymmetric analyses described the behavior of single glued-in rod connections accurately, and it was further concluded that numerical simulations, in a time efficient manner, predicted reliable results.

A parameter study was conducted, and the influence of axial stiffness ratio and geometrical length, on the load bearing performance, was studied. The results were compared with experimental data from literature, and an existing design recommendation, based on Volkersen (shear lag) theory, proposed by Gustafsson & Serrano (2002) was evaluated.

The results of the parameter study showed that the existing design proposal failed to accurately predict the load bearing capacity for epoxy-glued joints with short geometrical lengths. A modified version of the existing design recommendation was developed and analyzed. This modification yielded predictions of pull-out capacity on the safe side. Finally, the modification was simplified and ultimately proposed as a new design criterion for glued-in rods, shown to be valid for several adhesive types.

Keywords: Glued-in rod, Pull-out capacity, Adhesive, Finite element modelling, Axisymmetry, Numerical analysis, Parameter study, Design proposal

Contents

1 INTRODUCTION 1

- 1.1 Background 1
- 1.2 Aim and objectives 2
- 1.3 Scope and limitations 2
- 1.4 Method 3

2 REVIEW OF GLUED-IN ROD CONNECTIONS 4

- 2.1 Components and material properties of GiR connections 4
  - 2.1.1 Timber 4
  - 2.1.2 Steel 6
  - 2.1.3 Adhesive 6
- 2.2 Influence of geometrical parameters on the performance of GiR connections 7
- 2.3 Manufacturing GiR connections 8
- 2.4 Testing of GiR connections 9
- 2.5 Force transfer in GiR connections 10
- 2.6 Failure modes of GiR connections 12
- 2.7 Theories describing the behavior of adhesive bond lines in GiR connections 14
  - 2.7.1 Linear elastic stress analysis 14
  - 2.7.2 Linear elastic fracture mechanics 18
  - 2.7.3 Nonlinear and quasi-nonlinear fracture mechanics 19
- 2.8 Design of GiR connections 20

3 PREVIOUS TESTS AND EVALUATIONS IN LITERATURE 22

- 3.1 Experiments in literature 22
  - 3.1.1 Small-scale tests 22
  - 3.1.2 Full-scale tests 22
- 3.2 Finite element modelling in literature 24
- 3.3 Previous design proposal in literature 27

4 FINITE ELEMENT MODELLING 30

- 4.1 Description of the finite element models 30
- 4.2 Material models 33

5 VERIFICATION AND SENSITIVITY ANALYSIS OF THE AXISYMMETRIC FE MODEL 36

- 5.1 Influence of cohesive stiffness 36

5.2 Influence of mesh density 40
5.3 Influence of axisymmetry 45
5.4 Stress distribution and damage progression 47
5.5 Verification against previous studies 49
5.6 Discussion on the validity of the established axisymmetric FE model 51

6 PARAMETER STUDY 53
6.1 Results of numerical simulations 54
6.2 Discussion on parameter study 59

7 PROPOSED MODIFIED DESIGN EQUATION 61
7.1 Modified design equation 61
7.2 Simplification of modified design equation 63
7.3 Consideration of adhesive type 64
7.4 Discussion on the proposed design equation 66

8 CONCLUSIONS 68

REFERENCES 70

APPENDIX A – INVESTIGATION OF COHESIVE STIFFNESS 73

APPENDIX B – OVERVIEW OF MESH CONFIGURATIONS 81

APPENDIX C – DERIVATION OF CORRECTION FACTOR 82

Preface

This project was carried out at the Division of Structural Engineering, Department of Architecture and Civil Engineering between January 2018 and June 2018. We would like to thank our supervisor and examiner, Karin Lundgren, as well as our supervisor, Rasoul Atashipour. We are also grateful for the help and support received from Mohsen Heshmati, without whom, this project would have been very difficult to complete.

With this work, we conclude our time at Chalmers, a time that has been a rewarding and learning experience. This, however, does not mark the end of this beautiful friendship, as we will start working at the same office, coming fall. Thank you, to all the people that we have encountered during these special years.

Göteborg June 2018

Per Feldt & Axel Thelin

Axel Thelin

Notations

Roman upper case letters

A	Fracture area [m^2]
A_r	Rod cross-section area [m^2]
A_w	Timber cross-section area [m^2]
C	Bond line compliance [m/N]
E_r	Young’s modulus of rod [Pa]
E_w	Young’s modulus of timber [Pa]
G	Shear stiffness [Pa]
G_f	Fracture energy/ Energy release rate [J/m^2]
G_{fc}	Critical fracture energy [J/m^2]
K_n	Normal cohesive stiffness [Pa/m]
K_s	1st direction shear cohesive stiffness [Pa/m]
K_t	2nd direction shear cohesive stiffness [Pa/m]
P	External load [N]
$\underline{P}$	Unitless pull-out capacity [-]
P_f	Pull-out capacity [N]
P_r	Force acting on the rod section [N]
P_w	Force acting on the timber section [N]
T	Kinetic energy [J]
U	Total energy [J]
W	External work [J]

Roman lower case letters

a	Fracture progression [m]
d_h	Hole diameter [m]
d_r	Rod diameter [m]
f_v	Shear strength parameter [Pa]
k	Axial stiffness ratio [-]
l_a	Anchorage length [m]
l_{geo}	Geometrical length [m]
l_m	Material length [m]
t_b	Bond line thickness [m]
t_g	Glue line thickness [m]

t_n	Normal traction [Pa]
t_s	1st direction shear traction [Pa]
t_t	2nd direction shear traction [Pa]
u	Deformation [m]

Greek lower case letters

α	Coupling factor [-]
γ	Shear strain [-]
δ	Slip [m]
δ'_r	Axial deformation of the rod [m]
δ'_w	Axial deformation of the timber [m]
μ	Viscosity coefficient, Stabilization factor [-]
σ	Normal stress [Pa]
σ_f	Bond line normal strength [Pa]
τ	Shear stress [Pa]
τ_f	Bond line shear strength [Pa]
φ	Elastic energy [J]
ω	Stiffness ratio of a joint [-]
ϖ	Ratio of geometrical and material length [-]

1 Introduction

Building with timber has a long history in Sweden and many other countries. Traditionally, timber structures have been connected using old-school carpentry joints, dowels and nails. Today, there are numerous available connecting systems utilizing different techniques, suitable for different areas of application. One relatively new way of connecting timber is to use glued-in rods (GiR). By drilling holes in timber elements, they can be connected by inserting a rod, fastened with adhesive, thus creating an internal coupling, as shown in Figure 1.1.

Glued-in rods are generally seen as an efficient way of connecting timber elements in newly built structures, however they are also used to strengthen existing timber structures. Connections utilizing glued-in steel rods have gained popularity among designers since they provide high strength and stiffness in combination with efficient load transfer. Rods can be applied both parallel and perpendicular to the grain direction of the wood and, as long as they are fully covered by the surrounding wood, GiR connections provide good fire resistance and are generally perceived as aesthetically pleasing. Used as reinforcement, glued-in rods can effectively prevent tensile and shear cracking in tapered, curved or notched glulam beams (Tlustochowicz et al., 2011).

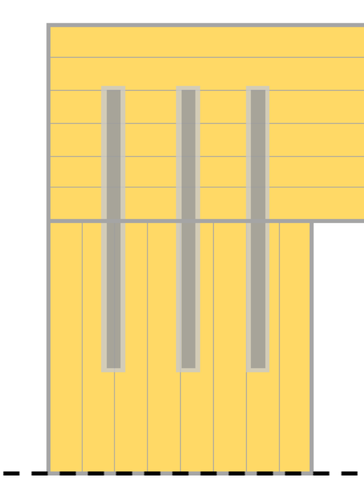

Figure 1.1 Glued-in rod connection between two timber elements.

Since glued-in rod connections utilizes the interaction between wood, adhesive and steel, there are several parameters that will influence its capacity. While geometry and material properties, of all components, will impact the performance, external factors such as loading condition, application method and surrounding environment will also affect the load bearing capacity of the connection (Stepinac et al., 2013).

1.1 Background

Research regarding glued-in rods have been ongoing since the 1980s, however, there seems to be no consensus in how to best design such connections and, as of today, a design criterion in the European structural standard, Eurocode 5, is missing (Tlustochowicz et al., 2011). Stepinac et al. (2013) elaborated on this problem further by stating that different design methods are currently in use in different European countries, but that there are some apparent variances, and sometimes contradictions, between them. According to Steiger et al. (2015), the lack of a general standard is primarily attributed to the large number of design approaches available, as well as the many parameters that impact the load bearing capacity of GiR connections.

Stepinac et al. (2013) also performed a survey where a questionnaire was answered by 56 respondents from 15 European countries. The group of respondents comprised of scientists, engineers and designers, as well as representatives from the timber industry. The purpose was to get an overview of the current popularity and knowledge of glued-in rods along with associated norms and regulations. The survey also treated the availability and quality of design methods. It was concluded, that there was a general dissatisfaction (89 % considered not satisfied) with the available design procedures among the respondents, thus further raising the need for a general-purpose European design criterion.

Furthermore, several issues were reported with the available design methods; one being the lack of reliable rules for multiple rod connections (Stepinac et al., 2013). Most design equations regarding pull-out capacity are instead derived from the behavior of single rod connections. This can be considered a problem and there is a need for a general approach regarding the design of multiple glued-in rods. On the other hand, there are still numerous issues left to study for single rod joints before a reliable design equation for multiple rod connection could be realized.

1.2 Aim and objectives

The purpose of this project is to increase the knowledge of load-bearing capacity and mechanical behavior of glued-in rod connections. More specifically, the aim is to find a way to effectively study the influence of certain geometrical and material parameters and their effect on the pull-out capacity of glued-in rod connections. This is broken down to several objectives:

- To perform a literature review of existing research to investigate which parameters are relevant for design and how they are considered in calculations of the pull-out capacity of GiR connections.

- To categorize different possible failure modes and identify the most important ones for the design of GiR connections.

- To establish a reliable and efficient method for finite element modelling of GiR joints which accurately predicts the pull-out capacity of single glued-in rods.

- To confirm the validity of the established modelling method by comparisons to tests and numerical evaluations in literature.

- To evaluate the accuracy of an existing design proposal with numerical analyses, by changing relevant parameters and study their impact on the pull-out capacity of glued-in rod connections.

Ultimately, this project aims to contribute to further research of GiR-connections in order to establish a reliable design model for future editions of Eurocode 5.

1.3 Scope and limitations

Glued-in rods are primarily used in timber structures as either connectors of structural elements or as reinforcement in areas where timber elements need to be strengthened due to high stress concentrations. This project mainly concerned the application of glued-in rods as connectors. Thus, no consideration was taken to the purely reinforcing aspects of GiR.

Since there are a large number of parameters affecting the load bearing capacity, the project was narrowed down to include joints in softwood, threaded steel rods as well as polyurethane and epoxy adhesives.

The study was limited to performance of single rod connections in axial loading; thus, the behavior of glued-in rods loaded in bending or shear was not investigated. The setup for the finite element model was limited to basic short-term loading under pull-pull conditions, constant indoor temperature and service class 1 and 2. Further, no consideration was taken to fatigue.

1.4 Method

A literature review was conducted in order to increase the knowledge regarding glued-in rods and to investigate which parameters are of special interest when designing GiR connections. Additionally, the mechanical behavior of glued-in rods was studied along with possible failure modes. This work was mainly conducted through reviewing research available in literature. As a part of the literature review, previous studies of experimental tests and numerical analyses of single rod connections were identified and later used as reference when establishing a numerical model.

An axisymmetric finite element model was established in the commercial finite element software Abaqus/CAE 2017 to run numerical analyses. The failure mode within the timber-adhesive interface was considered in the FE simulations. The reference studies were used for calibration of the FE model and results were compared in order to verify and ensure the validity of the model. The axisymmetric model was also compared with a 3D model to verify the accuracy of the former. After calibration, the influence of the defined parameters was investigated for single rod connections.

The numerically obtained pull-out capacities, for different geometrical setups, were compared with the predicted capacity of an existing analytical design equation, first presented by Gustafsson & Serrano (2002).

2 Review of glued-in rod connections

This chapter introduces the concept of glued-in rods as a timber-to-timber connector, its basic components, manufacturing principles, testing methods, force transfer, possible failure modes and theoretical approaches to describe the adhesive bond line. Additionally, a brief review of the issues with current approaches is presented.

2.1 Components and material properties of GiR connections

Glued-in rods are categorized as hybrid joints since they typically consist of three components: timber, rod and adhesive (Tlustochowicz et al., 2011). GiR connections are generally made with softwood construction timber, glulam or LVL (laminated veneer lumber). The rods can be applied either parallel or perpendicular to the grain direction of the timber.

The rods are often threaded and made from either steel or fiber-reinforced plastic (FRP). Steel is the most common material used; however, FRP is generally a preferred choice when there is high risk of corrosion or when lightweight constructions are desirable (Steiger et al., 2015). Rods or dowels made of hardwood can also be used, however these types of connections are not common and have mainly been researched and applied in Japan (Tlustochowicz et al., 2011).

In order to connect the rod to the timber there is a need of an adhesive. Over the last 30 years, several adhesive types have been used in GiR connections. Bengtsson & Johansson (2002) presented results of tests carried out on connections glued with three different types of adhesives – epoxy (EPX), phenol-resorcinol (PRF) and polyurethane (PUR). Out of those, EPX performed best regarding pull-out strength. According to Stepinac et al. (2013), PUR and EPX are the most commonly used adhesives in Europe.

The zone where the force is transferred between the two adherents (rod and timber), is generally referred to as "bond line", and includes the adhesive itself and the two interfaces between adherents and adhesive, see Figure 2.1. This zone is important when it comes to the design of GiR connections (Steiger et al., 2015).

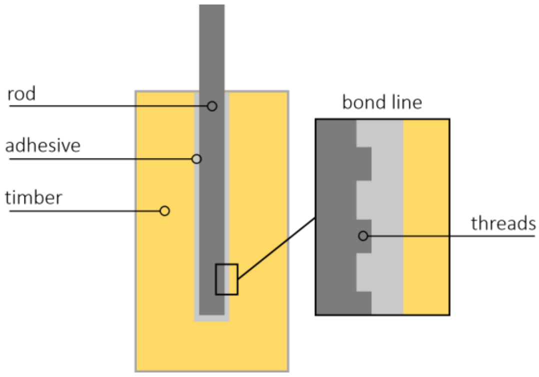

Figure 2.1 Different parts of a glued-in rod connection. A magnification of the bond line region is shown to the right.

2.1.1 Timber

The most common type of timber in Sweden is made from pine or spruce, i.e. softwood. Timber is an organic material with natural variations in properties such as density, strength, stiffness, moisture content, etc. Variations exist both between trees and within single trees. Timber is an orthotropic material which means that it has different properties in different directions (Svenskt Trä, 2013).

The strength of timber is dependent on the angle of the applied load, in relation to the grain direction, as well as the type of load. The compressive strength parallel to the grain is approximately 16 times greater than the strength perpendicular to the grain. In the case of tension, the strength parallel to the grain is approximately 30 times greater. Furthermore, the shear strength perpendicular to the grain is significantly higher compared to the shear strength parallel to the grain.

The stress-strain behavior of a material can be categorized as either ductile or brittle, and for timber, this depends on the type and direction of the applied load. The behavior of timber is generally characterized as brittle when loaded in tension or shear (Gonzalez et al., 2016) as opposed to the behavior when loaded in compression, which is considered to be more ductile (Danielsson, 2013). The response of timber for the different modes of stress and grain directions is shown in Figure 2.2.

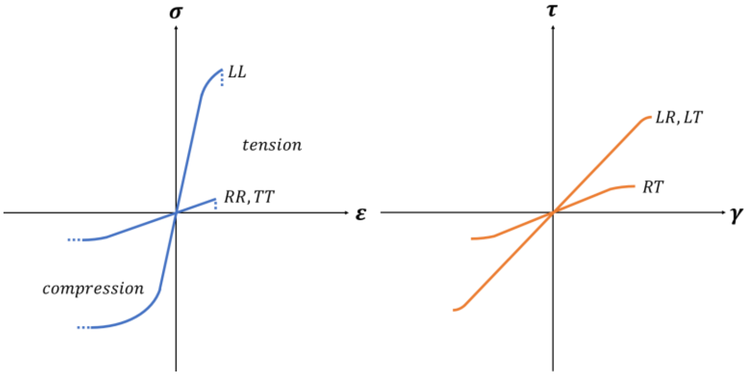

Figure 2.2 The stress-strain behavior of timber in different directions for normal stresses to the left and shear stresses to the right. L, R, T denotes the longitudinal, radial and tangential direction respectively.

To increase the performance of timber, engineered wood products such as laminated veneer lumber (LVL) and glued laminated timber (glulam) have been developed. The latter is produced by placing lamellas with the grain direction parallel to the length and gluing them together (Svenskt Trä, 2013), thus structural elements with less variations than ordinary sawn timber is attained (Svenskt Trä, 2016). LVL is manufactured by peeling logs of spruce into veneers and gluing them together under high pressure. The result is a product with similar characteristics as sawn timber but with smaller variation of properties and less defects (Francescato et al., 2005).

The material properties of the timber can have a large effect on the overall behavior of glued-in rod connections. The strength of the timber components is important with regards to performance and failure mode, where especially shear strength is of special interest (Steiger et al., 2015).

To what extent the density of the timber influences the strength of a GiR connection is not completely known, and opinions among researchers, seem to differ. Serrano (2001a) comments on the matter by stating that timber density can have threefold effect on the performance of a GiR connection. An increase in timber density is generally assumed to increase the strength of the timber, but a change in density could also mean that the adhesive properties between the adhesion and the timber change. Furthermore, a change in density could affect the stiffness of the timber which in turn can change the stress distribution in the glued-in rod connection. Tlustochowicz et al. (2011) elaborated on this further by stating that the influence of timber density is generally considered as a secondary effect, and that the associated effect on glued-in rod connections can counteract each other. Steiger et al. (2006) and Widmann et al. (2007) concluded that the effect of timber density on the pull-out capacity was more prominent for cases when the rod was glued-in parallel to the grain as opposed to perpendicular to the grain.

Variation in moisture content in the timber components can cause cracking as well as a rise in internal stresses. This is cited as the reason, along with some studied negative effects on the adhesive (see subsection 2.1.3), that glued-in rod connections in many design recommendations is not prescribed for usage in any other service classes than 1 and 2 (Tlustochowicz et al., 2011).

In addition to initial deformation, timber develops deformation over time and under constant loading. This effect is called creep and is a rheological property of the material. The creep deformation is highly dependent on the surrounding climate and develops logarithmically with time and approaches a final value which takes years to reach (Gowda et al., 1996).

2.1.2 Steel

On a macroscopic scale, and as opposed to wood, steel is considered an isotropic material, meaning that its mechanical properties are the same in all directions. Structural steel is generally considered ductile. Nevertheless, the rate of ductility, along with yield strength and ultimate strength, can differ significantly between different steel types. For example, a high strength, quenched alloy steel has considerably higher yield and ultimate strength than an ordinary carbon steel, while the latter exhibits a much more ductile behavior (Beer et al., 2012). This behavior is illustrated in Figure 2.3. A ductile failure mode is usually preferred when designing GiR connections, however a high strength steel is generally used in tests where it is of interest to provoke shear failure in the bond line or timber rather than failure of the rod itself (Steiger et al., 2006).

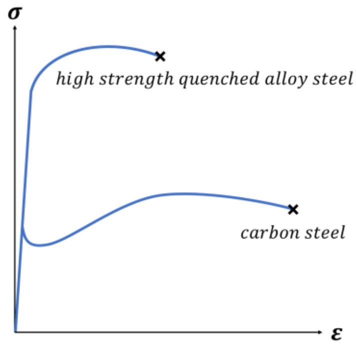

Figure 2.3 Stress and strain behavior for high strength steel (upper curve) and low strength steel (lower curve). Image reproduced from Beer et al. (2012).

2.1.3 Adhesive

The adhesive properties of a glue are dependent on several factors, partly on the viscosity and hardening of the glue substance itself, but also on the glue line thickness and the adhesion to the adherents (in this case timber and steel) (Tlustochowicz et al., 2011). According to Steiger et al. (2015), shrinkage may occur in the adhesive during the initial hardening and should be taken into consideration when designing GiR connections.

As stated in section 2.1, GiR connections can be made with several different types of adhesives, the most commonly used being epoxy (EPX) and polyurethane (PUR), where EPX generally demonstrates higher shear strength (Bengtsson & Johansson, 2002). It should be noted that EPX adhesives also develop a very strong attachment to both steel and wood. This means that the timber generally will be the weakest part of the connection, thus generating the fracture properties of the timber, or the interface between timber and adhesive, to become critical for the pull-out strength (Steiger et al., 2015). This is not always the case for PUR adhesives (Bengtsson & Johansson, 2002). PUR forms a strong bond like EPX, however when PUR is hardening, it absorbs water in the process and if the pressure is too low, the chemical reaction may result in formation of CO_2 bubbles. These bubbles usually form at the timber-adhesive interface which makes failure more likely to occur at this point (Serrano, 2001a). Both EPX and PUR generally demonstrate better gap-filling capabilities than more traditional timber adhesives such as phenol resorcinol (PRF), making them more appropriate for glued-in rod connections (Di Maria & Ianakiev, 2015). Furthermore, brittleness and ductility are important parameters regarding the characteristics of GiR connections. PUR is generally regarded as more ductile than EPX (Tlustochowicz et al., 2011).

The effect on different adhesives in glued-in rods, under the influence of moisture and elevated temperatures, was examined by Aicher & Dill-Langer (2001). Epoxy-based adhesives were found to be relatively unaffected when loaded in humid climate. This held true for both short and long-term loading. EPX showed a substantial loss of strength when exposed for temperatures above 50°C, while simultaneously being loaded. However, if no load was applied, the increase in temperature instead had a positive effect on the short-term strength, which was attributed to the adhesive's enhanced ability to post-cure. PUR did not perform as well when exposed to moisture or elevated temperatures above 40°C, and both the short and long-term strength decreased significantly.

The behavior of the adhesive is also closely interlinked with the glue-line thickness, which is categorized as a geometrical parameter (Tlustochowicz et al., 2011).

2.2 Influence of geometrical parameters on the performance of GiR connections

Many research projects, regarding the capacity of glued-in rod connections, have been focusing on the impact of different geometrical parameters; the most notable ones being: the anchorage length, diameter of rod and drilled hole, edge and rod-to-rod distance, as well as the direction of the applied load in relation to the grain direction of the timber member.

Steiger et al. (2006) investigated the influence of anchorage length and diameter of the drilled hole, along with timber density, in single rod connections, loaded in axial tension parallel to the grain. Experiments were conducted with samples of differing drill hole diameter and anchorage length. It was concluded that there is a positive correlation between pull-out capacity and an increase in anchorage length, but that the nominal shear strength of the connection decreases with increasing anchorage length. The ultimate load increased with increasing drill hole diameter, however, as no clear correlation between this diameter and nominal shear strength could be confirmed, the influence of drill hole diameter could not be properly evaluated.

The influence of edge distance, defined as the distance between the rod perimeter and the closest free edge of the timber body, has been investigated in several studies. According to Tlustochowicz et al. (2011), the recommendations on minimum edge distance is, in most cases, 2.5d, where d is the diameter of the rod. A study conducted by Steiger et al. (2006) observed that a smaller edge distance, resulted in a large decrease of the load bearing capacity caused by splitting of the wood. The recommendations on spacing between rods differ between 1.5*d* and 5*d* (Steiger et al., 2015). To avoid splitting of the wood between rods, recent studies have shown that a rod spacing of 5*d* is required (Gonzalez et al., 2016).

Tlustochowicz et al. (2011) also stated that the ultimate load generally increases with increasing rod diameter, but that the exact relationship between the two parameters is difficult to define. It is important, however, to distinguish between rod diameter and drilled hole diameter and to note that glue-line thickness also should be accounted for.

The glue-line thickness has been previously studied in several research projects. Tlustochowicz et al. (2011) claimed that it is problematic to draw any conclusions with regards to adhesive thickness only, since the strength is also dependent on adhesive type and properties. However, for EPX and PUR adhesives, there seems to be a slight increase in pull-out capacity when the glue-line thickness is increased up to 2 mm. For some adhesive types and with the glue-line thickness exceeding 3 mm, excessive stresses due to shrinkage may occur. It can also be said that a thicker glue-line generally means a more uniform stress distribution and a larger failure surface, assuming failure occurs in the interface between timber and adhesive.

Bengtsson & Johansson (2002) concluded that GiR connections exhibits higher strength when loaded parallel to the grain. This coincides with the typical behavior of timber, which is considerably stronger when loaded parallel to its grain direction. Conversely, a study performed by Widmann et al. (2007), came to a different conclusion after assessing the behavior of glued-in rod connections, loaded perpendicular to the grain. The results showed that the pull-out strength was 20-50 % higher when loaded perpendicular to the grain compared to when loaded parallel to the grain.

2.3 Manufacturing GiR connections

In the questionnaire conducted by Stepinac et al. (2013), one of the main reasons that GiR solutions sometimes are avoided, is the lack of manufacturing control and quality assessment. The level of expertise and knowledge needed for manufacturing GiR connections is, according to Stepinac et al. (2013), greater, compared to, for example, driving screws.

GiR connections can be built in different ways. The most common approach is to drill a hole into the timber which is 1 to 4 mm larger than the nominal diameter of the rod. After drilling, it is important that the hole is cleaned. This could be done by blowing pressurized air. According to Steiger et al. (2015), it is important that the air is free from oil-dust, since it negatively affects the load bearing capacity of the connection. A certain amount of adhesive is dispensed into the cleaned hole and the rod is inserted, see Figure 2.4a. The method´s disadvantage is the inability to ensure that the glue fills all the cavities (Steiger et al., 2015).

Further, Steiger et al. (2015) described an alternative approach, which is to drill one or two holes perpendicular to the main hole, where the rod is inserted. Adhesive is supplied via the perpendicular hole(s), and when adhesive is detected at the other opening, as shown in Figure 2.4b, the hole is filled. This approach can be applied for rods set both vertically and horizontally, as opposed to the more common one, which is only useful for rods set vertically. Tlustochowicz et al. (2011) suggests that some form of quality control should be applied to assure that the adhesive has filled all cavities.

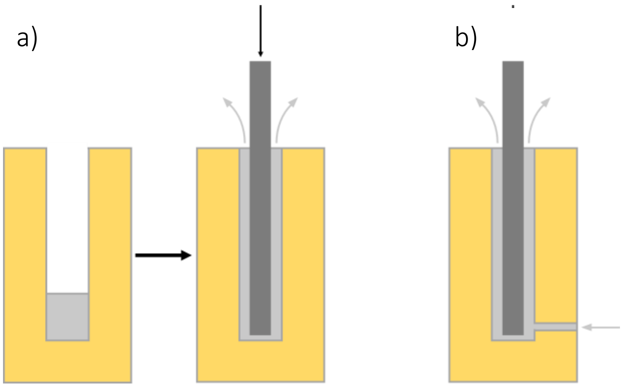

Figure 2.4 The most commonly used manufacturing approach (left) and the more controlled approach (right). Image reproduced from Steiger et al. (2015).

To obtain a good quality joint, the drilled hole should be straight and the rod placed in the middle of the hole to create an even adhesive thickness around the rod. The importance of cleaning the hole is stressed by Steiger et al. (2013); however, this is generally disregarded in practice (Tlustochowicz et al., 2011). The many parameters governing the quality of a finished GiR connection is difficult to assess during production, which makes glued-in rods a less used solution (Stepinac et al., 2013). Gonzales et al. (2016) came to a different conclusion, and stated that the orientation to the grain and centration of the rod, is of minor importance for the load bearing capacity and failure mode of the connection.

2.4 Testing of GiR connections

Most of the current knowledge regarding the mechanics and behavior of glued-in rod connections is derived from empirical experiments. When the load bearing capacity is tested, the axial pull-out capacity of the rod is measured. Even though single rod connections seldom are used in practice, most tests are carried out on single rod specimens, since it is regarded as an efficient way to isolate and investigate the influence of individual parameters. The boundary and loading conditions of the test setup, affect the results obtained. Depending on how the rod is placed in relation to the fiber direction, some setups are more suitable than others (Tlustochowicz et al., 2011).

In cases where the direction of the fiber and the rod coincide, a so-called pull–pull set-up is most common. In such an arrangement, the GiR connection is pulled from two sides, as can be seen in Figure 2.5a. An alternative approach, is the pull–compression configuration, in which the rod is pulled in one direction and the timber pressed in the opposite direction, see Figure 2.5b. The pull–compression setup is not a realistic loading condition (Tlustochowicz et al., 2011). According to Serrano (2001b), it also gives approximately 10-20 % lower pull-out strength compared to the more common pull-pull arrangement. The lowered capacity is explained by the setup, creating a more uneven shear stress distribution. Pull-compression tests can be performed, regardless of the angle between the grain direction and applied load.

The setup which reassembles reality the most, is the so-called pull–beam configuration, which can be seen in Figure 2.5c. The disadvantage with this set-up is that it demands a lot of material, as well as the issue of not knowing how much the pull-out strength is influenced by the bending stresses, caused in the test. An alternative test configuration, called pull–pile foundation, uses screws to distribute the compressive reaction forces within the wood, thus avoiding crushing of timber (Tlustochowicz et al., 2011), see Figure 2.5d. However, the simplicity of the pull-pull and the pull-compression set-ups, makes them the most commonly used test configurations.

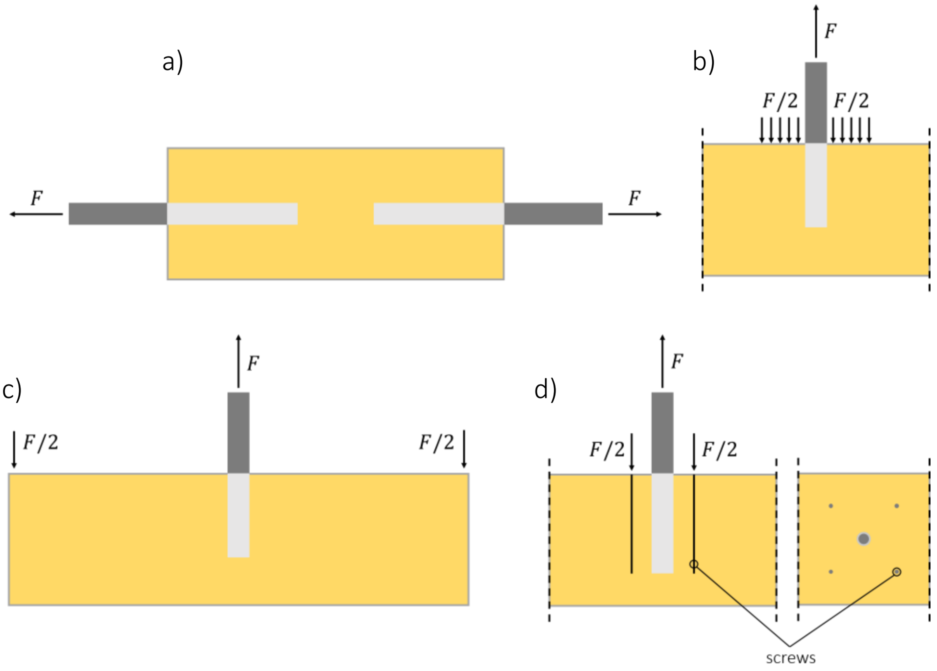

Figure 2.5 Different test setups: a) Pull-pull b) Pull-compression c) Pull-beam d) Pull-pile foundation. Image reproduced from Steiger et al. (2015).

2.5 Force transfer in GiR connections

An advantage with glued-in rod connections, is that the force transfer occurs internally, as opposed to several other timber connectors. In the rod, the force is transferred as normal stresses, however, the force transfer between the rod and the glue depends on the rod's surface. The surface of the steel rod can be either threaded, ribbed or smooth. Ribbed or threaded surfaces transfer the load as local normal compression stresses at the ribs or threads. Threaded rods are most commonly used in practice as they maximize the area of adhesion and increase the degree of mechanical interlocking (Tlustochowicz et al., 2011). Usage of smooth rods means that the force between the rod and the glue is transferred as shear stresses. In some design codes, it is regarded as insufficient to solely rely on the adhesive bond (Steiger et al., 2015). The force between the rod and the glue is generally seen as transferred either by compression or shear, however in some cases it is perceived as a combination of the two (Tlustochowicz et al., 2011).

The transfer of load through the adhesive layer as well as between the adhesive layer and the timber is governed by shear. The shear stresses have a non-uniform distribution which reach their maximum at the free surface and at the end of the anchorage zone, as can be seen in Figure 2.6 (Serrano, 2001b). The bond between the glue and the timber is seen as an adhesive bond. A study conducted by Di Maria & Ianakiev (2015) showed that a threaded wood surface of the hole, provided a slightly higher load bearing capacity compared to a smooth surface; the rough surface provides a larger surface area which reduces the shear stress, thus increasing the capacity of the joint.

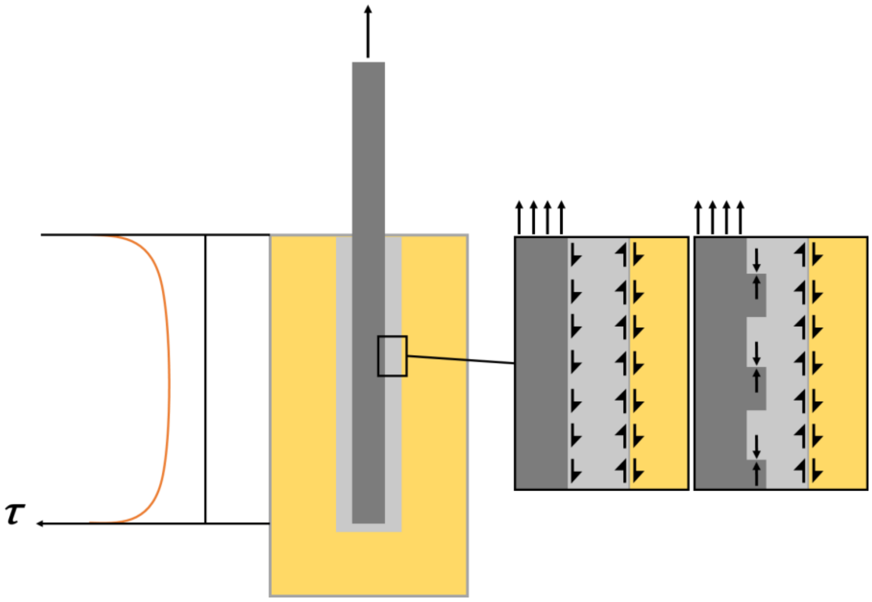

Figure 2.6 Bond line shear stress distribution along the anchorage length. The force is transferred by shear in the adhesive and between the adhesive and the timber, whereas there are two different means of understanding the force transfer between rod and the adhesive: shear or compression.

When a GiR connection is loaded in axial tension, the adhesive layer follows the rod outwards, thus creating stresses perpendicular to the rod. These stresses reach their maximum values at the bottom of the anchorage zone, and at the free surface, which is shown in Figure 2.7. These types of stresses are called peel stresses and affect the load bearing capacity of the connection (Gonçalves et al., 2014). The peel stresses in the adhesive, acts in compression in the bottom of the anchorage zone, and in tension near the free surface, while the stress directions in the timber are the opposite, thus acting in tension in the bottom of the anchorage zone and in compression near the free surface.

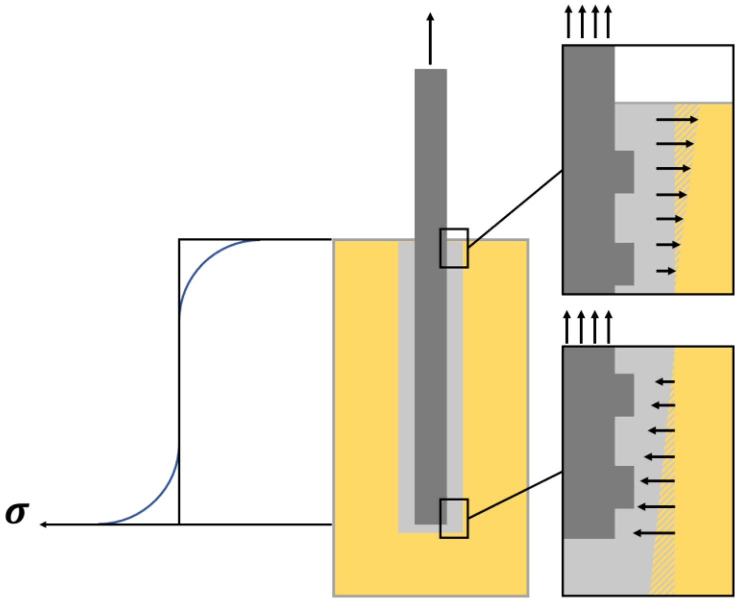

Figure 2.7 Bond line peel stress distribution along the anchorage length. The timber is subjected to compression close to the free surface and to tension at the bottom of the anchorage zone.

2.6 Failure modes of GiR connections

The mode of failure and the ultimate load bearing capacity of GiR joints are governed by the weakest part of the connection. Steiger et al. (2015) identified five possible failure modes for axially loaded single rod connections. All described failure modes are illustrated in Figure 2.8.

1. Rod failure: The steel rod can fail either by yielding (when loaded in tension) or by buckling (loaded in compression).

2. Pull-out of the rod: This failure mode is governed by the properties of the adhesive itself but also by the adhesion to the timber and steel:
    a. Compressive failure in the interface between steel rod and adhesive, due to crushing of the adhesive (for threaded rods), or shear failure (for smooth rods).
    b. Shear failure in the adhesive itself.
    c. Shear failure in the adhesive bond between adhesive and timber.
    d. Shear failure in the timber very close to the timber-adhesive interface.

3. Pull-out of wood plug: This failure mode occurs when the timber fails in shear parallel to the grain, resulting in the rod, along with a part of the timber, getting pulled out of the connection.

4. Splitting failure of the timber: Splitting failure generally occurs if the rod-to-edge distance is too small, or when loading is applied with an angle to the grain direction.

5. Tensile failure of the timber section: Tensile failure in the timber occurs just behind the glued-in rod, and is commonly occurring when the rod is inserted and loaded perpendicular to the grain direction.

Steiger et al. (2015) also outlined two additional failure modes for connections with multiple glued-in rods:

6. Group pull-out: Several rods, along with a block of wood, is pulled out from the connection due to shear failure in the timber body. This failure mode is also named “shear block failure”.

7. Splitting failure between rods: Splitting occurs between the rods and is due to too short rod-to-rod distance.

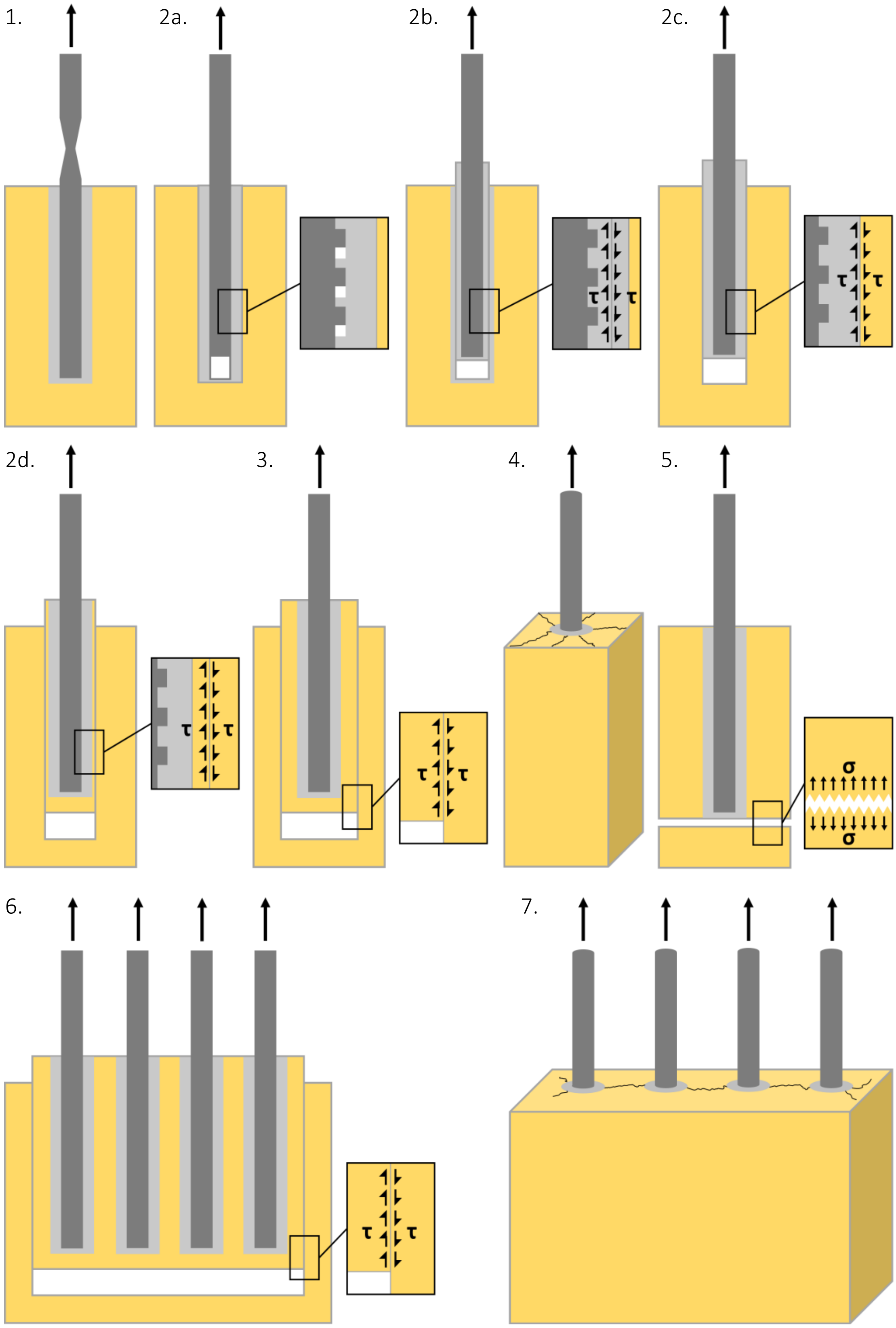

Figure 2.8 Possible failure modes for glued-in rod connections. Failure modes 1-5 are possible for single rod connections, failure mode 6 and 7 are possible for multiple rod connections.

While the probability of the occurrence of a certain failure mode might be difficult to assess, there are some studied relationships between specific failure modes and geometric setups. For example, failure modes 4 and 5, which describe splitting of timber and tensile failure of the timber section, are relatively easy to avoid if the provided edge distance and cross-sectional timber area are sufficient. Comparisons of design codes made by Stepinac et al. (2013), show that most codes have similar means of understanding of how to cope with these two failure modes. Additionally, the behavior of steel in tension is well studied, thus making failure mode 1 (yielding or buckling of steel rod) simple to predict.

Shear failure in, or in close proximity of, the bond line (failure mode 2, and to a certain degree, 3), which is connected to pull-out of the rod, is more complicated to describe and predict, since it depends on several parameters. While this failure mode is well studied, there seems to be a large discrepancy on how to approach it in design methods. As described in subsection 2.1.3, the weakest link of the bond line is located in, or in the vicinity of, the interface between adhesive and timber. Thus, the most common of the pull-out failures is the one occurring in the interface of timber and adhesive or within the timber itself (failure modes 2c and 2d).

2.7 Theories describing the behavior of adhesive bond lines in GiR connections

The bond line constitutes a critical element of glued-in rod connections, and the governing parameters for the behavior of the bond line are mainly the strength of the materials, the surface of the rod and the adhesive properties of the glue. As described in section 2.5, a non-uniform stress distribution will occur along the bond line. This stress distribution affects the pull-out capacity of a GiR connection, and can be taken into account by several different theoretical models, of which the most commonly used are described in this section.

2.7.1 Linear elastic stress analysis

In linear elastic stress analysis, the load bearing capacity of a glued joint is estimated by using a prediction of the stress and strain behavior. The pull-out capacity is assumed to be reached when the stress reaches a defined failure stress criterion (Steiger et al., 2015). In order to predict the stress distribution in a glued joint, one dimensional shear lag theory, first presented by Volkersen (1938), can be utilized. Based on Volkersen theory, linear elastic and isotropic behavior is assumed for the constituents of the joint. Further, the load transfer in the bond line is governed by shear only.

The initial mathematical model presented by Volkersen (1938), is valid for single lap glued connections. The following derivation is valid for circular glued joints, and could thus be applied on glued-in rods. Figure 2.9 illustrates the anchorage zone of a GiR connection, with the arbitrary length, l_a, from which the derivation of the pull-out capacity is made.

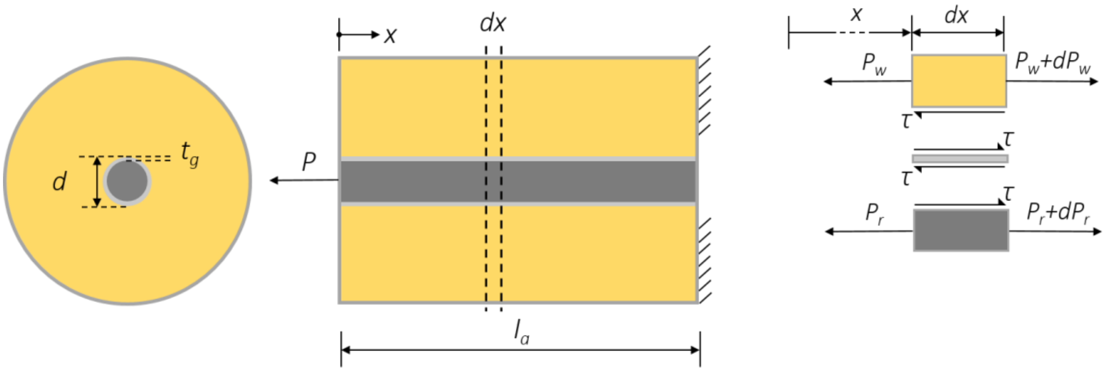

Figure 2.9 Cross-sectional views (from above and from the side) and a differential element of a single glued-in rod connection. With the help from the latter, an equation, describing the pull-out capacity, can be derived.

From the free body differential element of timber, an equilibrium equation can be derived as

$$P_w + dP_w - P_w - \tau \cdot d \cdot \pi \cdot dx = 0. \tag{2.1}$$

The equilibrium equation (2.1) is rewritten as

$$\frac{dP_w}{dx} = P_w' = \tau \cdot d \cdot \pi, \tag{2.2}$$

where τ is the shear stress in the adhesive, d is the rod diameter, dx the length of the differential element, and P_w the force in the timber. The expression for the rod is derived in a similar manner to

$$\frac{dP_r}{dx} = P_r' = -\tau \cdot d \cdot \pi = -P_w'. \tag{2.3}$$

The shear stress, τ, can be expressed in terms of the adhesive shear stiffness, G, and the shear strain, γ. Shear deformation can be rewritten as the axial displacement difference between the timber and rod:

$$\tau = G \cdot \gamma = \frac{G}{t_g} \cdot (\delta_w - \delta_r), \tag{2.4}$$

where the glue-line thickness is denoted by t_g, the axial timber deformation by δ_w, and the axial rod deformation by δ_r. The derivative of the axial strain in each part is given by the following equations:

$$\delta_w' = \frac{P_w}{E_w A_w}, \tag{2.5}$$

and

$$\delta_r' = \frac{P_r}{E_r A_r}. \tag{2.6}$$

By differentiating equation (2.4) and substitution from equations (2.5) and (2.6), one can obtain:

$$\tau' = \frac{G}{t_g} \cdot \left(\frac{P_w}{E_w A_w} - \frac{P_r}{E_r A_r}\right). \tag{2.7}$$

Differentiating equation (2.7) and replacing with equations (2.2) and (2.3), the following expression is obtained:

$$\tau'' = \frac{G}{t_g} \cdot \left(\frac{1}{E_w A_w} + \frac{1}{E_r A_r}\right) \cdot \pi \cdot d \cdot \tau. \tag{2.8}$$

By introducing the factor

$$\omega = \sqrt{\frac{G \cdot \pi \cdot d}{t_g}\left[\frac{1}{A_w E_w} + \frac{1}{A_r E_r}\right]}, \tag{2.9}$$

equation (2.8) can thus be expressed as

$$\tau'' - \omega^2 \cdot \tau = 0. \tag{2.10}$$

The general solution of this ordinary differential equation can be expressed as

$$\tau(x) = c_1 \cdot \cosh(\omega \cdot x) + c_2 \cdot \sinh(\omega \cdot x). \tag{2.11}$$

By integrating equation (2.11) over the whole anchorage length, l_a, the two equations of P_w and P_r are determined.

$$P_w = \frac{\pi \cdot d}{\omega} \cdot [c_1 \cdot \sinh(\omega \cdot x) + c_2 \cdot \cosh(\omega \cdot x)] + c_3 \tag{2.12}$$

$$P_r = \frac{\pi \cdot d}{\omega} \cdot [c_1 \cdot \sinh(\omega \cdot x) + c_2 \cdot \cosh(\omega \cdot x)] + \frac{E_w A_w}{E_r A_r} \cdot c_3 \tag{2.13}$$

Substituting P_w and P_r from equations (2.5) and (2.6), the axial deformations are attained as follows:

$$\delta_w = \frac{1}{E_w A_w} \cdot \left[\frac{\pi \cdot d}{\omega^2} \cdot [c_1 \cdot \cosh(\omega \cdot x) + c_2 \cdot \sinh(\omega \cdot x)] + c_3\right] + c_4 \tag{2.14}$$

$$\delta_r = \frac{1}{E_r A_r} \cdot \left[\frac{\pi \cdot d}{\omega^2} \cdot [c_1 \cdot \cosh(\omega \cdot x) + c_2 \cdot \sinh(\omega \cdot x)] + \frac{E_w A_w}{E_r A_r} \cdot c_3\right] - c_4 \tag{2.15}$$

From equations (2.12), (2.13), (2.14), and (2.15), it can be understood that four constants need to be determined from the boundary conditions; and consequently, the pull-out capacity can be obtained by equating the maximum shear strength and shear stress of the adhesive.

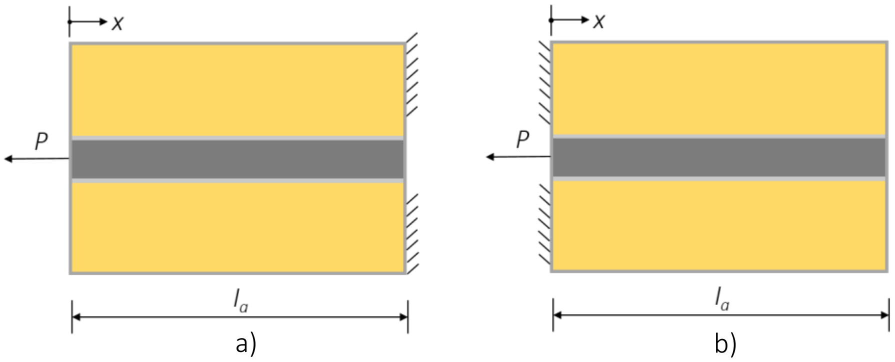

a) b)

Figure 2.10 a) Pull-pull load configuration, b) Pull-compression configuration.

The boundary conditions corresponding to the pull-pull load configuration are:

$$x = 0 \begin{cases} P_w = 0 \\ P_r = P \end{cases} \qquad x = l_a \begin{cases} \delta_w = 0 \\ P_r = 0 \end{cases}, \tag{2.16}$$

and the boundary conditions for pull-compression load configuration are:

$$x = 0 \begin{cases} \delta_w = 0 \\ P_r = P \end{cases} \qquad x = l_a \begin{cases} P_w = 0 \\ P_r = 0 \end{cases} \tag{2.17}$$

If the stiffness ratio $E_wA_w/E_rA_r > 1$, the maximum shear stress will occur at x=0. Using equation (2.11) and the boundary conditions of the joint, an expression for the maximum shear stress, τ^{max}, is obtained. By setting the maximum shear stress equal to the shear strength, τ_f, the ultimate load, P_f, can be attained.

For cases where the stress distribution along the glued length is relatively uniform (i.e. short glued lengths and ductile bond lines), meaning that the difference between maximum and minimum shear stress is small, a model based on linear elastic stress analysis can be utilized. However, for long glued lengths and brittle bond lines, the approach results in large stresses at the ends. The difference is illustrated in Figure 2.11. In reality, and as opposed to the prediction of a linear elastic stress analysis, these peak stresses do not necessarily result in failure of the joint. Thus, working with a stress based failure criterion can, for some cases, be inappropriate (Steiger et al., 2015).

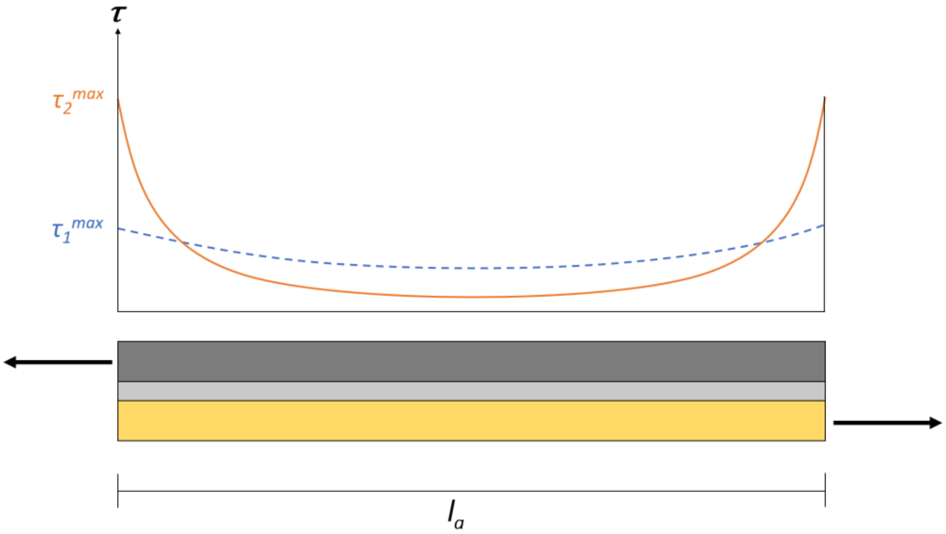

Figure 2.11 Shear stress distribution over an adhesive joint in accordance with the assumptions made in Volkersen's theory. The solid line represents a case with either long adhesive length or brittle bond line, where the maximum stress limit is denoted as τ_2^{max}. The dashed curve represents a case with short adhesive length or ductile bond line, where the maximum stress limit is denoted as τ_1^{max}. The areas under both stress distribution curves are assumed to be equal.

2.7.2 Linear elastic fracture mechanics

To be able to analyze glued connections where large end stresses occur, it is possible to approach the problem with linear elastic fracture mechanics (LEFM). The approach is generally based on energy release rate (fracture energy), G_f, which is defined as the amount of energy released by an infinitesimally small progression of an existing fracture area dA (Williams, 2001):

$$G_f = \frac{dU}{dA} = \frac{dW}{dA} - \frac{dT}{dA} - \frac{d\phi}{dA}, \tag{2.18}$$

where dU is the total energy change. The total energy is defined as different energy terms, then expressed as the work of the external load, W, the kinetic energy, T and the elastic strain energy, φ. When performing tests on specimens, the external and elastic energy change can be expressed as (Williams, 2001):

$$dW = P \cdot du \text{ and } d\phi = \frac{1}{2}[P \cdot du + u \cdot dP], \tag{2.19}$$

where P is the external load and u is the deformation. If the load is applied slowly during the test, the change in kinetic energy can be set as dT=0. Thus, the energy release rate can be expressed as

$$G_f = \frac{1}{2dA}[P \cdot du - u \cdot dP]. \tag{2.20}$$

During testing, it is possible to measure the compliance, *C(a)*, as a function of the crack progression, *da*. The compliance of the specimen is the inverse of the stiffness, and relates to the deformation and deformation change as

$$u = C \cdot P \text{ and } du = C(a) \cdot dP + P \cdot dC(a). \tag{2.21}$$

If the thickness, *B*, of the specimen is assumed to be constant, the fracture area change, *dA*, can be substituted by *dA=B·da*. When the energy release rate, G_f, is equal to the critical energy release rate, G_{fc}, illustrated in Figure 2.12, the load bearing capacity is assumed to be reached. Given equation (2.21) and the relation between fracture area and crack length, equation (2.20) can be rewritten as (Serrano & Gustafsson, 2006):

$$G_{fc} = \frac{1}{2}\left[\frac{P_f^2}{B}\right]\frac{dC(a)}{da}, \tag{2.22}$$

where P_f is the force it takes to start the crack propagation. Assuming the loading and boundary conditions are known, the maximum force can be solved from equation (2.22).

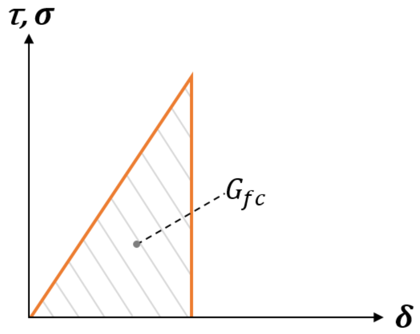

Figure 2.12 In LEFM, the stress-slip curve is limited by the fracture energy, i.e. the area under the curve. Image reproduced from Tlustochowicz et al. (2011).

In linear elastic fracture mechanics, failure is independent of stresses and is only limited by the critical energy release rate, G_{fc}. The approach assumes a linear elastic relation between the deformation and the fracture process of an already existing crack. This is not necessarily the real behavior but it is a reasonable assumption for brittle failures, which is the case for some adhesive joints (Williams, 2001). However, as an LEFM approach assumes that all supplied energy goes to propagation of an existing crack, and fails to consider that, in some cases, a large part of the energy is consumed by plastic deformations. This is the case for ductile adhesive bonds (Roylance, 2001).

2.7.3 Nonlinear and quasi-nonlinear fracture mechanics

As glued-in rod connections can continue to transfer load after the maximum allowed stress in some parts of the bond line has been reached, the two approaches described in subsection 2.7.1 and 2.7.2 do not offer entirely correct representations of real behavior. In order to more accurately assess the behavior of glued connections, a model based on nonlinear fracture mechanics (NLFM) can be used. Such a model takes into account the strain softening behavior and is, for glued joints, described by a stress limit and fracture energy of the bond line, see Figure 2.13. Since the approach is based on critical fracture energy, G_{fc}, and a stress criterion, related to τ_f and σ_f, NFLM provides the ability to analyze connections regardless if the expected behavior is brittle or ductile (Steiger et al., 2015). It is common to use nonlinear fracture mechanics when conducting numerical evaluations of adhesive joints.

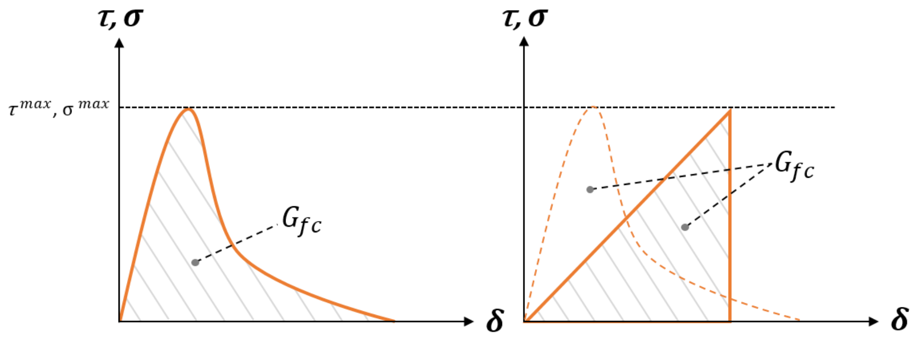

Figure 2.13 In NLFM, non-linear behavior is captured, and the stress-slip curve is limited by a stress limit as well as fracture energy. The simplification according to the quasi-nonlinear approach is illustrated to the right (Serrano & Gustafsson, 2006).

Quasi-nonlinear fracture mechanics is a theory that simplifies the general nonlinear fracture mechanics approach, and enables linear elastic analysis, but still accounts for both material strength and fracture energy, as well as deformation. The main principle is that an actual stress-slip behavior (τ-δ or σ-δ) is converted into a linear elastic relation, thus assuming that the load-bearing capacity is independent of the shape of the stress-slip curves (Serrano & Gustafsson, 2006). Analysis can subsequently be carried out by ordinary stress analysis, limited by both a failure stress criterion and prescribed fracture energy. This behavior is depicted in Figure 2.13.

In the case of glued-in rod connections, quasi-nonlinear fracture mechanics can be used to analytically describe the pull-out strength. This method was utilized, in combination with linear elastic stress analysis, by Gustafsson & Serrano (2002), when developing a calculation method, described in section 3.3.

Quasi-nonlinear simplifications might, however, not be suitable for numerical analysis. While a model based on quasi-nonlinear fracture mechanics offers some of the benefits of NLFM, it fails to realistically describe the stiffness in the elastic part of the stress-slip relation, as well the strain softening behavior, see Figure 2.13.

2.8 Design of GiR connections

Stepinac et al. (2013) summarized the evolution of design approaches regarding GiR connections. The first proposal for a design method was published by Riberholt in 1988 and included an equation for predicting the pull-out strength of axially loaded single glued-in rods, as well as recommended minimum values for edge distances. Experiments and further research was carried out during the 1990s, resulting in several different design approaches. In later years, several new research projects regarding the design of GiR connections have been launched and previous research have been revisited. Nonetheless, there is no general definition of how to best describe the behavior of glued-in rods, and an all-purpose design approach is still nonexistent.

Several design methods for single glued-in rods exist, but according to Stepinac et al. (2013), there is often a lack of cohesion between them. In some cases, different methods contradict each other and no consensus seems to exist over which theoretical design approach to use. Additionally, since the importance of different parameters and their effect on each other, and the pull-out strength, is not entirely investigated, it has been difficult to agree upon a general design approach.

According to Stepinac et al. (2013), most available design codes underestimate the pull-out strength of glued-in rods and can thus be considered safe. In later years, several new proposals for design equations have been published in scientific papers and in most cases, these equations predict a higher capacity.

Design equations for glued-in rods are almost exclusively formulated as criterions of pull-out strength where tension is applied axially. The main variable is generally agreed upon to be the shear strength of the connection, and the axial pull-out capacity of a single glued-in rod can according to Stepinac et al. (2013) be simplified as

$$P_f = \pi \cdot d \cdot l_a \cdot f_v, \tag{2.23}$$

where d is the diameter, l_a is the anchorage length and f_v is a shear strength parameter. Most proposed design criteria since the 1980s have been interpretations of this equation (2.23). However, and as previously stated, there is a disagreement on how to correctly define the relevant parameters. The diameter, d, can be defined as either diameter of rod, drilled hole or an equivalent diameter taking the threads of the rod into account. The anchorage length, l_a, can be described as either the part of the rod that is bonded or an equivalent length in which load transfer between the rod and the timber occurs.

The parameter that is perhaps most difficult to accurately describe, is the shear strength, f_v (Stepinac et al., 2013). This is due to a lack of consensus of which parameters that should be included in an expression describing this bond line strength. Additionally, previous research disagrees on whether the bond line strength should be described as the strength of the timber-adhesive interface, the strength of the adhesive itself or, in some cases, the shear strength of the timber.

3 Previous tests and evaluations in literature

This chapter presents previous work on glued-in rod connections, that has been used as comparison in this project. Three test series conducted on single glued in rod specimens, and one numerical evaluation method developed for GiR-connections, along with the latest proposal for a Eurocode design equation, were reviewed.

3.1 Experiments in literature

This section presents three test series performed in other projects: one small-scale test series which was used to capture fracture properties of the bond line, and two full-scale test series that investigated how different geometrical parameters affected the behavior of GiR connections. The data from the small-scale test was used to calibrate the finite element model established as part of this project, and the data from the full-scale tests was used for comparison and evaluation of the obtained results. Since this project only concerns connections glued with either PUR or EPX, results of tests performed with any other adhesive type is not presented.

3.1.1 Small-scale tests

Gustafsson & Serrano (2002) have conducted a series of tests with the aim to capture the fracture properties of the bond line for single rod connections, i.e. the fracture energies, as well as the shear and peel strengths of the bond line. They used small samples of softwood (strength classes C24 and C35), threaded steel bars and three different types of adhesives: PRF, PUR and EPX.

The testing has been conducted with a pull-pull configuration, with displacement controlled loading to capture the softening behavior of the specimens. They attained fracture properties for the connections from the stress-displacement curves obtained in testing. In order to obtain the specific bond line fracture properties for the peel and shear modes needed as input for finite element analyses, Gustafsson & Serrano (2002) changed the fracture properties until matching stress-displacement curves were obtained numerically. Values corresponding to samples glued with PUR and EPX are presented in Table 3.1.

Table 3.1 Input data for samples glued with PUR and EPX, obtained by numerically changing input to match the stress-slip curves (Gustafsson & Serrano, 2002).

	$G_{fc,s}$ [Nm/m^2]	τ_f [MPa]	$G_{fc,n}$ [Nm/m^2]	σ_f [MPa]
PUR	1200	11	400	4
EPX	2200	14	400	4

The failure modes occuring during the testing were reported to depend on which adhesive that had been used to join the rod and the timber. For PUR, all documented failures occurred within the adhesive itself, very close to the timber surface. For specimens glued with EPX, two different failure modes were documented. Some specimens failed in a similar manner as the PUR samples (i.e. failure in the adhesive very close to the timber), while some specimens instead failed in the timber very close to the adhesive (Gustafsson & Serrano, 2002).

3.1.2 Full-scale tests

Several tests on full scale joints have been conducted with the aim of providing data on how geometrical parameters influence the behavior of GiR connections. The results of the first test series presented in this section, were used as comparison and verification for the axisymmetric finite element model established, see chapters 4 and 5. The results from the second test series were used as reference data for the proposed design equation, see chapter 7.

Bengtsson & Johansson (2002) have presented results of several test series, one of which, performed at the Otto Graf Institute in Stuttgart, is described below. The results of this series have also been presented by Gustafsson & Serrano (2002). The tests have been conducted with a displacement controlled, pull-pull configuration. They used PRF, PUR and EPX adhesives as well as timber of strength classes C24 and C35, with a cross-sectional area of 120 x 120 mm^2. Threaded steel rods with a diameter of 16 mm and anchorage lengths of 160 and 320 mm have been used for testing of the bond line strength of joints glued with PUR and EPX. The drilled hole diameter of the tests was not reported. Joints glued with PRF were tested for three different anchorage lengths: 160, 320 and 640 mm. The results from the testing of samples with PUR and EPX are presented in Table 3.2.

Table 3.2 Values of ultimate load from the full-scale pull-pull tests. The tests were carried out on specimens with an anchorage length of 160 and 320 mm respectively. Polyurethane and epoxy was used as adhesives (Gustafsson & Serrano, 2002).

	PUR		EPX	
Anchorage length [mm]	160	320	160	320
Pull-out capacity [kN]	64.4	91.0	61.6	106.3

The failure modes of the different specimens generally corresponded to what was reported from the small-scale tests (presented in the previous section): all specimens glued with PUR failed in the adhesive, close to the timber-adhesive interface, while, for specimens glued with EPX, failure occurred either in the adhesive or the timber, very close to the timber-adhesive interface.

Another full-scale test series has been performed by Rossignon & Espion (2008), aimed to validate a certain production technique, created by the company Lamcol. They conducted the tests with pull-pull load configuration and used specimens made of glulam (GL24), with threaded steel rods and a two-component epoxy adhesive. The geometries for specimens with a rod diameter of 16 mm is presented in Table 3.3. The fracture input, provided by Rossignon & Espion (2008), for these specific connections, were $G_{fc,s}$=1890 J/m^2 and τ_f=10.5 MPa.

Table 3.3 The geometrical input for the specimens in the test performed by (Rossignon & Espion, 2008).

l_a [mm]	d_r [mm]	d_h [mm]	A_w [mm^2]	Steel grade	No. of tests
160	16	24	115x132	8.8	5
240	16	24	115x132	8.8	3
280	16	24	115x132	8.8	11
320	16	24	115x132	10.9	3
400	16	24	115x132	10.9	5

For steel rods with a diameter of 16 mm, a glue line thickness of approximately 4 mm was applied. The results of the tests are shown in Figure 3.1 and are presented as the mean shear stress, τ_{mean}, at failure, which corresponds to the ultimate load, P_f, divided by the surface bond area.

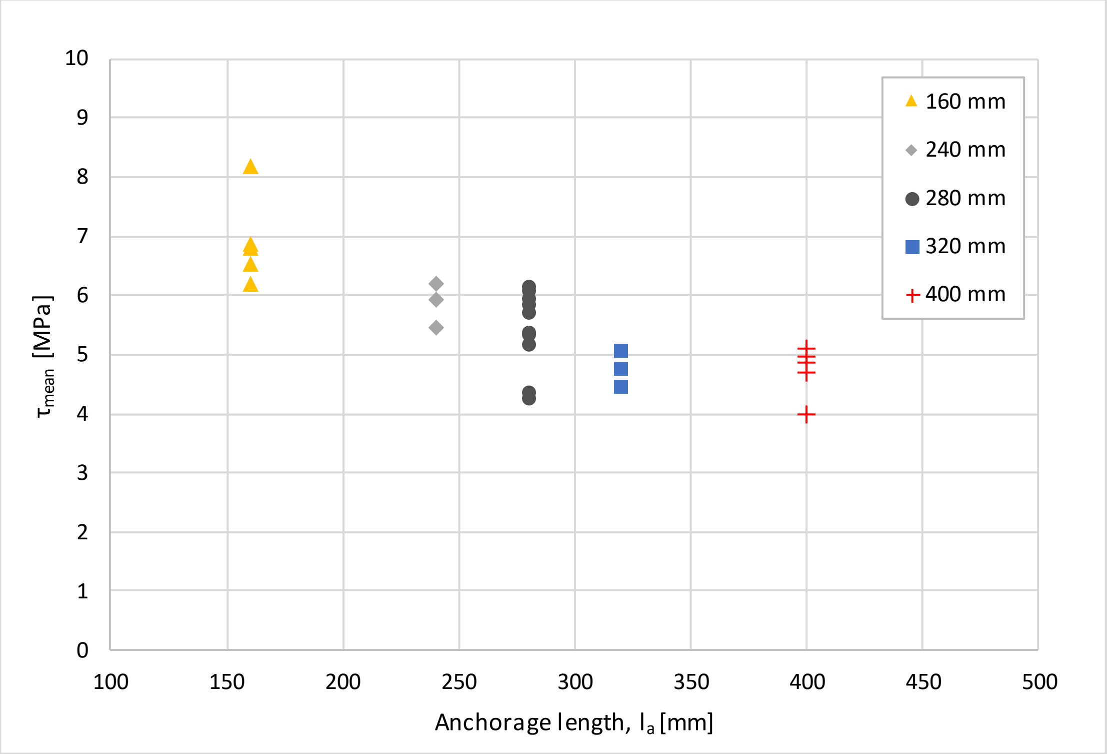

Figure 3.1 The results of the pull-pull tests by Rossignon & Espion (2008). The specimens were glued with epoxy.

Failure was reported to occur close to the timber-adhesive interface, either in the timber or in the adhesive. This tendency corresponds to the tested behavior of connections glued with EPX previously described.

3.2 Finite element modelling in literature

A method to numerically evaluate GiR connections have been developed by Serrano (2001b), with the aim to provide a basis for development of future design equations. The created model was implemented in Abaqus/CAE, and consisted of three parts: steel, timber and a bond line, modelled with 3D continuum elements. The geometry and boundary conditions Serrano (2001b) used for the model are illustrated in Figure 3.2. This model was later used by Gustafsson & Serrano (2002) for verification of the test series described in subsection 3.1.2.

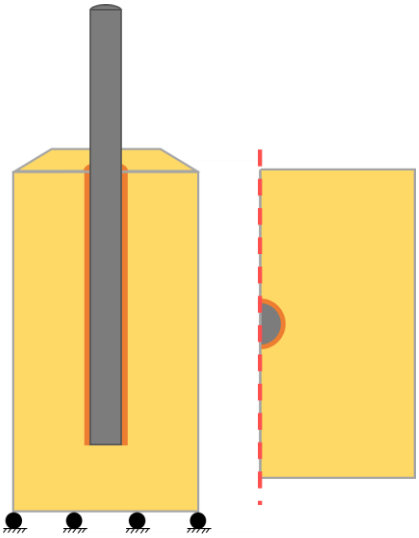

Figure 3.2 The geometry and boundary conditions of the finite element model developed by Serrano (2001b), seen from the side (left) and from above (right). The bottom is translationally locked and a symmetry condition is used to decrease the model size.

The model was limited to describe the failure and damage progression along the bond line. The steel and timber was modelled as linear elastic materials, with the difference that the steel was defined as isotropic and the timber as anisotropic. The bond line model was based on non-linear fracture mechanics and was an expansion of a theoretical model, previously presented by Wernersson (1994), which was created to evaluate timber-adhesive joints in 2D. While the original model considered one shear and one peel stress component, Serrano's development included an additional shear component. The shape of the three stress-slip curves for the bond line was simplified as a curve constituting of three lines, creating a linear representation of the elastic behavior and a bi-linear representation of the softening behavior. This is illustrated in Figure 3.3.

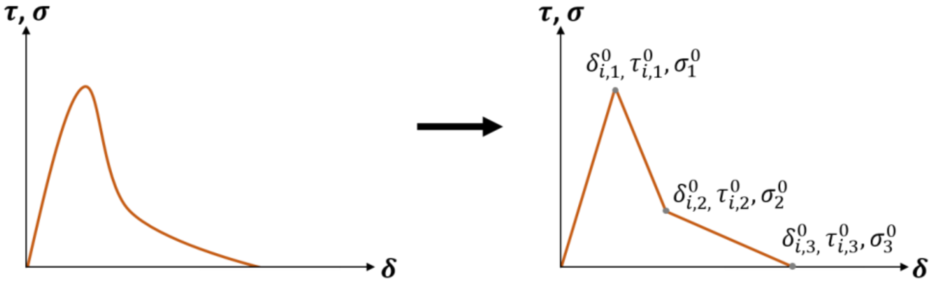

Figure 3.3 The simplification of the stress-slip curves used as input for the finite element model developed by Serrano (2001b) and used by Gustafsson & Serrano (2002).

The relations for the three stress components are formulated into one mixed mode deformation criterion, to decide if the stress state is within the elastic limit:

$$\left[\frac{\delta_{s1}}{\delta^0_{s1,1}}\right]^{m1} + \left[\frac{\delta_{s2}}{\delta^0_{s2,1}}\right]^{m2} + \left[\frac{\delta_n}{\delta^0_{n1}}\right]^{p} \leq 1, \tag{3.1}$$

where $\delta^0_{si,1}$ is the slip at the peak shear stress, $\tau^0_{i,1}$ and $\delta^0_{n,1}$ is the normal displacement for peak peel stress, σ^0_1. The slip at the corresponding shear stress, and normal displacement at the corresponding peel stress, is denoted as δ_{si} and δ_n, respectively. The factors *m1*, *m2* and *p* describe the coupling between the different fracture modes. If equation (3.1) is fulfilled, the existing stress state is within the elastic region, and the response can be directly interpolated for each stress component. If the state is beyond the elastic limit, the bi-linear softening behavior is assumed to keep its shape; however, the angle between the linear branches in a three-dimensional stress-deformation are assumed to change as following:

$$\varphi_{ss} = \arctan\left(\frac{\delta_{s1}}{\delta_{s2}}\right) \tag{3.2}$$

$$\varphi_{sn} = \arctan\left(\frac{\delta_{s}}{\delta_{n}}\right) \tag{3.3}$$

$$\delta_s = \sqrt{\delta_{s1}^2 + \delta_{s2}^2} \tag{3.4}$$

The following expressions define the critical fracture energies for the regarded modes of fracture, in terms of stress, associated deformation and bond line thickness, t_b:

$$G_{fc,s} = \int \tau_1^0 \cdot t_b \cdot \delta_{s1}^0 = \int \tau_2^0 \cdot t_b \cdot \delta_{s2}^0 \tag{3.5}$$

$$G_{fc,n} = \int \sigma^0 \cdot t_b \cdot \delta_n^0 \tag{3.6}$$

With these definitions, the complete behavior of the bond line is defined, and accordingly dependent on four parameters: the fracture energies for peel and shear, $G_{fc,n}$ and $G_{fc,s}$, and strength limits for peel and shear, σ_f and τ_f. If one of the conditions, prescribed by equations (3.5) or (3.6), are met, the material is assumed to be fully damaged and unable to transfer load further.

The results from the small-scale test, described in subsection 3.1.1, were used as input for the FE analyses performed by Gustafsson & Serrano (2002). The model geometry was then rebuilt to match the geometry of the test series for full scale testing in subsection 3.1.2. Further, the results obtained were compared with the full-scale test results, as can be seen in Table 3.4.

Table 3.4 The predicted pull-out capacities according to finite element simulations compared to full-scale test results, as presented by Gustafsson & Serrano (2002).

	PUR		EPX	
Anchorage length [mm]	160	320	160	320
Pull-out capacity, test [kN]	64.4	91.0	61.6	106.3
Pull-out capacity, FEM [kN]	67.1	93.8	89.2	118.7

Agreement between the numerical simulations and full-scale tests were found for PUR. For EPX however, the numerical simulations were overpredicting the capacity; a tendency that was most significant for the shorter anchorage length. This was attributed to the fact that failure in the tests of some EPX specimens, occurred in the timber close to the adhesive line, while the FE model assumed it to take place in the bond line.

3.3 Previous design proposal in literature

A design proposal has been developed by Gustafsson & Serrano (2002), presented on the 55th annual RILEM (International Union of Laboratories and Experts in Construction Materials, Systems and Structures) conference in Stuttgart, Germany in 2001. Their aim was to find a simple and general method, based on theory rather than experiments, and which takes both geometrical and material parameters into account.

Gustafsson & Serrano's (2002) calculation model was based on Volkersen's (1938) one dimensional shear lag theory as well as quasi-nonlinear fracture mechanics, see subsections 2.7.1 and 2.7.3, and thus presumes that the load bearing capacity is governed by shear. This calculation method is commonly referred to as "generalized Volkersen theory". The model assumes that failure of the connection occurs in the timber-adhesive interface, and that the pull-out capacity, P_f, is given by the shear strength, τ_f and critical shear fracture energy, $G_{fc,s}$, along with the axial stiffness of the two adherents, E_r (steel rod) and E_w (timber).

The result was an expression describing the ratio between the average shear stress at failure, $P_f/(\pi{\cdot}d_h{\cdot}l_a)$ and the bond line shear strength, τ_f.

$$\frac{P_f}{\tau_f \cdot \pi \cdot d_h \cdot l_a} = \bar{P}(\bar{\omega}, k) \tag{3.7}$$

The ratio, $\bar{P}$, is described as a function of the two parameters $\bar{\omega}$ and k, which in turn are defined as

$$\bar{\omega} = \omega \cdot l_a = \sqrt{\frac{l_{geo}}{l_m}} \tag{3.8}$$

$$k = \frac{E_r \cdot A_r}{E_w \cdot A_w}, \tag{3.9}$$

where l_{geo} is a length parameter, dependent on the geometry of the components as well as the stiffness ratio between the steel rod and the timber. The material property length parameter, l_m, is dependent on axial rod stiffness, E_r, and the bond line fracture properties. The two parameters, l_{geo} and l_m, can in turn be expressed as

$$l_{geo} = \frac{\pi \cdot d_h \cdot {l_a}^2}{2}\left(\frac{1}{A_r} + \frac{E_r/E_w}{A_w}\right) \tag{3.10}$$

$$l_m = \frac{E_r \cdot G_{fc,s}}{{\tau_f}^2}. \tag{3.11}$$

The expression for $\bar{P}(\bar{\omega},k)$, provides an understanding of how evenly the shear stresses are distributed along the bond line, and thus, how efficient the connection transfers load. Accordingly, $\bar{P}(\bar{\omega},k)$=1 means a completely uniform stress distribution, and that that the joint utilizes the maximum bond line shear strength over the whole bonding area when it fails. A lower value of $\bar{P}(\bar{\omega},k)$ means that the bond line shear strength only is utilized at some parts of the bonding area, while other parts have spare capacity when the joint fails. This is a general way of expressing the pull-out capacity in unitless form. Further, the expression for $\bar{P}(\bar{\omega},k)$ is formulated differently depending on how the GiR joint is loaded.

$$\frac{P_f}{\tau_f \cdot \pi \cdot d_h \cdot l_a} = \frac{\sinh(\omega) \cdot (1 + k)}{\omega \cdot (\cosh(\omega) + k)} \tag{3.12}$$

$$\frac{P_f}{\tau_f \cdot \pi \cdot d_h \cdot l_a} = \frac{\tanh(\omega)}{\omega} \tag{3.13}$$

$$\frac{P_f}{\tau_f \cdot \pi \cdot d_h \cdot l_a} = \frac{1 + k}{\omega/(\tanh(\omega) + k)} \tag{3.14}$$

Equations (3.12), (3.13) and (3.14) describe the unitless pull-out capacity for pull-pull, pull-compression and pull-distributed loading respectively. The difference in unitless pull-out capacity for the different loading conditions is illustrated in Figure 3.4. To keep the results on the safe side, Gustafsson & Serrano (2002) suggested that equation (3.13), corresponding to pull-compression loading, should be used for design of glued-in rods, since it predicts the lowest pull-out capacity. Additionally, this equation, is independent of the axial stiffness ratio, *k,* thus resulting in a simpler expression.

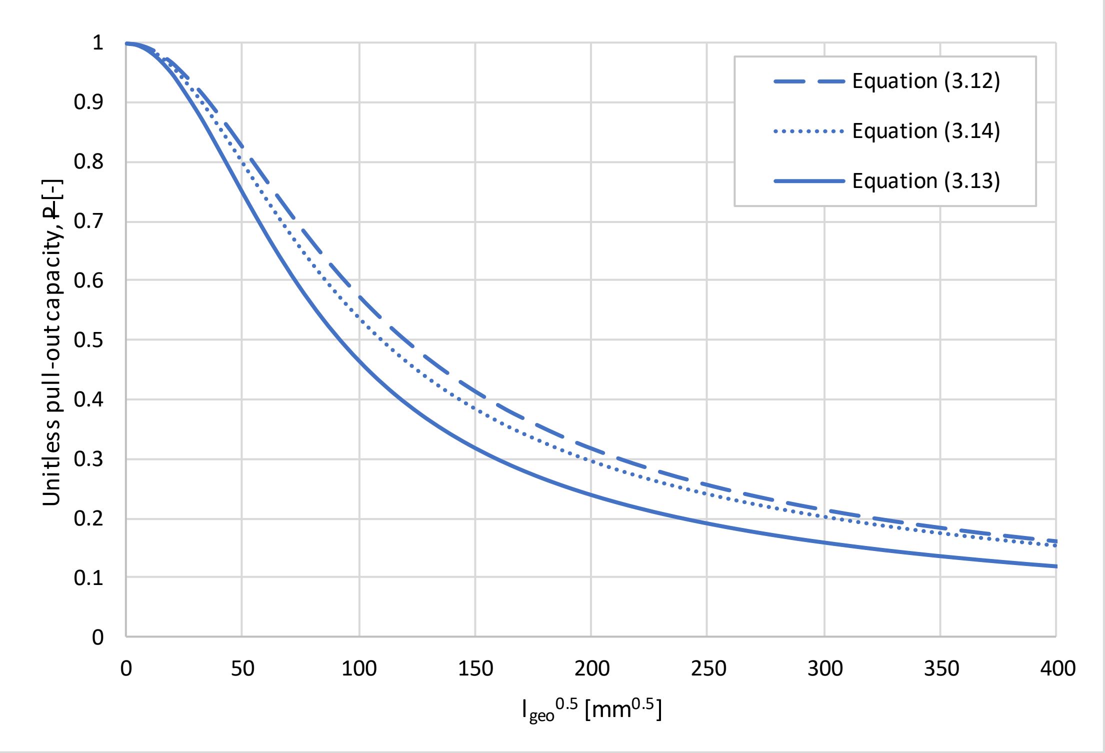

Figure 3.4 Comparison of the design equations presented by Gustafsson & Serrano (2002). Equation (3.12), (3.13) and (3.14) represents pull-pull, pull-compression and pull-distributed loading respectively. The input used to plot the curves is E_r=205 GPa, A_r=201 mm^2, E_w=11 GPa, A_w=11310 mm^2, d_h=17 mm, $G_{fc,s}$=1200 Nm/m^2, τ_f=11 MPa.

The pull-out strength, P_f, however, is dependent on the ratio of axial stiffness, and depending on the associated loading set-up, the ratio, *k*, affects the pull-out capacity differently. The effect is more evident for larger anchorage lengths and is schematically illustrated in Figure 3.5. While a higher stiffness ratio yields a higher pull-out strength, P_f, for pull-pull loading, the opposite effect is evident for pull-compression loading.

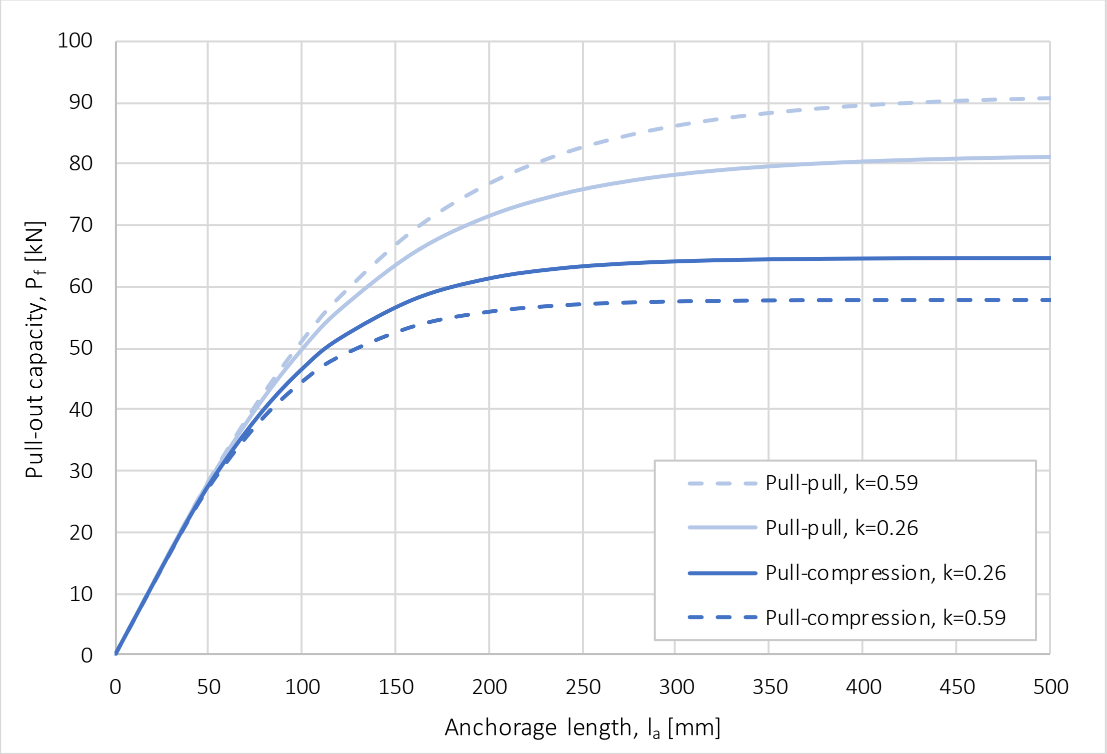

Figure 3.5 The influence of the rod-timber stiffness ratio, k, on the pull-out capacity, P_f, for different loading conditions (pull-pull and pull-compression) and anchorage lengths. The input data used to plot the curves is E_r=205 GPa, A_r=201 mm^2, E_w=11 GPa, d_h=17 mm, $G_{fc,s}$=2200 Nm/m^2, τ_f=14 MPa.

The proposed design model is valid for short time loading and constant climate and is possible to use for loading both parallel and perpendicular to the grain direction, where the pull-out strength perpendicular to the grain can be determined by using $E_w=E_{w,90}$ along with the relevant values for τ_f and $G_{fc,s}$ (Gustafsson & Serrano, 2002).

A simplified version of equation (3.13) was originally intended to be included in Annex C of Eurocode 1995-2:2004. However, it was decided in 2003 to put this design approach on hold since no consensus about it had been reached (Tlustochowicz et al., 2011).

4 Finite element modelling

One of the main objectives of this project, was to establish an effective method to predict the pull-out capacity of single glued-in rods. A two-dimensional axisymmetric model was created with the purpose of enabling fast modelling and evaluation of GiR connections and allowing for detailed analyses of bond-line failure during axial loading. Also, a three-dimensional solid model, as well as an additional axisymmetric model, were established as references. The finite element modelling was conducted in Abaqus/CAE. The models were created in such a way, that the acquired results could be compared to those of the FE model developed by Serrano (2001b) and the data presented by Gustafsson & Serrano (2002).

This chapter describes the three models, chosen material models and the simplifications that were made to be able to describe timber-adhesive interface failure.

4.1 Description of the finite element models

Timber is an orthotropic material and thus, a 3D solid model is a practical choice with regard to describing the properties dependent on material directions. However, the computational time required for numerical simulations with a model based on solid 3D elements is rather large. An axisymmetric model on the other hand, enables significantly faster simulation time. The concept of the two different models are shown in Figure 4.1 and Figure 4.2.

A quarter of the single rod connection was modelled for the 3D case, in order to reduce the simulation time, see Figure 4.1. However, the axisymmetric model was established and simulated in a two-dimensional domain, and subsequently extruded around a symmetry axis, see Figure 4.2.

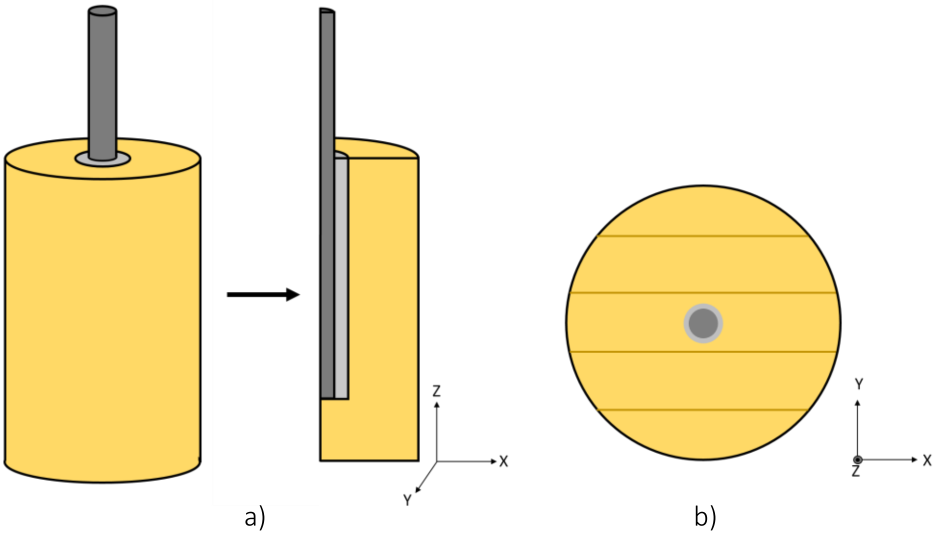

a) b)

Figure 4.1 a) Conceptual overview of the 3D model. Due to symmetry and in order to shorten the simulation time, only a quarter of a GiR connection was modelled, b) The defined directions of the timber properties as modelled in Abaqus/CAE.

The 3D model, illustrated in Figure 4.1, has different properties in the X, Y and Z directions. In Abaqus/CAE, the coordinate system can be changed to a cylindrical one. However, Serrano (2001b) studied the effect of ring curvature in numerical analysis with a 3D solid model and cylindrical coordinate system, and found that it had little effect on the results. Thus, for the 3D model used in this project, the properties in the different directions in the timber were assumed to be constant in the X, Y and Z directions, and accordingly modelled in a cartesian coordinate system.

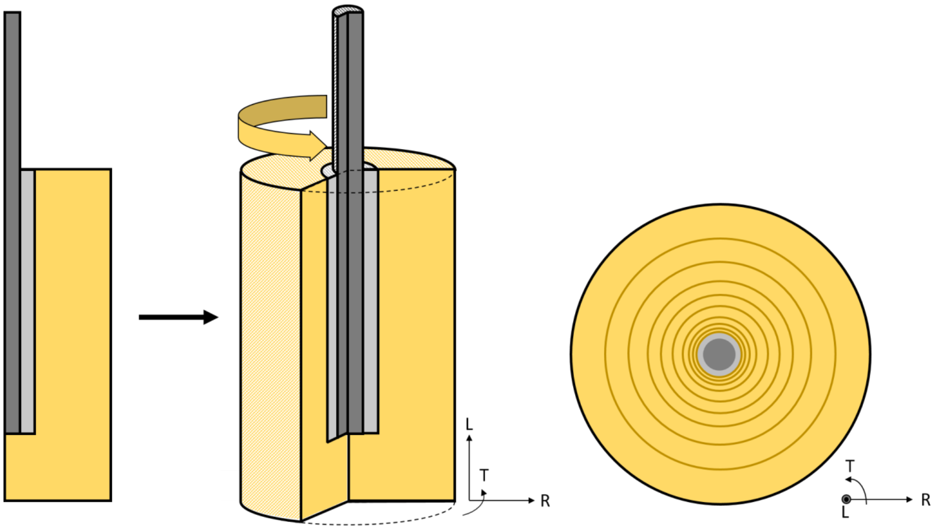

a) b)

Figure 4.2 a) Conceptual overview of the axisymmetric model. The two-dimensional plane and the extrusion around its symmetry axis, b) The defined directions of the timber properties as modelled in Abaqus/CAE.

The axisymmetric model, illustrated in Figure 4.2, assumes, that the properties vary in the longitudinal, radial and tangential directions. This condition assumes that the rod is placed centrically in a timber specimen with symmetric circular grains. The influence of this assumption was not known, however, since an axisymmetric model is significantly faster and less complicated to work with, it fitted the purpose of quickly and efficiently investigating the load bearing capacity of GiR connections.

As confirmed by the test results reported in section 3.1, the most commonly occurring failure in pull-pull loading, is failure in the region of the timber-adhesive interface. Thus, the finite element models established in this project aimed to simulate this specific failure. Accordingly, other failure modes were disregarded. A displacement controlled loading was used for both the 3D solid, and the axisymmetric model. A total displacement, u, of 2 mm was prescribed, and applied stepwise, as complete fracture in the bond line for both adhesive types, and for all investigated anchorage lengths, was predicted to take place at deformations smaller than 2 mm (Serrano, 2001a).

The boundary conditions of the models can be seen in Figure 4.3. Both models are locked with a symmetry line along the center line of the rod, as well as fixed at the bottom. Since the axisymmetric model is symmetric around its axis, it only needs one symmetry line along the rod's center. The 3D model has two symmetry lines, creating a quarter of a single glued-in rod connection. The fixed boundary in the bottom was initially motivated by potentially attaining more stable finite element analyses. The influence of this assumption was studied. Pull-out capacities for models with translationally locked bottom were compared with simulated capacities of models where the bottom was entirely fixed for any movement. It was shown that the difference was negligible (around 0.1 %). Thus, it was opted to continue working with a fixed bottom boundary condition.

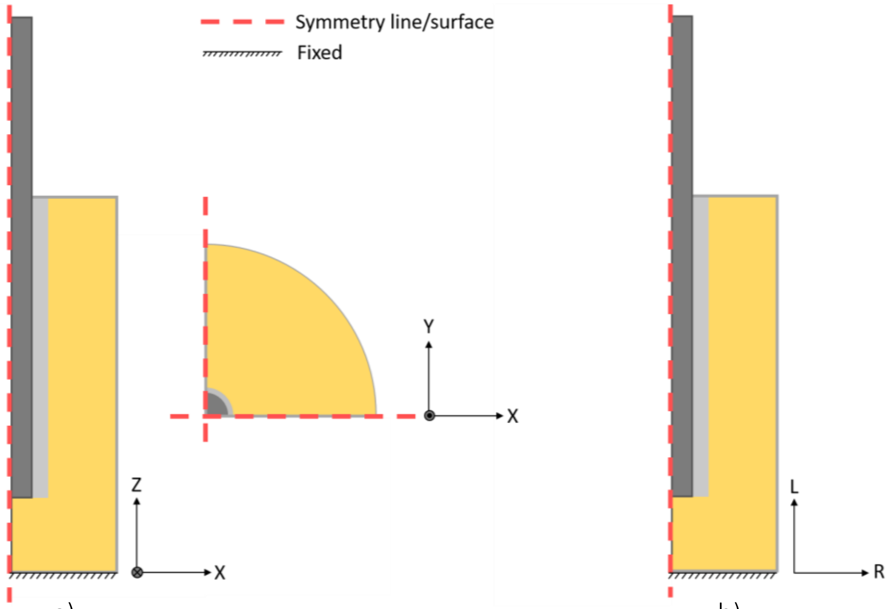

a) b)

Figure 4.3 a) The boundary conditions of the 3D model. Two symmetry lines creates a quarter of a glued-in rod connection, b) The boundary conditions of the axisymmetric model, with one symmetry line, along the center axis of the connection. Both models are fixed along the bottom

For the axisymmetric model, elements of the type CAX4R are used. For the 3D-model hexahedral elements of C3D8R are used. The 3D model's element type is an expansion of the axisymmetric element type.

The axisymmetric model consists of a steel rod, an adhesive layer and a thin row of cohesive elements, followed by timber. Due to convergence issues, the 3D case was modelled without an adhesive layer. Instead, this was replaced by a thicker row of cohesive elements, corresponding to the total adhesive layer thickness, as seen in Figure 4.4b). In order to make the axisymmetric and 3D models comparable, an additional axisymmetric model was established with the same bond line layering as the 3D model.

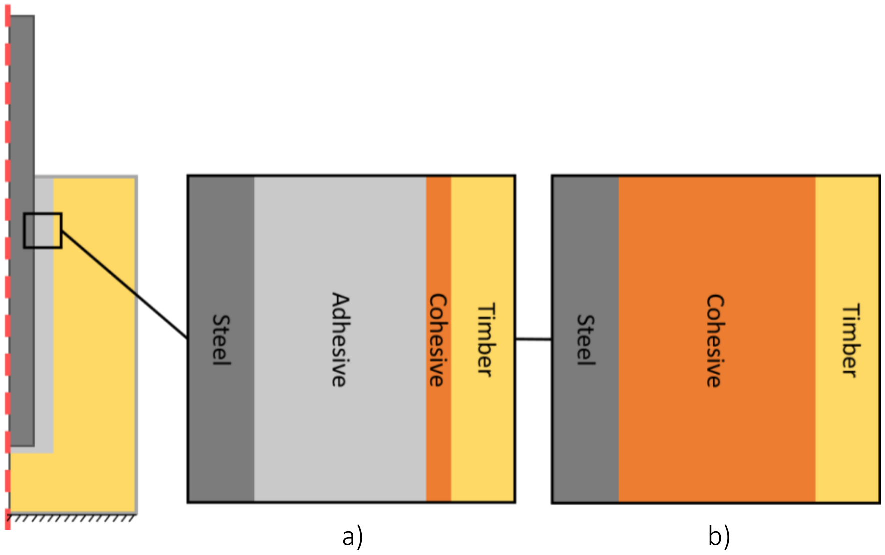

a) b)

Figure 4.4 The material layers of the different models. a) Bond line layer of the axisymmetric model, b) Bond line layers of the 3D and axisymmetric models, used for verification.

All the materials interact with tie constraints, as can be seen in Figure 4.5. This allowed for a finer mesh, close to the cohesive zone, which is important to attain reliable results (Heshmati et al., 2017). Furthermore, it also enabled a coarser mesh in the timber and rod, which reduces the computational time. The bottom of the rod was modelled as a free edge, due to the unknown behavior and material input for this zone. Additionally, it was also assumed to have little effect on the load bearing capacity.

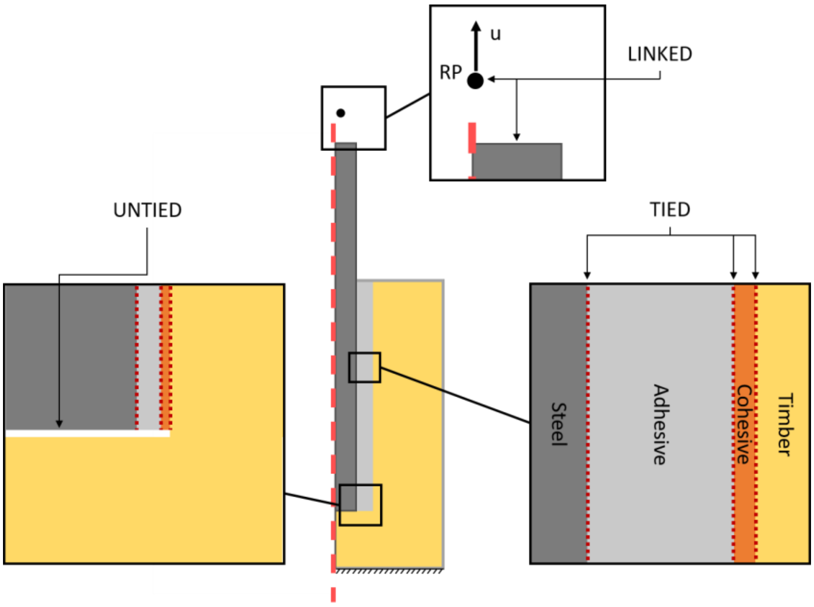

Figure 4.5 The interactions given in the axisymmetric model. The steel rod elements are tied to the adhesive, and the cohesive element row is tied to both the adhesive layer and the timber. The upper surface of the rod is tied to a reference point (RP) in which a displacement of u=2 mm is applied.

20 mm above the top surface of the rod, a reference point was placed; in which the prescribed displacement, *u*, was applied. The reference point was linked with the top surface of the rod, yielding equal displacement. This scheme allowed for easy extraction of load displacement data.

4.2 Material models

The steel and adhesive were given isotropic, linear elastic properties. However, the timber was given directional dependent, linear elastic, properties. For the axisymmetric model, these were given based on a cylindrical coordinate system, and for the 3D model, a cartesian coordinate system was used.

To describe failure of the timber-adhesive interface, a cohesive zone modelling (CZM) approach was used. In CZM, a crack's progression is simulated as a cohesive zone, where tractions are holding the surfaces together and as the separation of the surfaces increase, the tractions decrease until they become zero; this means that the surfaces are totally separated and the crack has progressed, which eventually will cause failure (Stigh et al., 2010).

The cohesive zone is modelled as a row of very thin (0.02 mm) elements which depend on a peel stress component and two shear stress components. The cohesive elements are defined by: an elastic behavior, a damage initiation criterion, a damage evolution model and a stabilization factor. The elastic behavior is defined by the stiffness of three modes: the normal cohesive stiffness, K_n, and the shear stiffness in two directions, K_s and K_t.

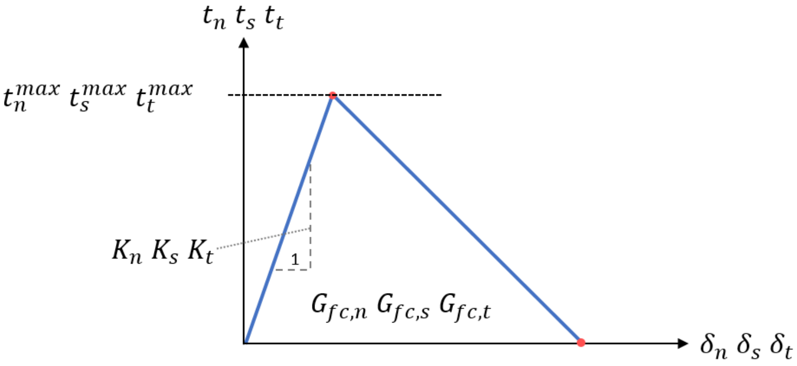

Figure 4.6 Definition of the stress-slip curves used in numerical simulations.

To determine whether a part of the material is damaged or not, the quadratic stress criterion (QuadS) in Abaqus/CAE was used (Dassault Systèmes, 2016). This criterion is defined as

$$\left[\frac{\langle t_n \rangle}{t_n^{max}}\right]^2 + \left[\frac{t_s}{t_s^{max}}\right]^2 + \left[\frac{t_t}{t_t^{max}}\right]^2 \leq 1, \tag{4.1}$$

where $\langle t_n \rangle$ is the normal tension traction, t_s and t_t are the tractions for each shear mode, t_n^{max}, t_s^{max} and t_t^{max} are the maximum possible tractions for respective mode. The finite element model, presented in section 3.2, uses a similar criterion, with the difference that the damage criterion depends on separations, instead of tractions. In the models established in this project, as well as in the model used by Serrano (2001b), the input for both shear modes are assumed to be equal.

When the quadratic damage initiation criterion is fulfilled, the damage evolution model determines the behavior of the bond line. The 3D and axisymmetric models were provided with an energy based, damage evolution model, with a linear softening response. The method developed by Serrano (2001b), described in section 3.2, uses a bilinear softening behavior and the difference is illustrated in Figure 4.7.

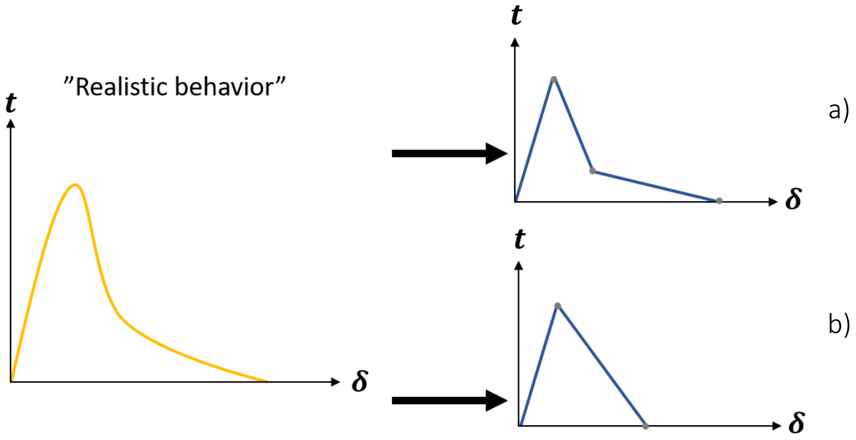

Figure 4.7 A stress slip-curve corresponding to "realistic behavior" compared to a), the simplification made by Serrano (2001b) and b), the simplification made in this project, according to the power law, see equation (4.2).

A mixed mode behavior was used, which follows an existing power law equation in Abaqus, which is as (Dassault Systèmes, 2016),

$$\left(\frac{G_{f.n}}{G_{fc,n}}\right)^{\alpha} + \left(\frac{G_{f,s}}{G_{fc,s}}\right)^{\alpha} + \left(\frac{G_{f,t}}{G_{fc,t}}\right)^{\alpha} = 1, \tag{4.2}$$

where $G_{f,n}$ is the normal fracture energy, $G_{f,s}$ and $G_{f,t}$ are the shear fracture energies, $G_{fc,n}$, $G_{fc,s}$ and $G_{fc,t}$ are the critical fracture energies for respective mode, and α is the coupling factor between the modes. The critical fracture energy is equal to the area under the traction-separation curves in Figure 4.7. When the criterion, defined by equation (4.2), is fulfilled, the material is fully damaged, and will be unable to carry load. The coupling factor α, affects how fast the material reaches the fully damaged state. The effect of this factor is illustrated in Figure 4.8. The lower value of the coupling factor, the faster the fully damaged state is reached, i.e. the more brittle the behavior becomes.

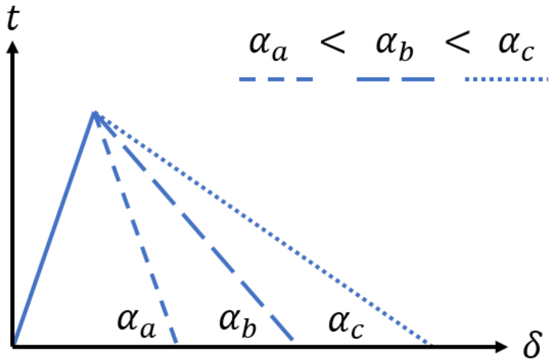

Figure 4.8 The impact of increasing the coupling factor. $\alpha_a < \alpha_b < \alpha_c$.

5 Verification and sensitivity analysis of the axisymmetric FE model

This chapter describes the process of calibrating and verifying the axisymmetric model presented in chapter 4.

5.1 Influence of cohesive stiffness

The cohesive stiffness values, K_n, K_s and K_t, as mentioned in section 4.2, describe the elastic behavior of the defined cohesive element row. The input values of these parameters affect the possibility of convergence as well as ultimate load. Thus, it was deemed important to investigate the effect of the adhesive stiffness input.

Heshmati et al. (2017) performed finite element modelling of glued FRP-steel joints, using a similar cohesive zone modelling approach. As a starting point in this work, input values from Heshmati et al. (2017) were used: K_n=3600 GPa/m and K_s=K_t=360 GPa/m for an adhesive with a Young's modulus of 7 GPa. In this work, cohesive stiffness values were scaled proportionally against the adhesive stiffness, 1.56 GPa for PUR, and 2 GPa for EPX. Thus, the cohesive stiffness values chosen as reference were K_n=800 GPa/m and K_s=K_t=80 GPa/m for PUR and K_n=1025 GPa/m, and K_s=K_t=102.5 GPa/m for EPX. These values are marked as "Reference" in Table 5.1. In order to investigate their effect on the numerical simulations, the different values of cohesive stiffness were changed, while the rest of the input was kept constant. This procedure was carried out for two anchorage lengths: 160 mm and 320 mm.

Table 5.1 Overview of cohesive stiffness values of the different simulations.

Simulation	Normalized cohesive stiffness (NCS)	PUR	EPX
		K_n, K_s [GPa/m]	K_n, K_s [GPa/m]
1	0.05	40, 4	50, 5
2	0.25	200, 20	260, 26
3	0.5	400, 40	510, 51
4	0.75	600, 60	770, 77
Reference	1	800, 80	1030, 103
5	1.25	1000, 100	1280, 128
6	1.5	1200, 120	1540, 154
7	1.75	1400, 140	1800, 180
8	2	1600, 160	2050, 205
9	2.5	2000, 200	2560, 256
10	3	2400, 240	3080, 308
11	4	3200, 320	4100, 410
12	6	4800, 480	6150, 615
13	8	6400, 640	8200, 820
14	10	8000, 800	-

The results from the investigation for PUR adhesive and an anchorage length of 160 mm are shown in Figure 5.1 and Figure 5.2. For cohesive stiffness 1.25-2.5 times greater than the reference values, the difference in pull-out capacity between the simulations is small, and lies within the range of 1.8 kN, which is less than 3 %.

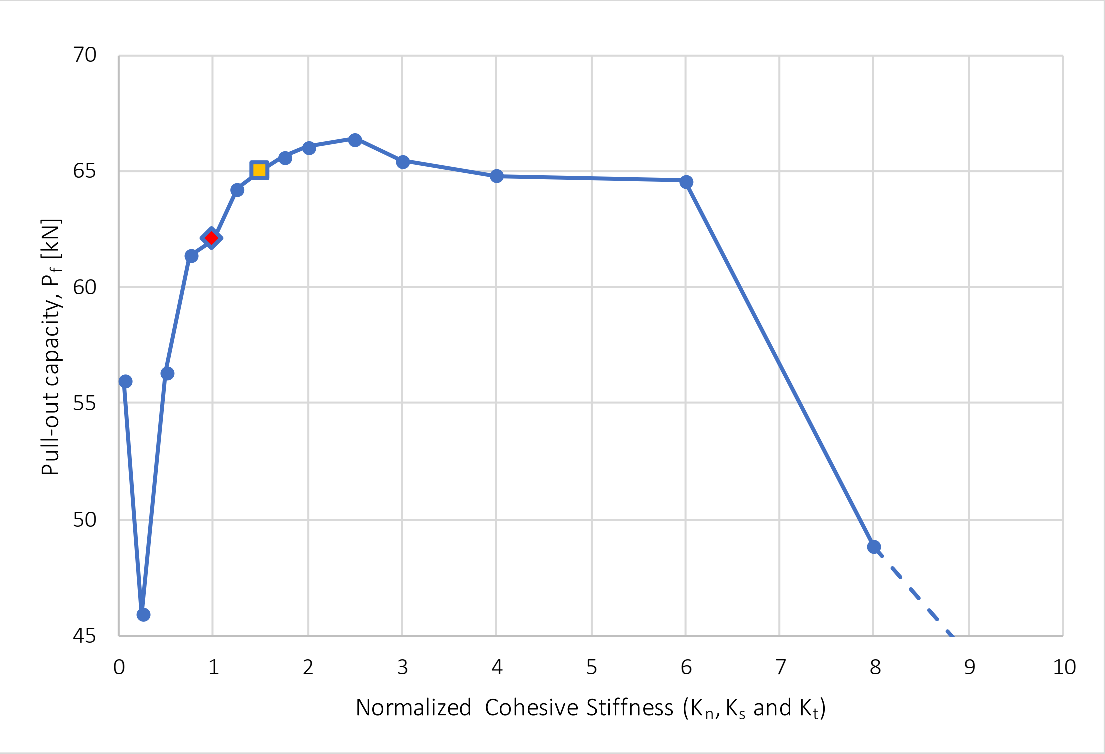

Figure 5.1 The predicted pull-out capacity vs normalized cohesive stiffness for PUR with an anchorage length of 160 mm. The reference case is marked by a red diamond. The simulation corresponding to the chosen normalized cohesive stiffness of 1.5 times the reference value is marked by a yellow square.

For cohesive stiffness three times the reference values or higher, the model starts to exhibit a non-converging behavior. This is visible in Figure 5.2, and is further highlighted in Figure 5.3, where it is evident that the simulations, corresponding to normalized cohesive stiffness (NCS) 3.00 and higher, stop at a load, greater than the previous step. Thus, for these cases, it is not known if the maximum load has been reached. Furthermore, for larger cohesive stiffness values, the overall stiffness of the joint is less and less affected.

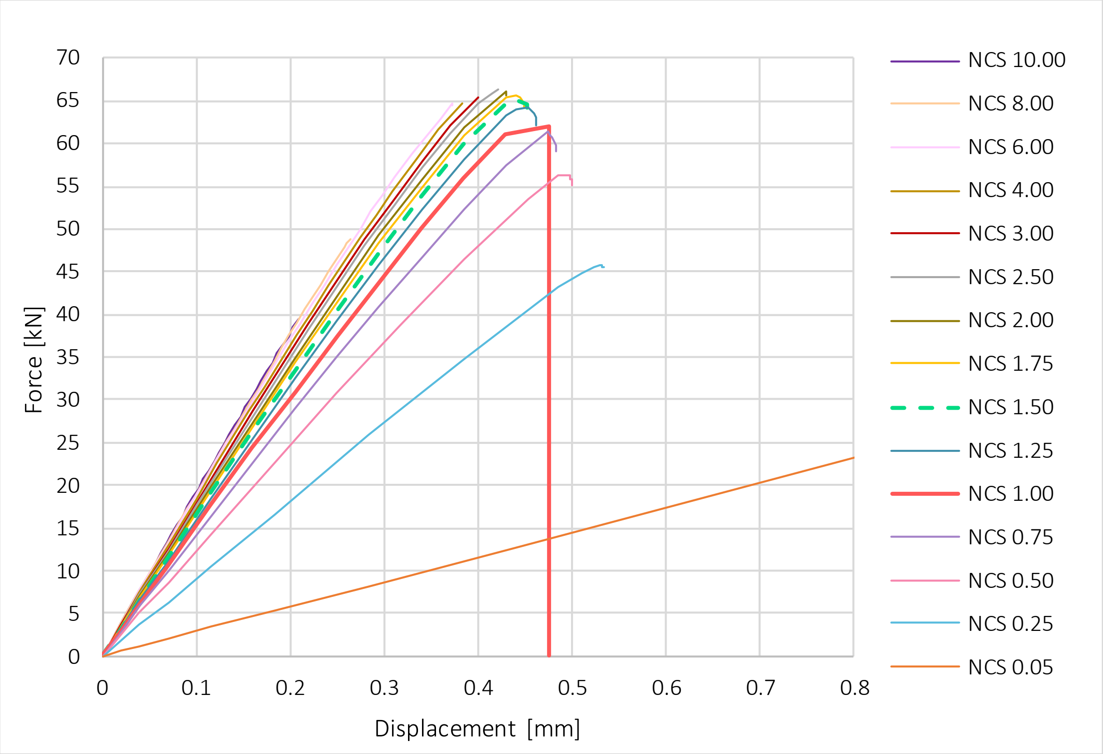

Figure 5.2 The force vs displacements for the different normalized cohesive stiffness (NCS) values for PUR with an anchorage length of 160 mm. The simulation corresponding to the chosen normalized cohesive stiffness of 1.5 times the reference value is marked by a dashed curve.

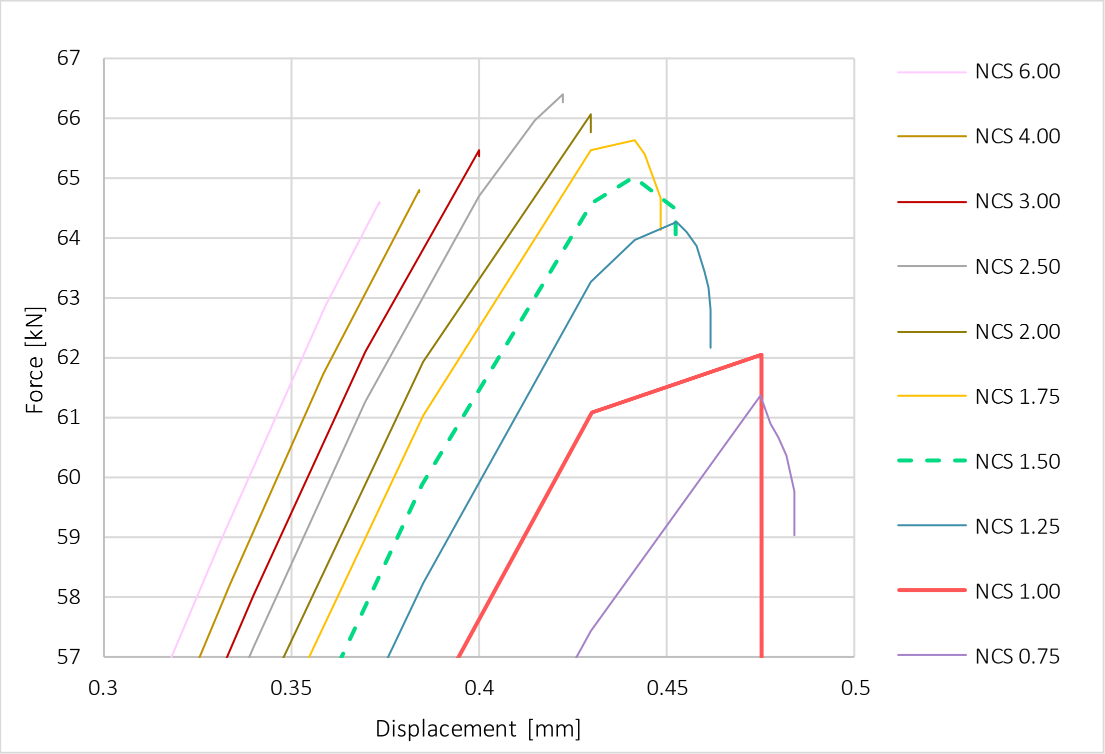

Figure 5.3 Magnification of maximum values for the force vs displacements curves for the different normalized cohesive stiffness (NCS) values in Figure 5.2. The simulation corresponding to the chosen normalized cohesive stiffness of 1.5 times the reference value is marked by a dashed curve.

For PUR, with the anchorage length 320 mm, the results can be seen in Figure 5.4. For cohesive stiffness 1.25-6 times greater than the reference values, the difference in pull-out capacity between the simulations is also small, and lies within the range of 1.6 kN, which is less than 2 %. After exceeding a point corresponding to 6 times the reference values, a non-converging behavior is evident.

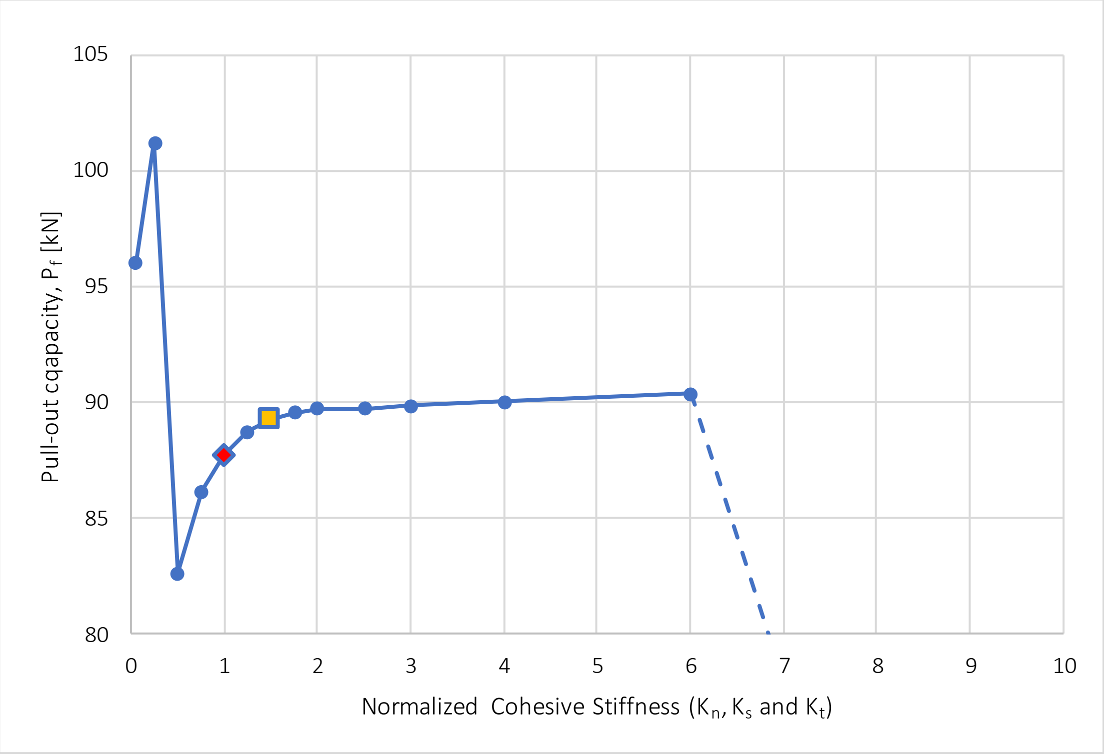

Figure 5.4 The predicted pull-out capacity vs normalized cohesive stiffness for PUR with an anchorage length of 320 mm. The reference case is marked by a red diamond. The simulation corresponding to the chosen normalized cohesive stiffness of 1.5 times the reference value is marked by a yellow square.

For simulation with EPX adhesive, the same behavior as for PUR is displayed. Based on the investigation performed, and to ensure sufficient accuracy of the pull-out capacity as well as to avoid non-converging behavior, cohesive stiffness values of 1.5 times greater than the reference was used for further analyses. For PUR, this means that values of K_n=1200 [GPa/m] and K_s=K_t=120 [GPa/m] was chosen. The corresponding values for EPX was K_n=1540 [GPa/m] and K_s=K_t=154 [GPa/m]. For input data used in the cohesive stiffness study, see Table 5.4, and for complete results of the investigation, see Appendix A.

5.2 Influence of mesh density

The influence of mesh density was investigated with regard to ultimate load and stress distribution. The objective was to define a mesh that provided good accuracy of ultimate load and stress distribution for a reasonable simulation time.

The mesh size was investigated for PUR adhesive and anchorage lengths of 160 mm and 320 mm. The initial increment was set to 0.01, the maximal increment limit to 0.1 and the minimum allowable increment size to 10^{-10}. This setup was kept constant along with the input data for every mesh configuration.

The general mesh pattern corresponding to the finest mesh size is shown in Figure 5.5. The element size was changed along the cohesive element row, while the element size, along the outer rim of the model, was kept constant for each mesh configuration. The finest mesh had an element length of 0.1 mm along the cohesive row and to obtain a coarser mesh the length along the bond line was increased. Images of all mesh configurations are presented in Appendix B.

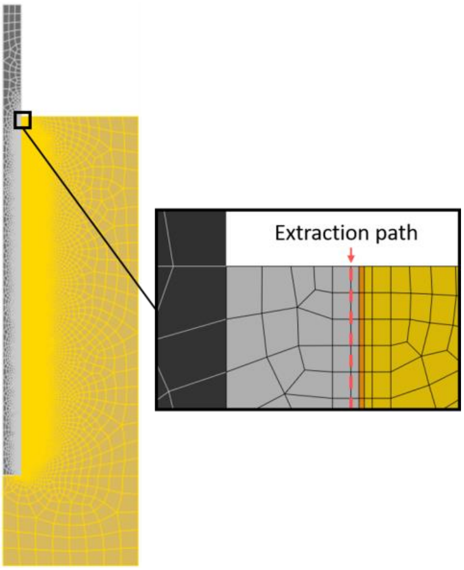

Figure 5.5 The mesh layout for the finest mesh configuration, the material layering and the position of the path used for extraction of stress distribution data.

The results of the ultimate load investigation are summarized in Table 5.2, and as can be understood by the results, the mesh size had little effect on the ultimate load. The simulation time for the analyses with different mesh densities, were between one and three minutes.

Table 5.2 The ultimate load and number of elements for anchorage lengths of 160 and 320 mm.

Anchorage length 160 mm		Anchorage length 320mm	
No. of elements	Ultimate load [kN]	No. of elements	Ultimate load [kN]
48668	65.009	71473	89.259
20979	65.024	59388	89.285
9117	65.024	19114	89.285
6131	64.789	15854	89.289

The difference between the finest and the coarsest mesh, was approximately 0.3 % for an anchorage length of 160 mm. The difference for an anchorage length of 320 mm was even smaller.

Shear and peel stress distributions were extracted and studied for a path, within the adhesive, close to the cohesive element row, illustrated in Figure 5.5. The stress distributions presented, were taken for a displacement of 0.02 mm (Figure 5.6 and Figure 5.7) when no damage had occurred, as well as a displacement of 0.45 mm (Figure 5.8 and Figure 5.9), just before failure.

The shear stress distributions for a displacement of 0.02 mm, illustrated in Figure 5.6, were similar for all mesh configurations. The difference between the finest and the coarsest mesh was around 0.2 %, measured at 5 mm from the free surface.

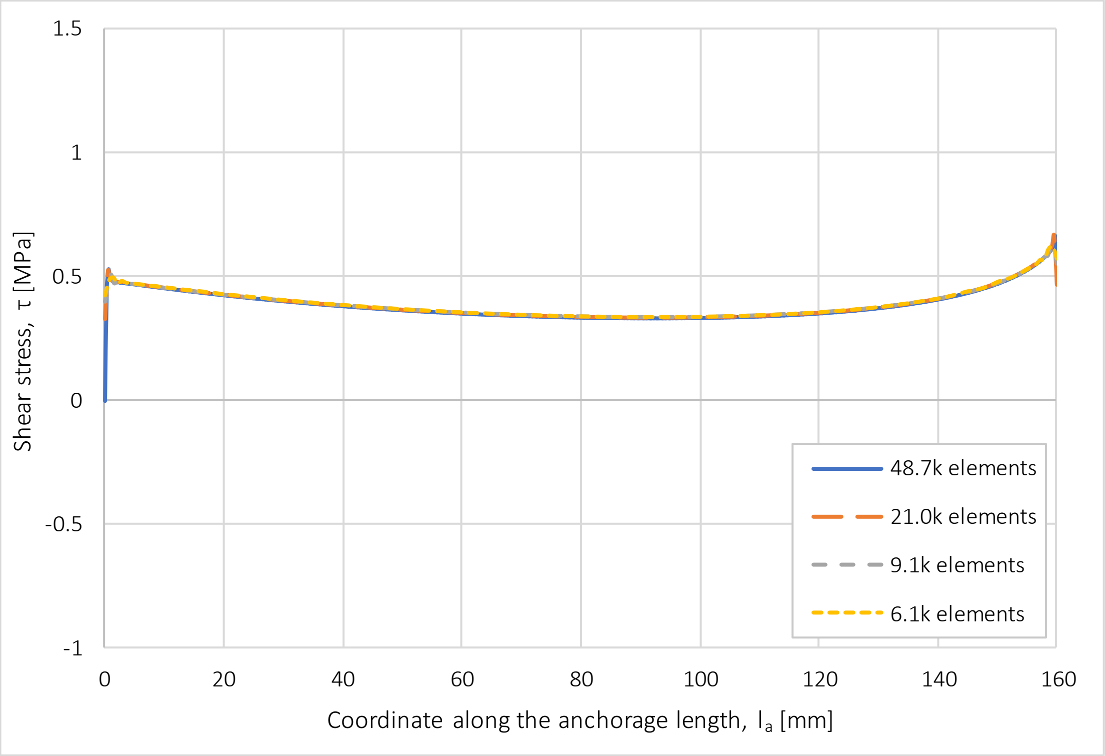

Figure 5.6 The shear stress distributions at u=0.02 mm, along the defined path for the specimen with 160 mm anchorage length. The free surface of the joint is at 0 mm.

The peel stress distributions for a displacement of 0.02 mm, illustrated in Figure 5.7, were similar for all mesh configurations. The difference between the finest and the coarsest mesh was around 0.2 %, measured at 5 mm from the free surface.

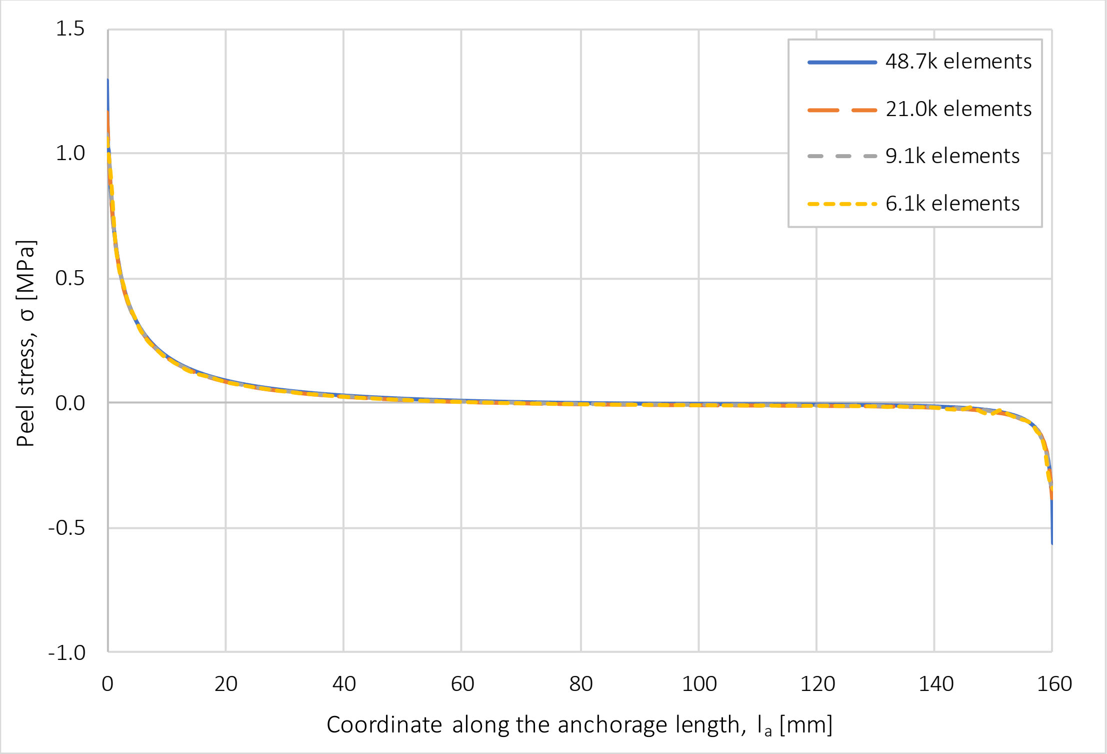

Figure 5.7 The peel stress distributions at u=0.02 mm, along the defined path for the specimen with 160 mm anchorage length. The free surface of the joint is at 0 mm.

The shear stress distributions for a displacement of 0.45 mm are illustrated in Figure 5.8. The difference between the finest and the coarsest mesh was around 3.2 %, measured 60 mm from the free surface. The same comparison of finest to the second coarsest configuration, gave a difference of 0.2 %.

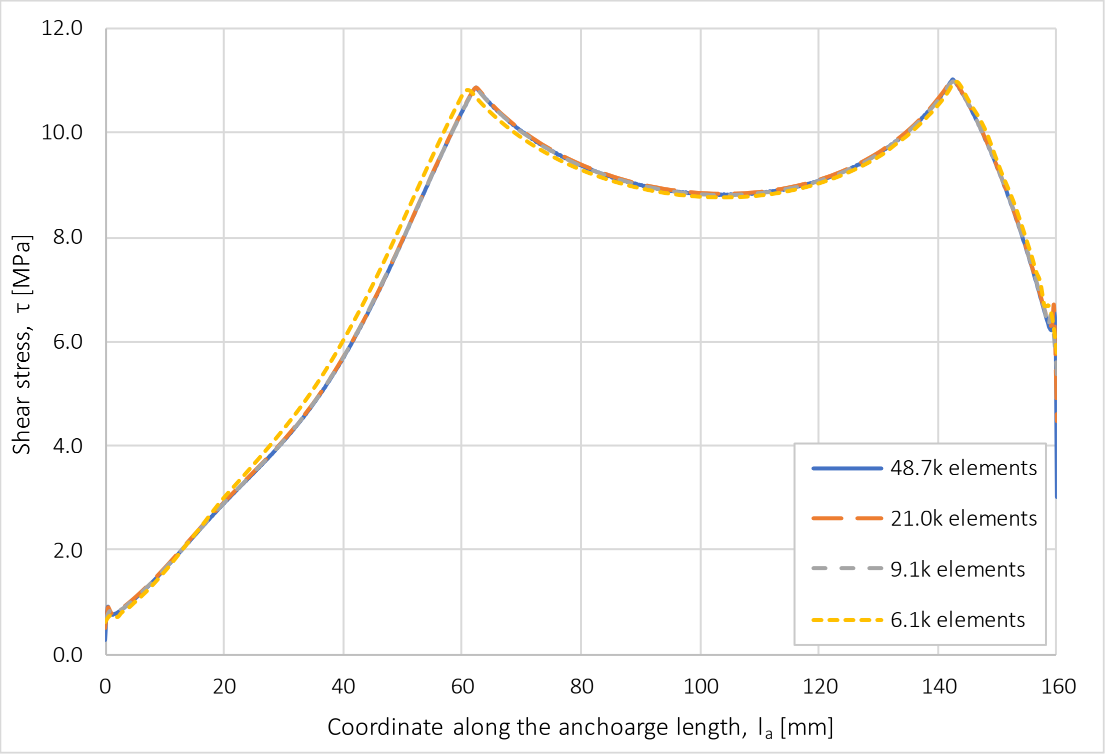

Figure 5.8 The shear stress distributions at u=0.45 mm, along the defined path for the specimen with 160 mm anchorage length. The free surface of the joint is at 0 mm.

The peel stress distributions for a displacement of 0.45 mm are illustrated in Figure 5.9. The difference between the finest and the coarsest mesh was around 2.6 %, measured 60 mm from the free surface. The same comparison of finest to the second coarsest configuration, gave a difference of 0.5 %. The simulation with the coarsest mesh configuration displays an uneven peel stress distribution at approximately 150 mm from the free surface.

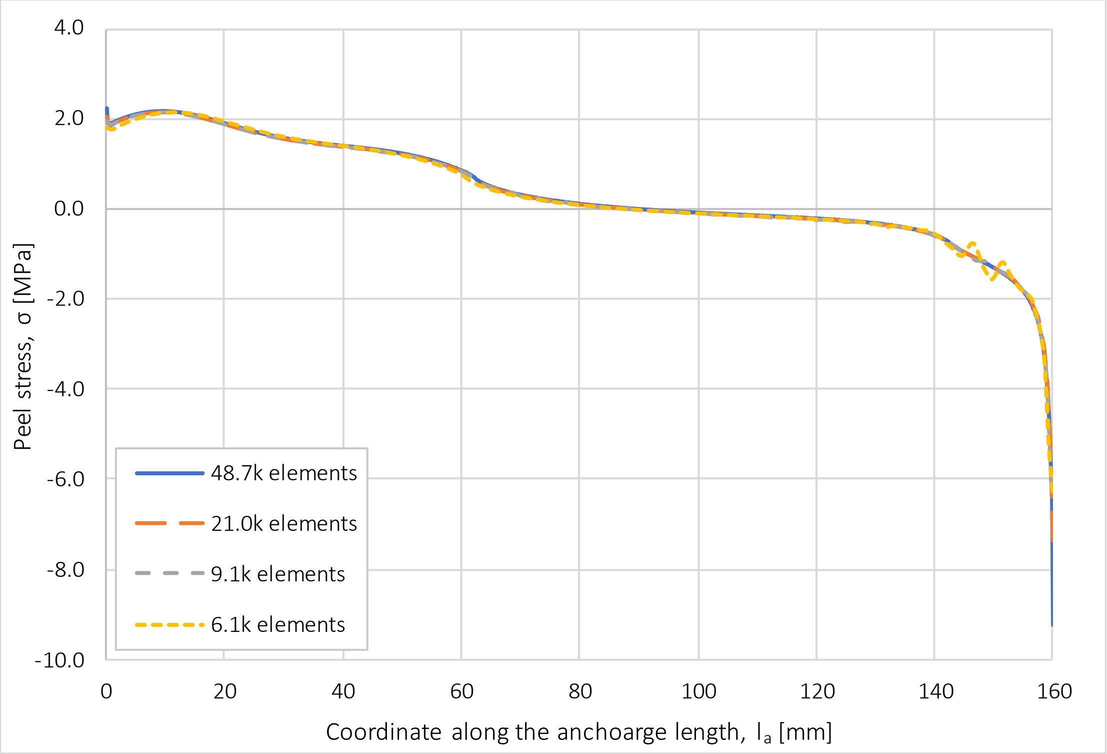

Figure 5.9 The peel stress distributions at u=0.45 mm, along the defined path for the specimen with 160 mm anchorage length. The free surface of the joint is at 0 mm.

The mesh analysis showed that the results from the axisymmetric model, regarding ultimate load, stress distributions and simulation time, were unsensitive to changes of the mesh density. Since the mesh configurations showed similar results, while the increase in simulation time was relatively unaffected, the finest mesh, with 48.7 thousand elements, was used in further investigations.

5.3 Influence of axisymmetry

To investigate the effect of axisymmetry, a three-dimensional verification model was made. An initial 3D model was set up with the same material layering as the axisymmetric model, but due to convergence issues, the 3D model had to be simplified, as described in section 4.1. This, however, made the 3D model less comparable with the axisymmetric model, thus an additional axisymmetric model was created with the same layering as the 3D model, see Figure 5.10. This was made to further investigate the influence of the cohesive row thickness.

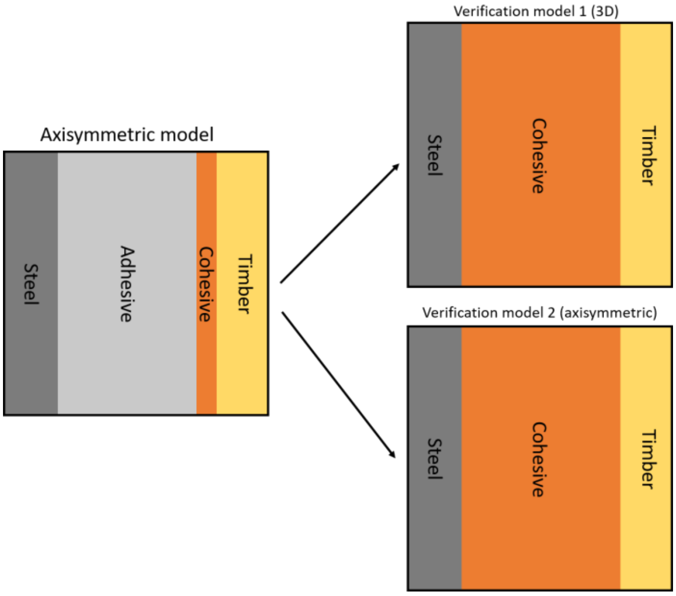

Figure 5.10 The bond line layers of the axisymmetric model and the two verification models.

The three models were compared for PUR adhesive with an anchorage length of 160 mm, and the results are shown in Table 5.3. The simulation time for the 3D model was approximately 60 minutes, while the axisymmetric models finished in less than 3 minutes.

Table 5.3 The ultimate load for the three models. The difference is taken in relation to the axisymmetric model.

Model	Axisymmetric model	Verification model 1 (3D)	Verification model 2 (Axisymmetric)
Ultimate load [kN]	66.5	65.2	64.6
Difference [%]	-	1.95	2.86

The difference in ultimate load between verification model 1 and verification model 2 is around 0.9 %. Thus, the influence of the axisymmetric condition on the pull-out capacity was said to be negligible. The difference between the axisymmetric model and verification model 1 was measured to about 1.95 %, while the difference between the axisymmetric model and verification model 2 was measured to about 2.86 %.

Load-displacement curves for the three models are presented in Figure 5.11. The axisymmetric model and verification model 1 exhibit similar stiffness, while verification model 2 displays a slightly stiffer behavior.

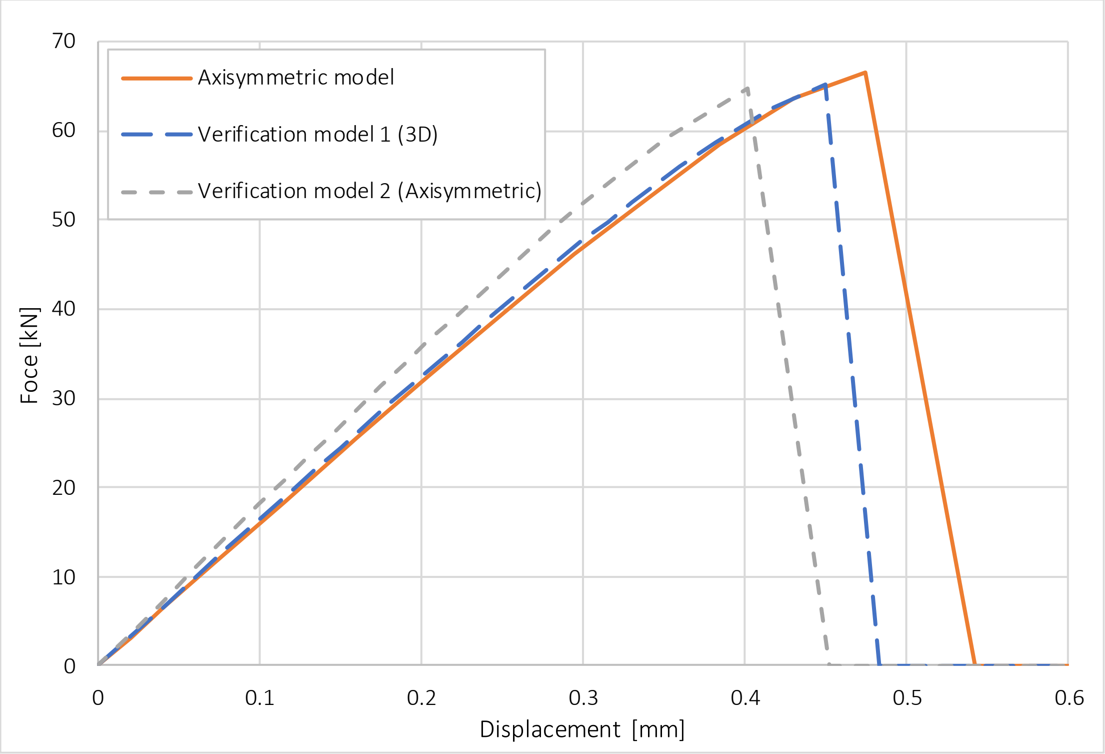

Figure 5.11 Load-displacement curves the different finite element models.

The aim of the investigation was to study several anchorage lengths. However, verification model 1 turned out to be unstable when changing input values and geometry, resulting in only one simulation converging. Hence only one length is presented.

From the investigation of axisymmetry, the axisymmetric model was proved valid, since the difference in ultimate load between the models were within the range of 3 %. Additionally, the axisymmetric model exhibited a more stable behavior during simulations compared to verification model 1. Ultimately, the axisymmetric model describes failure in the timber-adhesive interface, whereas verification model 1 and 2 describes failure of the whole bond line. Since failure of connections glued with PUR and EPX, takes place close to the timber-adhesive interface, the axisymmetric model is considered to be more realistic, with regard to pull-out failure.

5.4 Stress distribution and damage progression

From the axisymmetric model, stress distributions and damage progressions along the bond line were extracted and analyzed, to make a judgement on the reliability of the model. In this section, peel and shear stresses, as well as damage progressions, for anchorage lengths of 160 mm and 320 mm with PUR adhesive, are presented.

The stress distributions were extracted for the first increment of each simulation, which for both lengths, was an axial displacement of 0.02 mm. Additionally, distributions just before failure were extracted, which for the 160 mm long joint, corresponded to a displacement of 0.45 mm, and for the 320 mm long connection, a displacement of 0.62 mm. The stress distributions are shown in Figure 5.12.

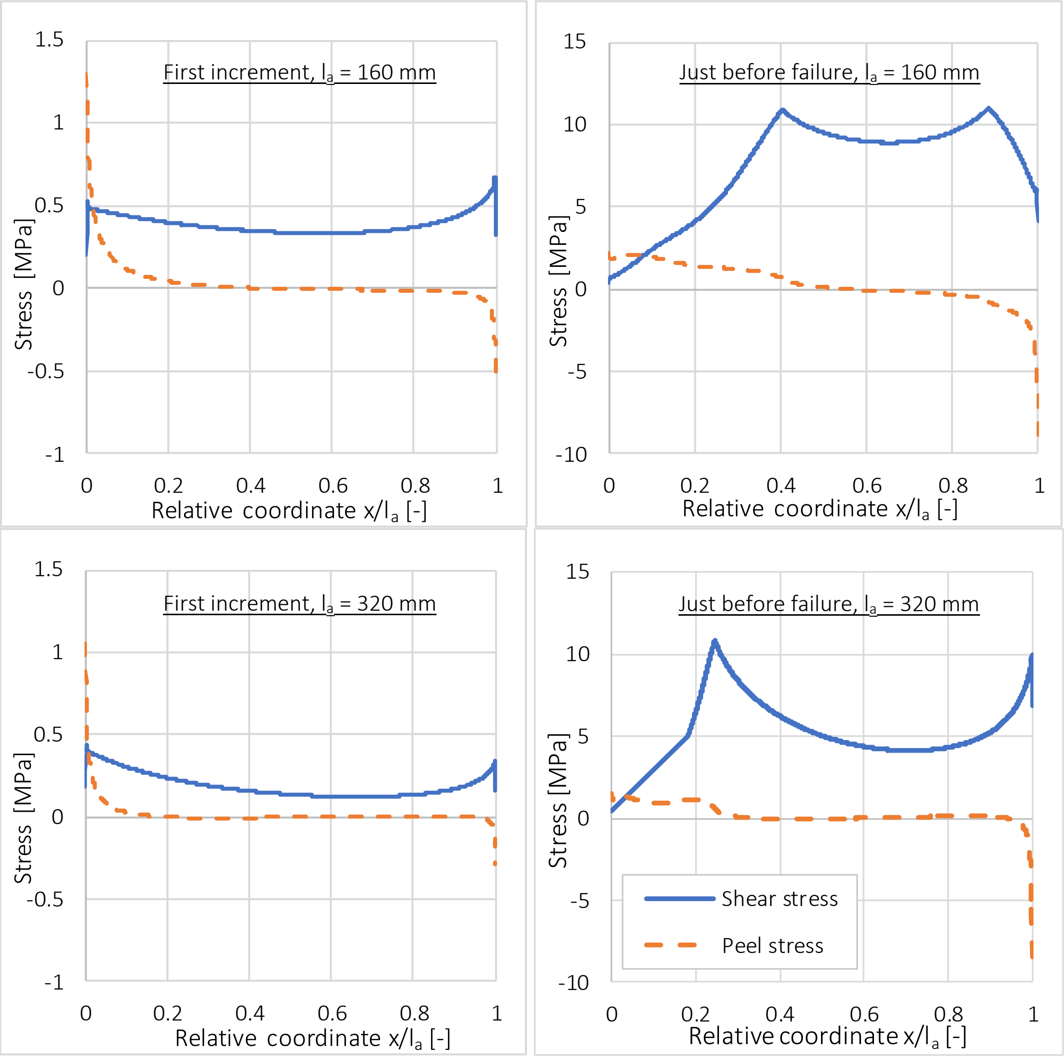

Figure 5.12 The top row shows stress distributions for anchorage length 160 mm and the bottom row for 320 mm. The left column shows the stress distributions at the first increment when no damage has taken place and the right column shows the distributions just before failure. The free surface of the connection is at x=0 and thus $x/l_a=0$, where $0 \le x \le l_a$.

The stress distributions, just before failure, show the occurrence of a damaged zone, followed by an undamaged region. In the undamaged zone, the stress distributions behave in a linear elastic manner between two stress peaks. For the longer anchorage length, the difference between the stress peaks and the in-between minimum is larger, compared to the difference for the shorter anchorage length. This agrees with stress distributions predicted with Volkersen theory, presented in subsection 2.7.1. Furthermore, the results are similar to the stress distributions obtained by Serrano (2001b).

The damage progression along the anchorage zone for the two lengths are illustrated in Figure 5.13. The data was extracted along a path within the cohesive element row. If the damage is 0, the element is undamaged, and if the damage is 1, the element is completely damaged and has lost all its load transferring ability.

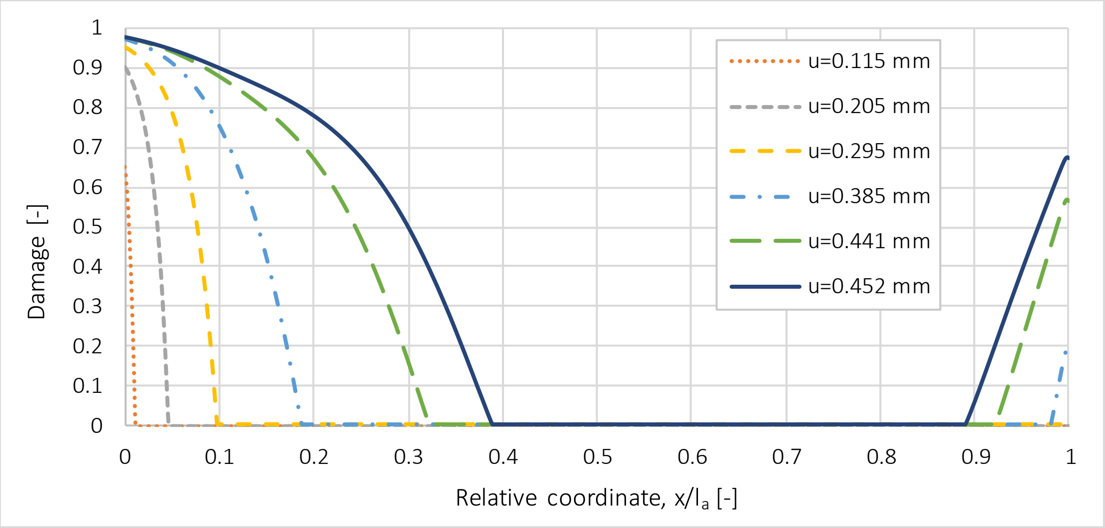

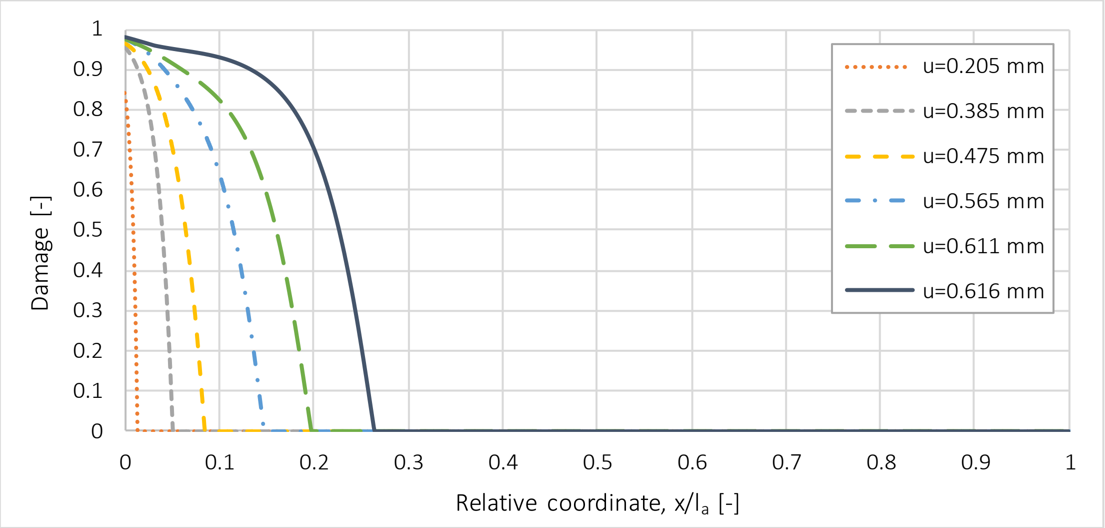

Figure 5.13 The damage progression for connections with anchorage lengths of 160 mm (top) and 320 mm (bottom). The adhesive type simulated is PUR. The free surface of the connection is at x=0 and thus $x/l_a=0$, where $0 \leq x \leq l_a$.

A difference in damage progression can be seen between the two anchorage lengths. For an anchorage length of 160 mm, damage occurs at the bottom of the anchorage zone, prior to failure, whereas the 320 mm long connection only exhibit damage at the top of the joint. The same trend can be observed in the stress distributions, in Figure 5.12, where the shorter anchorage length has a gradual dip towards the end of the of the anchorage zone, just before failure.

5.5 Verification against previous studies

To verify the validity of the axisymmetric model, the obtained numerical results were compared to the test and numerical results presented by Gustafsson & Serrano (2002), described in subsection 3.1.2 and section 3.2. The input data for the model and verification analysis is presented in Table 5.4.

Table 5.4 Input data used for verification of the axisymmetric FE model.

Steel	Young's modulus		205	[GPa]
	Poison´s ratio		0.3	[-]
Timber	Young's modulus	L	11	[GPa]
		R	0.6	[GPa]
		T	0.37	[GPa]
	Shear modulus	LR	0.69	[GPa]
		LT	0.3	[GPa]
		RT	0.03	[GPa]
	Poison´s ratio	LR	0.04	[-]
		LT	0.03	[-]
		RT	0.35	[-]
PUR	Young's modulus		1.56	[GPa]
	Poison´s ratio		0.3	[-]
COHESIVE (PUR)	Normal stiffness		1200	[GPa/m]
	Shear stiffness		120	[GPa/m]
	Normal fracture energy		400	[Nm/m^2]
	Shear fracture energy		1200	[Nm/m^2]
EPX	Young's modulus		2.0	[GPa]
	Poison´s ratio		0.3	[-]
COHESIVE (EPX)	Normal stiffness		1540	[GPa/m]
	Shear stiffness		154	[GPa/m]
	Normal fracture energy		400	[Nm/m^2]
	Shear fracture energy		2200	[Nm/m^2]

The test series, presented by Gustafsson & Serrano (2002), used timber of strength class C24, while it is not mentioned what timber data they used in their finite element analyses. In this project, input data corresponding to strength class C24 was used for numerical analyses. Additionally, the fracture properties, as well as the properties of the steel rod, corresponds to the values used by Gustafsson & Serrano (2002). Values of cohesive stiffness were determined in a converge investigation, presented in section 5.1. The values of Young's moduli for PUR and EPX were taken from Loctite (2015) and Henkel (2018).

With this input data, along with the fine mesh configuration, the model was rebuilt to match the geometry used in the test series. The simulations were done for PUR and EPX adhesives and the results from the verification analysis are shown in Table 5.5.

Table 5.5 Results of tests and numerical simulations presented in (Gustafsson & Serrano, 2002). Additionally, the numerical results of the axisymmetric simulations performed in this project are marked as "verification".

		PUR		EPX	
Anchorage length [mm]		160	320	160	320
Gustafsson & Serrano (2002)	Pull-out capacity, test [kN]	64.4	91.0	61.6	106.3
	Pull-out capacity, FEM [kN]	67.1	93.8	89.2	118.7
Verification	Pull-out capacity, FEM [kN]	65.0	89.3	82.6	117.5

The results of the verification showed a good agreement for both anchorage lengths and adhesive types, compared to FE simulations made by Gustafsson & Serrano (2002). The axisymmetric model predicts pull-out capacities closer to the test results. For EPX, both the axisymmetric and the reference FE models, produce similar overpredictions of the pull-out capacity. However, the axisymmetric model is slightly more conservative.

5.6 Discussion on the validity of the established axisymmetric FE model

The axisymmetric model was established to simulate bond line failure, and more accurately, failure in the timber-adhesive interface. With regard to pull-out capacity, the results of the axisymmetric model are satisfying, compared to the three-dimensional FE model used by Gustafsson & Serrano (2002). The same can be stated for test results where specimens fail in the same manner as was defined in the axisymmetric FE model.

Comparing the efficiency of the axisymmetric and three-dimensional models, created as part of this project, it can be stated, that the former is both faster and more reliable. Simulations made with the 3D model were significantly slower, as well as more prone to fail due to convergence issues. The simulation time for the axisymmetric model was around 3 % of the run time of the 3D model. Additionally, the meshing procedure of an axisymmetric model is considerably simpler and less time consuming. Also, considering that the difference in calculated ultimate load is less than 2 %, it can be argued that the simplicity of the axisymmetric model outweighs the possible increase in accuracy of the 3D model.

While axisymmetric FE simulations manage to sufficiently predict the ultimate load of an axially loaded glued-in rod, there are some limitations. Since the concept of axisymmetry only allows for cylindrical shapes, modelled about an axis, it does limit the possibilities of creating desirable geometries. This is also the reason that multiple rod connections cannot be modelled using this approach. With a model, based on axisymmetry, comes a defined set of directions, which, do not, for example, allow for realistic modelling of timber. However, the impact of direction dependent properties in timber was studied, and subsequently found to not significantly affect the load bearing capacity.

The stress distributions extracted from the axisymmetric simulations, display similar behavior as the ones obtained from Serrano's (2001b) FE analyses, described in section 3.2. Furthermore, an agreement between the damage progressions and stress distributions, extracted from the axisymmetric model, is evident. This suggests that the axisymmetric model produces reasonable results.

From the extracted stress distributions, higher stress peaks can be observed at the end of the anchorage length as the mesh density increases, see Figure 5.6 to Figure 5.9. The stress peaks are a result of singularities in the numerical simulations, probably due to the geometry of the anchorage zone's end. High local stress concentrations will appear in such zones, and will increase for decreasing element size. However, this phenomenon does not affect the ultimate load of the connection, Table 5.2.

A possible explanation for the discrepancy in pull-out capacity between tests and numerical simulations, for connections utilizing EPX, is cited by Gustafsson & Serrano (2002). The numerical simulations assume that failure will take place in the bond line. This was not always the case for tested specimens, where some of the connections, glued with EPX, instead failed in the timber close to the bond line. The same tendency was reported by Rossignon & Espion (2008), when testing the axial capacity of single rod connection glued with EPX.

The behavior of axially loaded GiR connections can be described by load-displacement curves, and to further ensure the validity of the axisymmetric FE model, it would have been useful to compare load-displacement curves of previous test results and numerical simulations. However, data on load-displacement behavior for previously performed tests are seldom presented in literature. Conversely, and in accordance with the purpose of this project, it was sufficient to obtain accurate predictions of the ultimate load rather than the behavior up to the failure.

The established model does not capture a realistic softening behavior. While all simulated joints exhibited a certain degree of post-peak behavior, none of the simulations fully converged, and all analyses subsequently failed due to convergence issues. It can be argued that the finite element model is sensitive with regard to the input data used, and in order to possibly avoid convergence problems, additional calibration might be needed.

It should also be noted that there will always be a difference between numerical simulations and actual experiments. While a finite element model represents a connection with no imperfections, a real tested specimen will, to some extent, contain impurities, which may affect the load bearing capacity. Examples of such impurities include material defects and variation as well as manufacturing errors.

The model could have been developed to capture additional bond line failures, as well as yielding of the steel rod and failure in the timber. However, this was not considered necessary for this project. One of the main objectives was to establish a reliable and efficient FE model that would accurately predict the pull-out capacity of glued-in rods. This can be argued to have been fulfilled.

6 Parameter study

A parameter study was done to investigate the validity of the design equation derived, from Volkersen theory, developed by Gustafsson & Serrano (2002), see equation (3.13). According to the theory, the pull-out capacity of an axially loaded glued-in rod, depends on the stiffness ratio of the materials in the connection, as well as the parameter ϖ, which in turn depends on the geometrical and material lengths parameters l_{geo} and l_m.

The study was set up so that the influence of the geometrical length, l_{geo}, see equation (3.10), as well as the material stiffness ratio, k, see equation (3.9), on the load bearing capacity of axially loaded glued-in rods could be investigated.

Numerical results were gained from simulations, using the axisymmetric finite element model described in chapter 4. The results were subsequently compared against the predicted capacity of the design equation, corresponding to the same material input data. Since the load configuration in the FE simulations was set as pull-pull, it was initially believed that the numerical simulations would yield a higher load bearing capacity than what was predicted by Volkersen theory.

The influence of the material stiffness ratio, k, was investigated by studying how the unitless pull-out capacity changed when changing the timber area, A_w and anchorage length, l_a, in such a way that l_{geo} remained constant. Thus, all parameters, except the timber area and anchorage length were kept constant. From equation (3.10), an expression, describing the relation between the anchorage length and timber area, was derived:

$$l_a = \sqrt{\frac{l_{geo} \cdot 2 \cdot A_r}{\pi \cdot d_h} \cdot \frac{1}{1 + \frac{E_r \cdot A_r}{E_w \cdot A_w}}} \tag{6.1}$$

Further, a span of geometrical lengths, as well as three timber areas, were defined and the corresponding anchorage lengths were solved from equation (6.1). The timber areas were defined as the area of a cylinder with a diameter of 80, 120 and 200 mm respectively. Reduction of the timber areas due to the circular hole of the rod and adhesive, was neglected. This was done in accordance with guidelines from Gustafsson & Serrano (2002). The smallest cross-sectional area was based on the minimum edge distance in the New Zealand design codes (Steiger et al., 2015).

The timber areas created the base of three finite element series which varied along the defined span of $l_{geo}^{0.5}$ (25-325 $\text{mm}^{0.5}$). In total, the three FE series with eight individual geometries each, generated 24 different models, which are presented in Table 6.1. They were assembled and meshed in Abaqus and simulated with corresponding settings for PUR and EPX adhesives with the same input as in Table 5.4.

Table 6.1 The three FE series A, B and C with span of investigated $l_{geo}^{0.5}$ and the corresponding anchorage lengths.

FE series	d [mm]	A_w [mm^2]	k [-]	Sim. no.	$l_{geo}^{0.5}$ [mm$^{0.5}$]	l_a [mm]
A	80	5027	0.71	A25	25	51.9
				A50	50	103.8
				A75	75	155.7
				A125	125	259.6
				A175	175	363.5
				A225	225	467.3
				A275	275	571.2
				A325	325	675.0
B	120	11 310	0.31	B25	25	59.5
				B50	50	118.9
				B75	75	178.4
				B125	125	297.3
				B175	175	416.2
				B225	225	535.1
				B275	275	654.0
				B325	325	772.9
C	200	31 416	0.11	C25	25	64.8
				C50	50	129.7
				C75	75	194.5
				C125	125	324.2
				C175	175	453.9
				C225	225	584.6
				C275	275	713.3
				C325	325	842.9

6.1 Results of numerical simulations

The results of the numerical analysis are presented in Table 6.2 (PUR) and Table 6.3 (EPX) as well as Figure 6.1 (PUR) and Figure 6.2 (EPX), where the results from each FE series are plotted against the predicted capacity according to Volkersen theory.

Table 6.2 Results of numerical simulations compared to predicted capacity according to the design equation corresponding to pull-compression loading, equation (3.13). Results are displayed in ultimate load, P_f, and unitless capacity, Ᵽ. The adhesive type is PUR. Results from numerical simulations have the denotation "FE", while results from the design equation (3.13) have the denotation "eq".

FE series	Sim. no.	$P_{f,FE}$ [kN]	Ᵽ_{FE} [-]	$P_{f,eq}$ [kN]	Ᵽ_{eq} [-]	$(\text{Ᵽ}_{eq} - \text{Ᵽ}_{FE})/\text{Ᵽ}_{FE}$ [%]
A_{PUR}	PA25	21.9	0.720	27.7	0.909	26.3
	PA50	44.1	0.724	44.2	0.725	0.2
	PA75	64.5	0.706	51.2	0.560	-20.7
	PA125	91.9	0.603	54.6	0.358	-40.6
	PA175	102.4	0.480	55.0	0.257	-46.3
	PA225	105.7	0.385	55.0	0.200	-48.0
	PA275	106.9	0.318	55.0	0.164	-48.5
	PA325	107.4	0.271	55.0	0.139	-48.8
B_{PUR}	PB25	25.5	0.730	31.7	0.909	24.5
	PB50	50.0	0.716	50.6	0.725	1.2
	PB75	70.5	0.673	58.6	0.560	-16.9
	PB125	87.3	0.500	62.5	0.358	-28.4
	PB175	92.5	0.378	62.9	0.257	-32.0
	PB225	94.3	0.300	63.0	0.200	-33.2
	PB275	95.0	0.248	63.0	0.164	-33.8
	PB325	95.2	0.210	63.0	0.139	-33.8
C_{PUR}	PC25	28.1	0.737	34.6	0.909	23.3
	PC50	54.8	0.719	55.2	0.725	0.8
	PC75	72.8	0.637	63.9	0.560	-12.1
	PC125	85.9	0.451	68.2	0.358	-20.6
	PC175	87.6	0.329	68.6	0.257	-21.7
	PC225	88.4	0.257	68.7	0.200	-22.1
	PC275	89.3	0.213	68.7	0.164	-23.1
	PC325	88.9	0.180	68.7	0.139	-22.7

Table 6.3 Results of numerical simulations compared to predicted capacity according to the design equation corresponding to pull-compression loading, equation (3.13). Results are displayed in ultimate load, P_f, and unitless capacity, $Ᵽ$. The adhesive type is EPX. Results from numerical simulations have the denotation "FE", while results from the design equation (3.13) have the denotation "eq".

FE series	Sim. no.	$P_{f,FE}$ [kN]	$Ᵽ_{FE}$ [-]	$P_{f,eq}$ [kN]	$Ᵽ_{eq}$ [-]	$(Ᵽ_{eq} - Ᵽ_{FE})/Ᵽ_{FE}$ [%]
A_{EPX}	EA25	26.6	0.685	35.7	0.918	34.1
	EA50	55.2	0.711	58.0	0.747	5.1
	EA75	82.8	0.711	68.2	0.586	-17.7
	EA125	120.6	0.622	73.7	0.380	-38.9
	EA175	136.1	0.501	74.4	0.274	-45.3
	EA225	140.4	0.402	74.5	0.213	-46.9
	EA275	140.0	0.328	74.5	0.174	-46.8
	EA325	142.4	0.282	74.5	0.148	-47.7
B_{EPX}	EB25	31.1	0.699	40.8	0.918	31.4
	EB50	62.0	0.697	66.4	0.747	7.2
	EB75	90.0	0.675	78.1	0.586	-13.2
	EB125	115.3	0.519	84.4	0.380	-26.8
	EB175	122.3	0.393	85.2	0.274	-30.4
	EB225	125.1	0.313	85.3	0.213	-31.8
	EB275	125.6	0.257	85.3	0.174	-32.2
	EB325	126.1	0.218	85.3	0.148	-32.3
C_{EPX}	EC25	34.5	0.712	44.5	0.918	29.1
	EC50	68.5	0.706	72.4	0.747	5.8
	EC75	93.4	0.642	85.2	0.586	-8.8
	EC125	112.8	0.465	92.0	0.380	-18.4
	EC175	116.1	0.342	92.9	0.274	-20.0
	EC225	117.3	0.268	93.0	0.213	-20.5
	EC275	117.5	0.220	93.0	0.174	-20.8
	EC325	117.7	0.187	93.0	0.148	-21.0

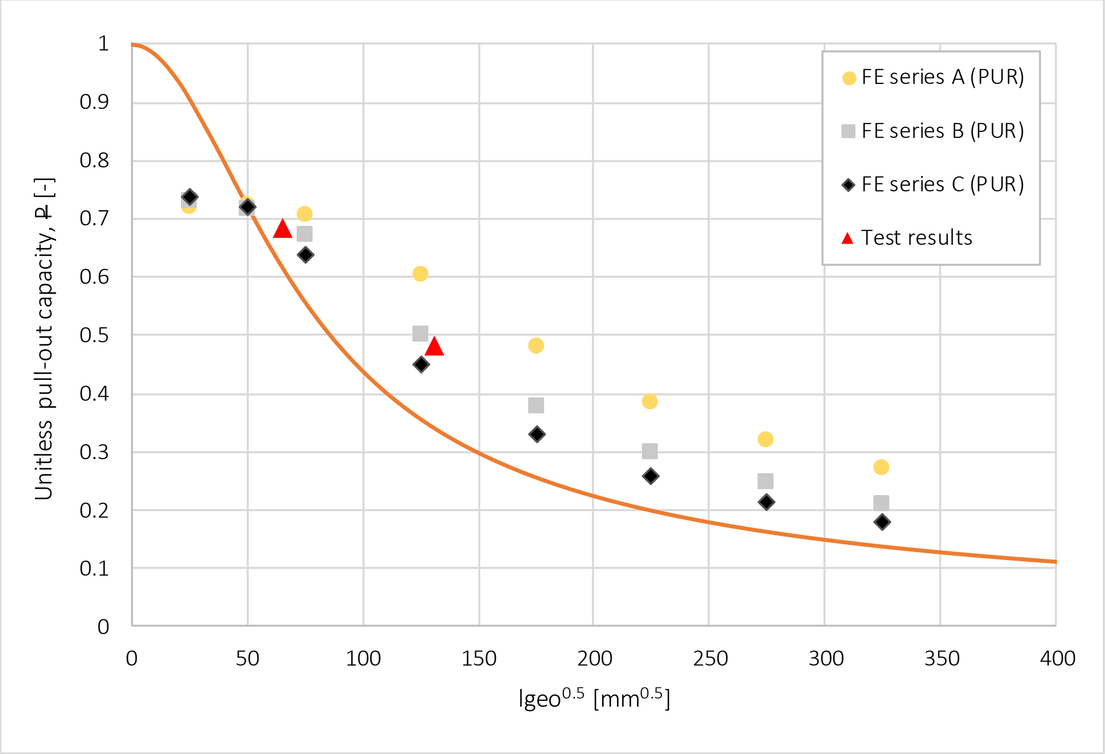

Figure 6.1 The results of the parameter study for PUR. The solid curve corresponds to the predicted pull-out capacity under pull-compression loading. The three FE test series A_{PUR}, B_{PUR} and C_{PUR} are marked along with test results from Gustafsson & Serrano (2002).

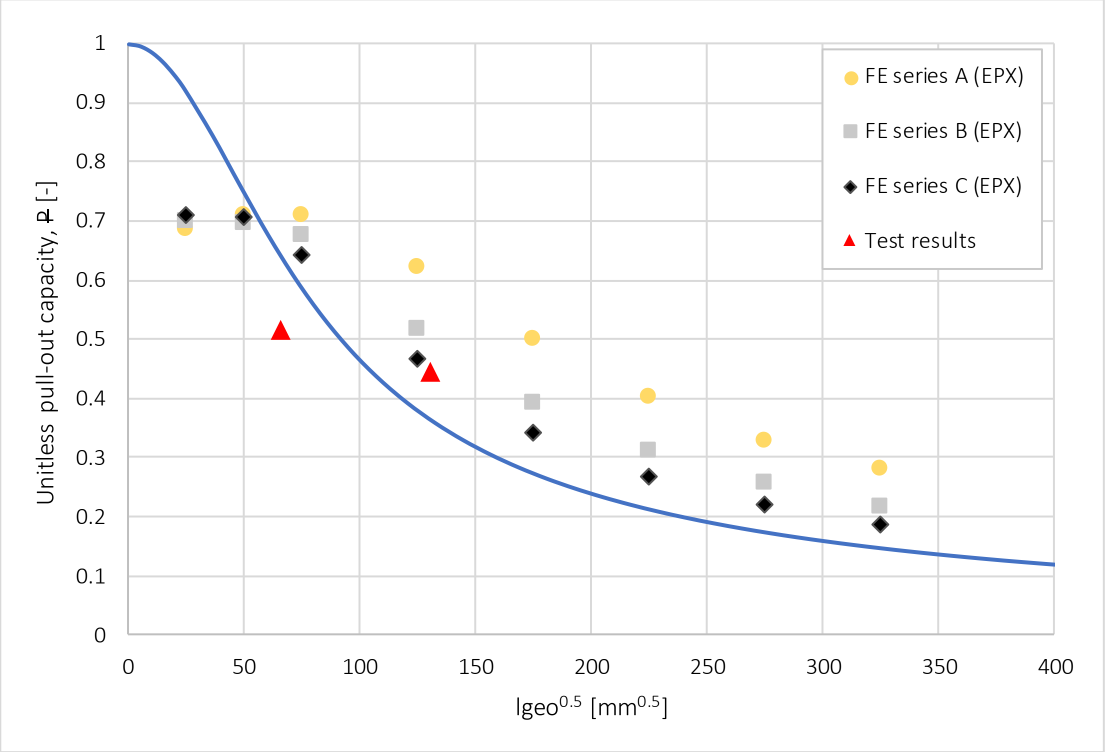

Figure 6.2 The results of the parameter study for EPX. The solid curve corresponds to the predicted pull-out capacity under pull-compression loading. The three FE test series A_{EPX}, B_{EPX} and C_{EPX} are marked along with test results from Gustafsson & Serrano (2002).

Compared to the tested specimens by Gustafsson & Serrano (2002), the design curve for pull-compression loading overestimates the capacity for connections glued with EPX for smaller values of l_{geo} (Figure 6.2). This is not the case for rods glued with PUR.

For larger geometrical lengths, FE series A gave higher pull-out capacity than FE series B, which in turn gave higher pull-out capacity than FE series C. The results of the three series coincide at approximately $l_{geo}^{0.5}$=50 mm$^{0.5}$, and for even smaller values of $l_{geo}^{0.5}$, test series C attained higher capacity. These trends are observable for both types of adhesives. Thus, it can be stated that a larger value of the material stiffness ratio, k, gives a higher capacity for specimens with a geometrical length higher than $l_{geo}^{0.5}$=50 mm$^{0.5}$.

Overall, and as expected, equation (3.13) underestimates the capacity for larger geometrical lengths and both adhesive types, compared to the FE analyses. This was true for larger values of l_{geo}. However, with a smaller value of l_{geo}, the design curves overestimate the capacity. Peel and shear stress distributions, for FE series A_{PUR} and simulations PA25, PA50 and PA75, were extracted in order to study the underlying causes. These stresses are illustrated in Figure 6.3 and Figure 6.4.

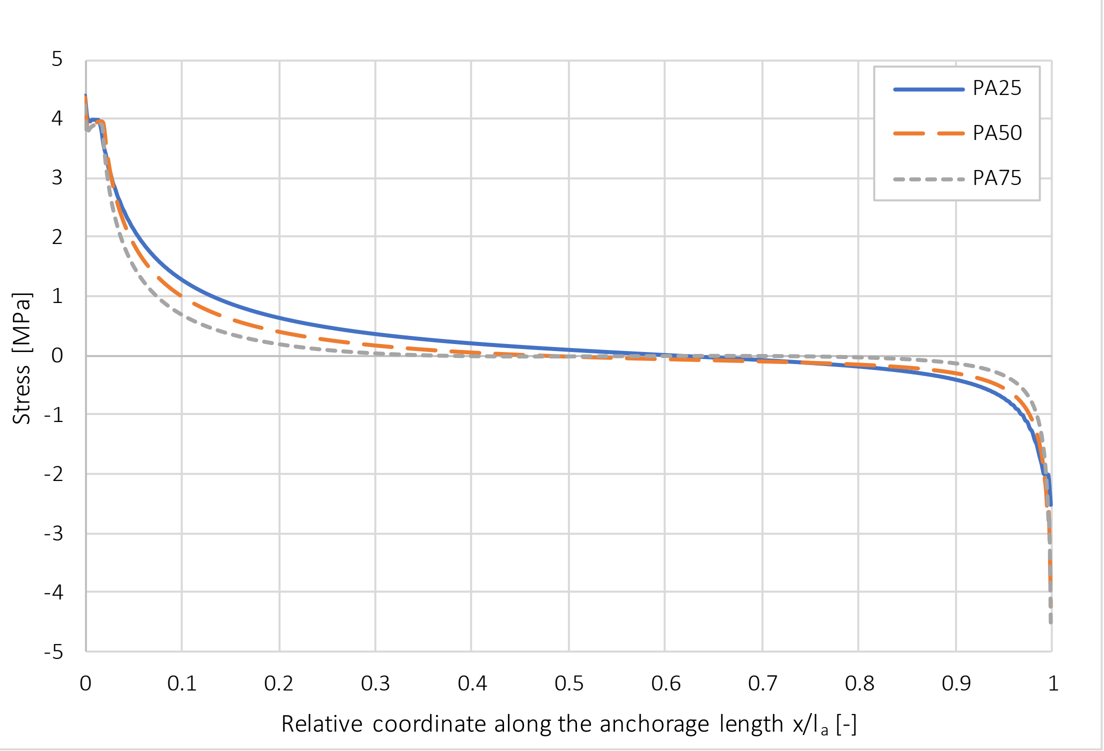

Figure 6.3 Peel stress distributions for FE series A_{PUR}, simulations PA25, PA50 and PA75, at the first increment where the peel strength (4 MPa) has been reached. This corresponds to deformations of u=0.07 mm, u=0.12 mm and u=0.16 mm for the three simulations respectively.

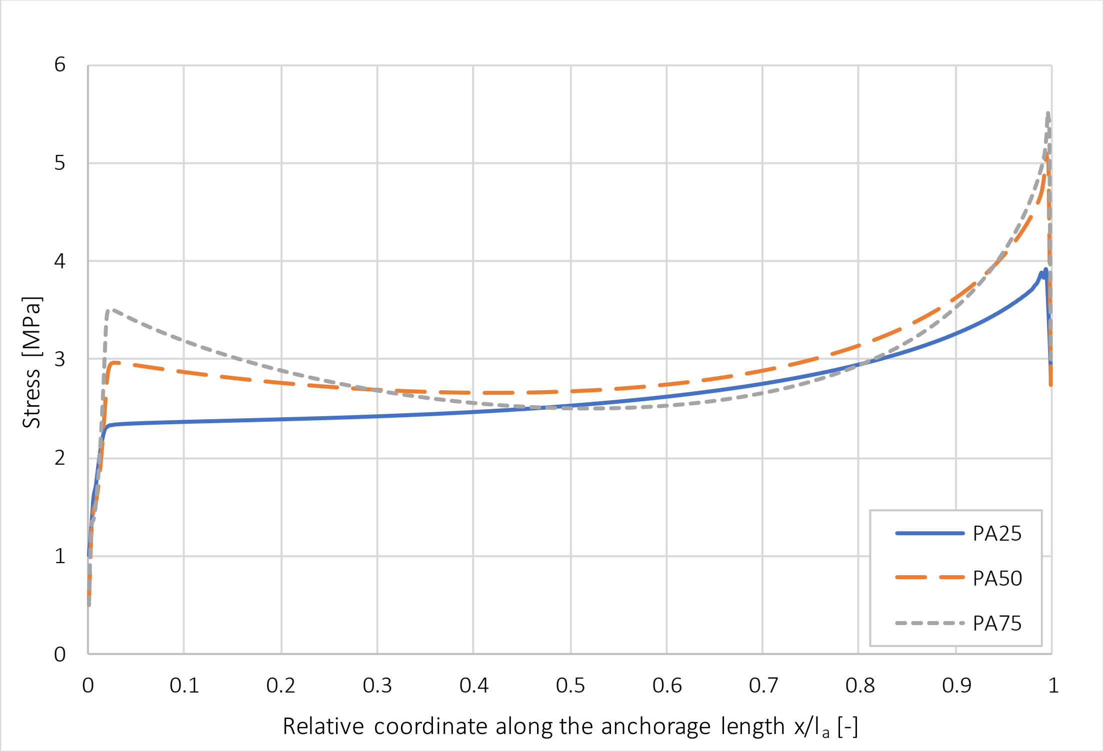

Figure 6.4 Shear stress distributions for FE series A_{PUR}, simulations PA25, PA50 and PA75, at the first increment where the peel strength has been reached. This corresponds to deformations of u=0.07 mm, u=0.12 mm and u=0.16 mm for the three simulations respectively.

For simulation PA25, the influence of peel stress is more dominant along the length of the rod, compared to what is the case for PA50 and PA75. Regarding shear stress distributions, the peak values increase for an increasing value of $l_{geo}^{0.5}$.

6.2 Discussion on parameter study

The finite element simulations were compared to the design equation presented by Gustafsson & Serrano (2002), see equation (3.13). The attained FE results followed the predicted trend and the design equation was generally conservative. However, for smaller values of l_{geo}, the design equation overestimated the load bearing capacity. A possible reason for this might be that the design curve only considers shear stresses in the bond line, and completely disregards the peel stress component, whose effect seems to increase for decreasing geometrical lengths. Thus, for short geometrical lengths, the load bearing capacity is probably governed by the peel stress rather than the shear stress. Consequently, only including the shear stress in the design equation (3.13), seems to be a reasonable assumption for large values of l_{geo}, while it should not be considered valid for smaller values of l_{geo}.

In the interval 25 $\text{mm}^{0.5} < l_{geo}^{0.5} < 75\ \text{mm}^{0.5}$, the three FE series switch places in relation to each other, see Figure 6.1 and Figure 6.2. For larger values of $l_{geo}^{0.5}$, a larger value of the material stiffness ratio, k, gives a higher capacity, but for values of $l_{geo}^{0.5} < 50\ \text{mm}^{0.5}$, this relationship changes and a larger value of k instead yields a lower capacity. The change seems to coincide at a point where the dominating stress mode shifts from shear to peel.

Values of $l_{geo}^{0.5}$ around 40 $mm^{0.5}$, correspond to an anchorage length of approximately 100 mm, which, with regard to practical use, is the minimum allowed anchorage length. Hence, values of $l_{geo}^{0.5}$ smaller than 40 $mm^{0.5}$ are purely for scientific purposes.

The test results for specimens glued with PUR show a relatively good agreement with the design equation. However, compared to specimens with shorter geometrical lengths that are glued with EPX, the design curve seems to be unconservative (see Figure 6.2). This is most likely due to that failure occurs in the timber instead of in the timber-adhesive interface, which the design equation presumes.

For PUR, the design curve predicts results on the safe side, in relation to both test results and FE results (for $l_{geo}^{0.5} > 50$ $mm^{0.5}$). Thus, it could be argued that the design equation is useful for glued-in rods utilizing PUR adhesives. However, as a design equation should be general and able to describe the behavior of connections glued with different adhesive types, it can be argued that equation (3.13) is not a valid design approach. An alternative method to predict the load bearing capacity of GiR connections is presented in chapter 7.

7 Proposed modified design equation

As discussed in section 6.2, the predictions of the existing design equation were not always conservative compared to test results of GiR connections. This was especially true for connections glued with EPX. In this chapter, a modification of the existing design equation is presented and compared to test data. The design equations are further discussed, simplified and the effect of different adhesive types is included. Finally, a new design equation is proposed.

7.1 Modified design equation

Since the design equation (3.13) was shown to be unconservative for smaller values of $l_{geo}^{0.5}$, a development of the existing design approach was established by Atashipour et al. (2018):

$$\bar{P} = \frac{\tanh(\bar{\omega})}{\bar{\omega}} \cdot (1 - e^{-\bar{\omega}}), \tag{7.1}$$

where ($1\text{-}e^{-\bar{\omega}}$) is a correction factor. This factor was derived with the help of a concept presented by Bocciarelli et al. (2008); the full derivation is presented in Appendix C. This equation reduces the predicted capacity for glued-in rods with shorter geometrical lengths, with the aim of always being conservative compared to equation (3.13) and test results.

The curve corresponding to equations (3.13) and (7.1), as well as the results of the tests conducted by Rossignon & Espion (2008), are shown in Figure 7.1. The x-axis was truncated at $l_{geo}^{0.5}$ equal to 40 mm$^{0.5}$, which, for this case, corresponds to an anchorage length of approximately 100 mm. The input data used to plot these curves are characteristic values of the bond line shear strength and fracture energy along with geometrical data, used by Rossignon & Espion (2008), (τ_f=10.5 MPa, G_f=1890 Nm/m^2, A_w=115 x 115 mm^2, E_w=11.6 GPa, A_r=201 mm^2). The Young's modulus of the steel rods, E_r, was not presented, but a value of 205 GPa was assumed.

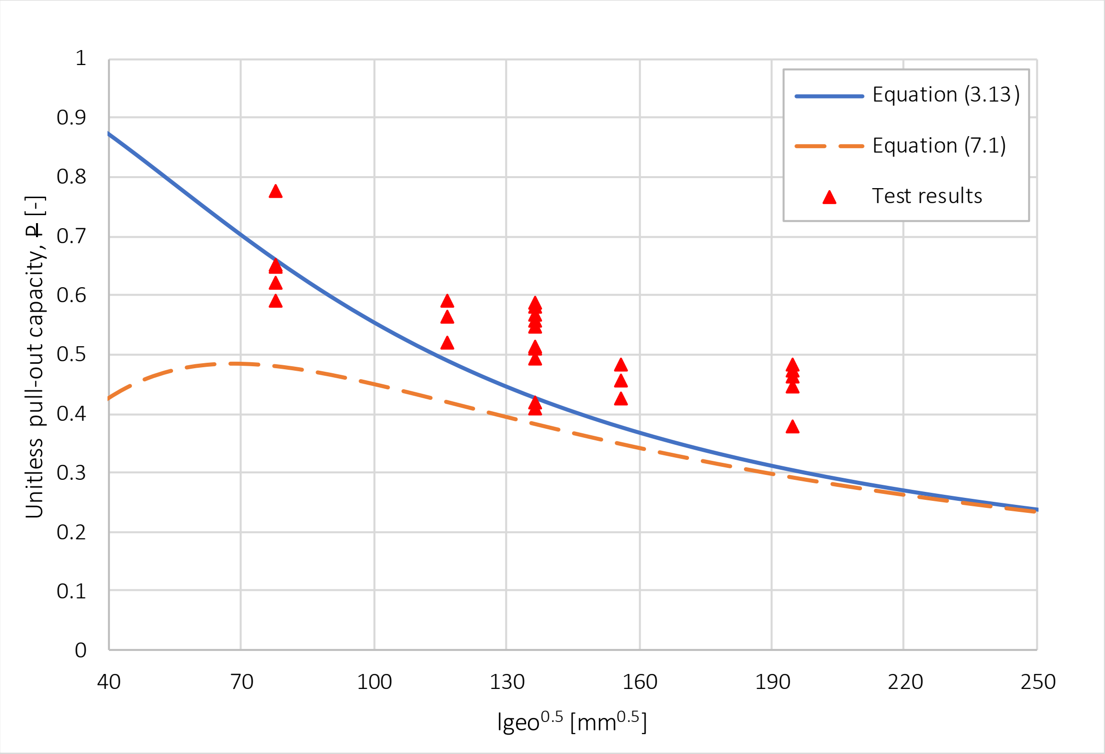

Figure 7.1 A comparison of the existing design equation (3.13) and the modified design equation (7.1), plotted with characteristic bond line properties, as well as test results by Rossignon & Espion (2008). The x-axis was truncated to reflect a span of geometries used in practice.

The modified equation displays a conservative behavior compared to the existing design equation (3.13) and the test results. Further, the difference between the two equations and the test results is presented in Table 7.1.

Table 7.1 Comparison of equation (7.1) and (3.13) against test results for different geometrical lengths. "Min. test" refers to the lowest obtained test result while "avg. test" refers to the mean value of the obtained test results by Rossignon & Espion (2008). Positive values indicate underpredictions while negative values indicate overpredictions.

	Eq. (7.1) vs. min. test		Eq. (7.1) vs. avg. test	
$l_{geo}^{0.5}$ [mm$^{0.5}$]	[-]	[%]	[-]	[%]
78	0.108	22.4	0.177	26.8
117	0.100	24.9	0.139	24.9
137	0.025	6.8	0.135	26.1
156	0.078	23.4	0.107	23.4
195	0.088	31.6	0.157	35.1
	Eq. (3.13) vs. min. test		Eq. (3.13) vs. avg. test	
$l_{geo}^{0.5}$ [mm$^{0.5}$]	[-]	[%]	[-]	[%]
78	-0.069	-10.4	0.000	0.0
117	0.033	6.7	0.071	14.6
137	-0.018	-4.2	0.093	21.8
156	0.050	13.4	0.080	21.2
195	0.077	25.3	0.146	48.3

7.2 Simplification of modified design equation

In an attempt to provide a simple design criterion for practicing engineers, that assimilates the behavior of equation (7.1), an expression, dependent on ω̶, and not expressed with neither hyperbolic nor logarithmic functions, was established:

$$\text{₽} = \frac{a \cdot \text{ω̶}}{b + c \cdot \text{ω̶}^2}, \tag{7.2}$$

where a, b and c are constants. To mimic the behavior of equation (7.1), which diminishes towards zero as ω̶ (and l_{geo}) approaches zero, the constant b was needed. The constants a and c were provided to scale the curve appropriately. Good agreement was found for values of the constants corresponding to a=1, b=1 and c=0.98. In order to further simplify the expression, the constant c was set to 1, thus yielding the following equation (Atashipour et al., 2018):

$$\text{₽} = \frac{\text{ω̶}}{1 + \text{ω̶}^2} \tag{7.3}$$

To investigate the accuracy of the proposed expression, a comparison of the predicted capacity of equation (7.1) and (7.3) is presented in Figure 7.2 along with the existing design proposal (equation (3.13)) and test results.

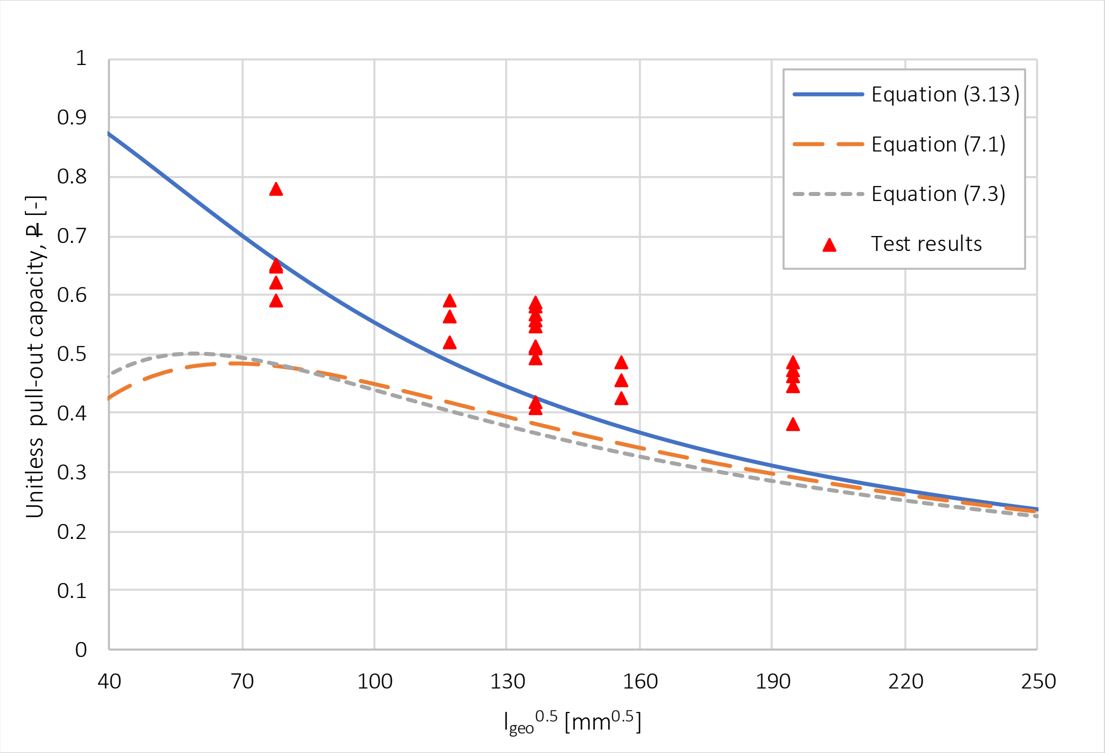

Figure 7.2 A comparison of the different design proposals as well as the test results presented by Rossignon & Espion (2008). The x-axis was truncated to reflect the span of geometries used in practice.

The curves representing equation (7.1) and (7.3) produce similar results. The difference in predicted load bearing capacity, ₽, is schematically illustrated in Figure 7.3.

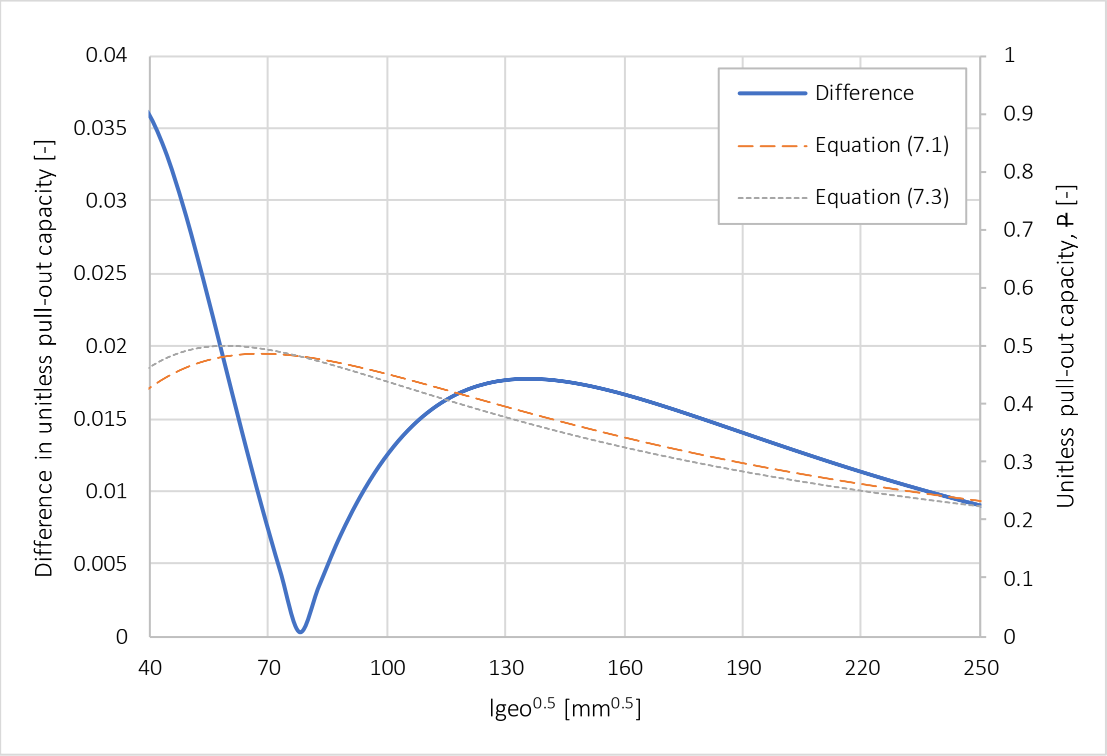

Figure 7.3 The absolute difference in predicted pull-out capacity between equation (7.1) and (7.3) is illustrated by the solid blue line with its y-axis to the left.

Initially, for 40 mm$^{0.5}$ < $l_{geo}{}^{0.5}$ < 75 mm$^{0.5}$, the simplified equation (7.3) is less conservative, and as the geometrical length increases, it becomes more conservative than equation (7.1). The largest difference between the two equations, for values of l_{geo}=40 mm$^{0.5}$, is approximately 0.037.

7.3 Consideration of adhesive type

In order to generate an expression that would be general and practically applicable with regard to different adhesive types and properties, equation (7.3) was further developed by Atashipour et al. (2018),

$$\text{Ᵽ} = \begin{cases} \dfrac{\sqrt{\alpha}}{2} & for \quad \sqrt{\dfrac{l_{geo,min}}{l_m}} \leq \varpi \leq \dfrac{1}{\sqrt{\alpha}}, \\ \dfrac{\alpha \cdot \varpi}{1+\alpha \cdot \varpi^2} & for \quad \varpi > \dfrac{1}{\sqrt{\alpha}} \end{cases} \tag{7.4}$$

where

$$\alpha \leq 3 \tag{7.5}$$

$$l_{geo,min} = l_{geo}(l_a = 100\ mm) \tag{7.6}$$

The coefficient, α, modifies the behavior of the curve after the adhesive type used. This value was empirically concluded to not exceed α=3, in order for equation (7.4) to be conservative compared to equation (3.13). Further, the function is limited by a minimum anchorage length of 100 mm with regard to practical application, thus generating equation (7.6). The influence of α is illustrated in Figure 7.4. Higher values of α, yields a higher prediction of unitless pull-out capacity.

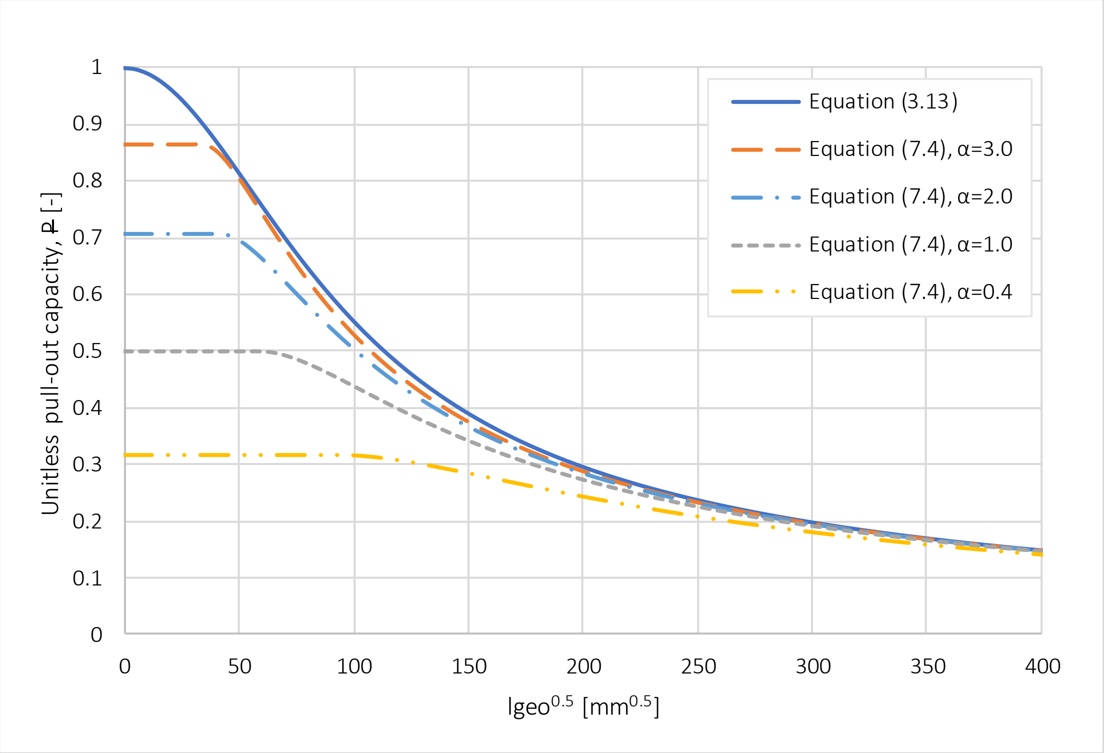

Figure 7.4 Influence of the coefficient, α, on equation (7.4).

Based on the test results for GiR connections, glued with EPX, along with equivalent values for the material parameters, presented by Rossignon & Espion (2008), it is possible to curve fit a value of α that yields predictions close to the lower bound test results. This would, in this case, correspond to a value of α=1.7, see Figure 7.5.

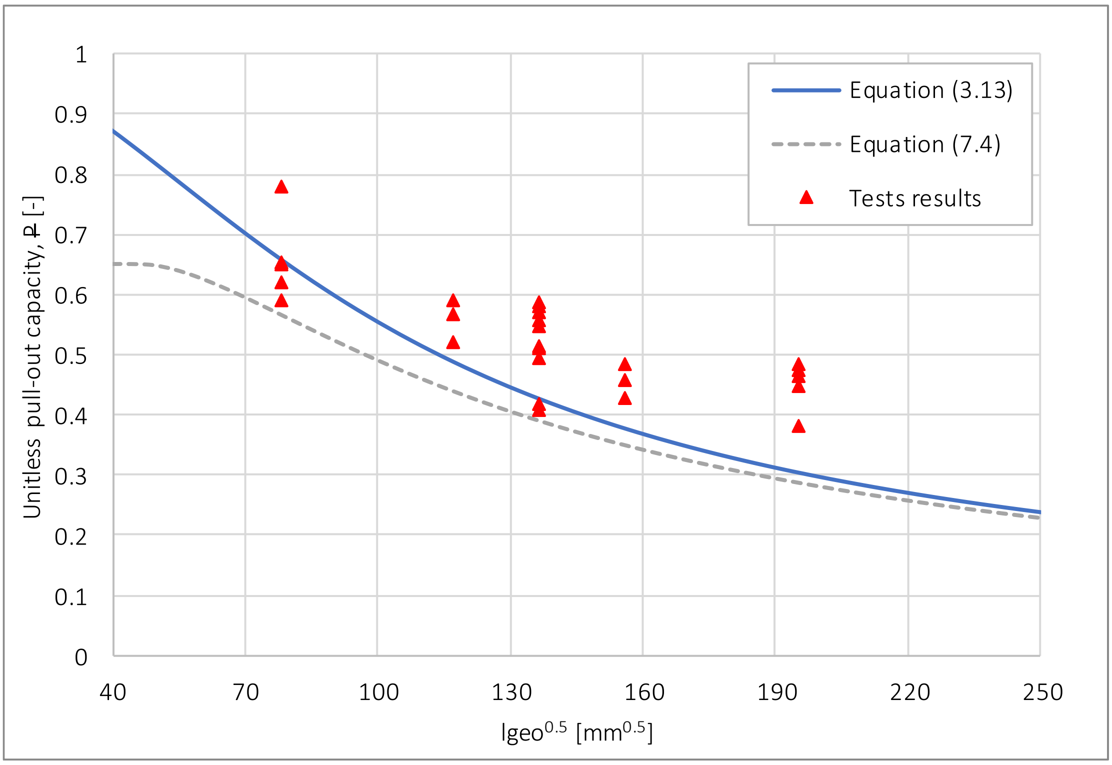

Figure 7.5 The proposed design equation (7.4) with α=1.7 plotted against test results for single GiR connections glued with EPX by Rossignon & Espion (2008). The solid line indicates the existing design proposal, equation (3.13).

7.4 Discussion on the proposed design equation

Equation (7.3) was developed as a simplification of equation (7.1). As a consequence, the prediction of unitless pull-out capacity, Ᵽ, of the expressions, differ. However, this difference is negligible. And while it can be argued that the simplified design equation (7.3) is too conservative, the advantage is its simplicity.

The suggested design equation (7.4) seems to yield conservative predictions of unitless pull-out capacity for GiR connections glued with EPX. The difference between the existing design equation (3.13) and the proposed design equation (7.4) is generally largest for small geometrical lengths, and decreases as l_{geo} increases. This behavior was desired since the predictions of the existing equation was found to overpredict the pull-out capacity for smaller values of l_{geo}, while it generally was more accurate for larger geometrical lengths.

The proposed design approach is dependent on bond line shear strength and fracture energy and the predicted capacity will be highly influenced by these parameters. Thus, it is important to know the corresponding material data of the designed connection. Correct bond line properties, however, are difficult to assess, which ultimately will affect the applicability of the approach. However, this is the case for all approaches derived from Volkersen theory.

The coefficient, α, accounts for the behavior of different adhesive types, and should be experimentally determined. This renders the design equation (7.4) general, as long as α is correctly assessed. For GiR connections glued with EPX, an approximate value of α=1.7 is suggested, based on the lower bound test results presented in (Rossignon & Espion, 2008). However, extensive testing should be conducted in order to ensure the validity of any proposed value of this coefficient.

Finally, and as mentioned by Stepinac et al. (2013), there is a general concern among professionals, that several available design equations underestimate the capacity of glued-in rod connections. This concern could also be raised for equation (3.13) as well as the modified equations (7.3) and (7.4). However, as this project mainly focused on the area where equation (3.13) yielded predictions on the unsafe side, i.e. for short geometrical lengths, the problem of underestimating the pull-out capacity for higher values of l_{geo} was not considered.

8 Conclusions

The aim of this project was to contribute to research of glued-in rod connections in order to establish a reliable design approach for future editions of the European standard for timber structures, Eurocode 5. The aim was fulfilled by achieving the following:

- The most important failure mode of glued-in rod connections was identified as failure in, or in the close proximity of, the timber-adhesive interface. This was true for connections glued with polyurethane or epoxy.
- An axisymmetric finite element model, describing pull-out failure at the timber-adhesive interface, was established and subsequently verified against experimental data and previously performed numerical analyses found in literature.
- An existing design approach, developed by Gustafsson & Serrano (2002), based on Volkersen (shear lag) theory and fracture mechanics, was studied, and the influence of the parameters geometrical length, l_{geo}, and material stiffness ratio, k, was investigated.
- The existing design approach was found to be unconservative, and a modified design equation was suggested.

The following conclusions were drawn regarding the developed axisymmetric finite element model:

- The FE simulations showed that the damage progression starts at the free surface of the connection; and for short anchorage lengths, damage also occurs at the end of the anchorage zone, before failure. However, for longer anchorage lengths, the damage only occurs at the free surface before failure.
- The assumed axisymmetry does not have a significant effect on the pull-out capacity; however, it slightly influences the stiffness of the joint.
- The established axisymmetric FE model provides a simple approach, which in a time efficient way analyses the pull-out capacity of single rod connections.
- The results from simulations of the axisymmetric finite element model showed good agreement with numerical simulations found in literature. The obtained FE results are in good agreement with test results for polyurethane adhesive, while overpredictions were observed for connections glued with epoxy.

The following conclusions were drawn regarding the evaluation of the existing design approach, and the proposed design equation:

- For joints glued with epoxy, the existing design approach is unconservative for small geometrical lengths, and on the safe side for larger geometrical lengths. Whereas, for joints glued with polyurethane, predictions of pull-out capacity are generally on the safe side, for anchorage lengths used in practice ($l_a \geq 100$ mm).
- The proposed design equation, yields pull-out capacities on the safe side for all geometrical lengths and is applicable to use for all types of adhesives, as long as correct values of the coefficient, α, is used.

Suggestions for further studies:

- To further investigate the effect of peel stresses in glued-in rod connections, and ultimately incorporate its influence in a design criterion.

- To study the convergence problems of simulations using the axisymmetric finite element model, with regard to material input, in order to make results of simulations more reliable.
- Since the results of both the finite element simulations and the proposed design equation are highly dependent on bond line strength and fracture energy, an investigation of how to standardize testing procedures and gathering of input data, is of interest.
- To find appropriate values of the coefficient, α, in order to make the proposed design equation generally applicable.

References

Aicher, S. & Dill-Langer, G., 2001. *Influence of moisture, temperature and load duration on performance of glued-in rods.* Stuttgart, Rilem Symposium on Joints in Timber Structures.

Atashipour, S.R., Lundgren, K., Feldt, P., Thelin, A. & Heshmati, M., 2018. A simplified design equation for Glued-in-Rod (GiR) joints. *(Under submission to a conference).*

Beer, F. P., Johnston Jr., R. E., Dewolf, J. T. & Mazurek, D. F., 2012. *Mechanics of Materials.* 6th ed. New York: McGraw-Hill.

Bengtsson, C. & Johansson, C.-J., 2002. *Final Report: GIROD - Glued-in Rods for Timber Structures,* Borås: SP.

Bocciarelli, M., Pierluigi, C., Giulia, F. & Foggi, C., 2008. Prediction of debonding strength of tensile steel/CFRP joints using fracture mechanics and stress based criteria. *Engineering Fracture Mechanics,* pp. 299-313.

Danielsson, H., 2013. *Perpendicular to Grain Fracture Analysis of Wooden Structural Elements - Models and Applications,* Lund: Department of Construction Sciences.

Dassault Systèmes, 2016. *Abaqus Documentation, Abaqus/CAE 2017.* Johnston, RI, USA: Dassault Systèmes Simulia Corporation.

Di Maria, V. & Ianakiev, A., 2015. Adhesive Connections in Timber: A Comparison between Rough and Smooth Wood Bonding Surfaces. *International Journal of Chemical, Molecular, Nuclear, Materials and Metallurgical Engineering,* 9(3), pp. 395-401.

Francescato, P., Pastor, J. & Enab, T., 2005. Torsional Behavior of a Wood-based Composite Beam. *Journal of Composite Materials,* 39(10), pp. 865-879.

Gonçalves, D. J. S., Campilho, R. D. S. G., Da Silva, L. F. M. & Fernandes, J. L. M., 2014. The Use of the Boundary Element Method in the Analysis of Single Lap Joints. *The Journal of Adhesion,* 90(1), pp. 50-64.

Gonzales, E., Tannert, T. & Valle, T., 2016. The impact of defects on the capacity of timber joints with glued-in rods. *International Journal of Adhesion & Adhesives,* Volume 65, pp. 33-44.

Gonzalez, E., Avez, C. & Tannert, T., 2016. Timber Joints with Multiple Glued-in Steel Rods. *The Journal of Adhesion,* 92(7-9), pp. 635-651.

Gowda, C., Kortesmaa, M. & Ranta-Maunus, A., 1996. *Long term creep tests on timber beams in heated and non-heated environments,* Espoo: Technical Research Center of Finland.

Gustafsson, P. J. & Serrano, E., 2002. *Glued-in Rods for Timber Structures - Development of a Calculation Model,* Lund, Sweden: Division of Structural Mechanics, LTH, Lund University.

Gustafsson, P. J., Serrano, E., Aicher, S. & Johansson, C.-J., 2001. *A Strength Design Equation for Glued-in Rods.* Stuttgart, RILEM Symposium on Joints in Timber Structures.

Henkel, 2018. *Hysol® EA 9309NA - Epoxy Paste Adhesive.* Bay Point, California: Henkel Corporation.

Heshmati, M., Haghani, R., Al-Emrani, M. & André, A., 2017. On the strength prediction of adhesively bonded FRP-steel joints using. *Theoretical and Applied Fracture Mechanics,* Volume 93, pp. 64-78.

Loctite, 2015. *Loctite® CR 421 PURBOND - 2K-Polyurethan-System zum Einkleben von Gewindestangen und Betonrippenstählen in tragenden Holzbauteilen.* s.l.:Geistlich Ligamenta.

Riberholt, H., 1988. *Glued Bolts in Glulam - Proposals for CIB Code,* Parksville, Vancover Island: International Council for Building Research Studies and Documentation.

Rossignon, A. & Espion, B., 2008. Experimental assessment of the pull-out strength of single rods bonded in glulam parallel to the grain. *Holz Roh Werkst,* Volume 66, pp. 419-432.

Roylance, D., 2001. *Introduction to Fracture Mechanics,* Cambridge, MA: Massachusetts Institute of Technology.

Serrano, E., 2001a. Glued-in rods for timber structures - An experimental study of softening behaviour. *Materials and Structures,* Volume 34, pp. 228-234.

Serrano, E., 2001b. Glued-in rods for timber structures - a 3D model and finite element parameter studies. *International Journal of Adhesion & Adhesives,* Volume 21, pp. 115-127.

Serrano, E. & Gustafsson, P. J., 2006. Fracture mechanics in timber engineering - Strength analyses of components and joints. *Materials and Structures,* Volume 40, pp. 87-96.

Steiger, R., Gehri, E. & Widmann, R., 2006. Pull-out strength of axially loaded steel rods bonded in glulam parallel to the grain. *Materials and Structures,* 40(1), pp. 69-78.

Steiger, R., Serrano, E., O'Neill, C. & Mcpolin, D., 2015. *Reinforcement with glued-in rods,* Aachen: Shaker Verlag GmbH.

Stepinac, M., Hunger, F., Tomasi, R., Serrano, E., Rajcic, V. & van de Kuilen, J., 2013. *Comparison of design rules for glued-in rods and design rule proposal for implementation in European standards,* Vancouver: International Council for Research and Innovation in Building and Construction.

Stigh, U., Alfredsson, S., Andersson, T., Biel, A., Carlberger, T. & Salomonsson, K., 2010. Some aspects of cohesive models and modelling with special application to strength of adhesive layers. *International Journal of Fracture,* 165(2), pp. 149-162.

Svenskt Trä, 2013. *Att välja trä.* 9th ed. Stockholm: Föreningen Sveriges Skogsindustrier.

Svenskt Trä, 2016. *Limträhandbok Del 1 - Fakta om limträ.* 5th ed. Stockholm: Föreningen Sveriges Skogsindustrier.

Tlustochowicz, G., Serrano, E. & Steiger, R., 2011. State-of-the-art review on timber connections with glued-in steel rods. *Materials and Structures,* 44(5), pp. 997-1020.

Wernersson, H., 1994. *Fracture Characterization Of Wood Adhesive Joints,* Lund: Division Of Structural Mechanics, Lund Unveristy.

Widmann, R., Steiger, R. & Gehri, E., 2007. Pull-out strength of axially loaded steel rods bonded in glulam perpendicular to the grain. *Materials and Structures,* 40(9), pp. 827-838.

Williams, J., 2001. Introduction to linear elastic fracture mechanics. *European Structural Integrity Society,* Volume 28, pp. 3-10.

Volkersen, O., 1938. Die Nietkraftverteilung in Zugbeanspruchten Nietverbindungen mit Konstanten Laschenquerschnitten. *Luftfahrtforschung,* Volume 15, pp. 41-47.

Appendix A – Investigation of Cohesive Stiffness

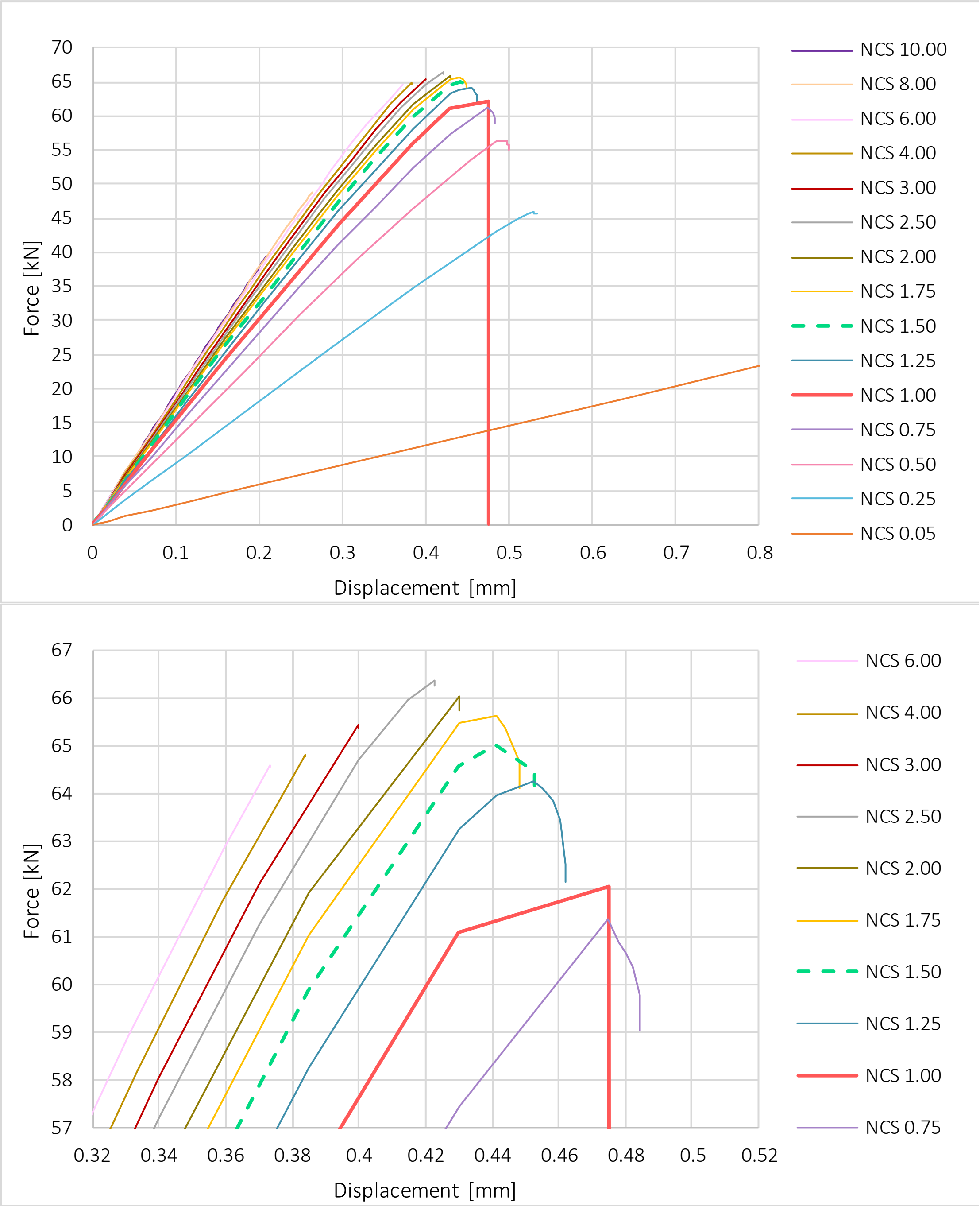

Figure A 1 The force vs displacements for the different cohesive stiffness simulations for PUR with an anchorage length of 160 mm. Run 6, corresponding to a normalized cohesive stiffness of 1.5 times the reference value is marked by the dashed curve.

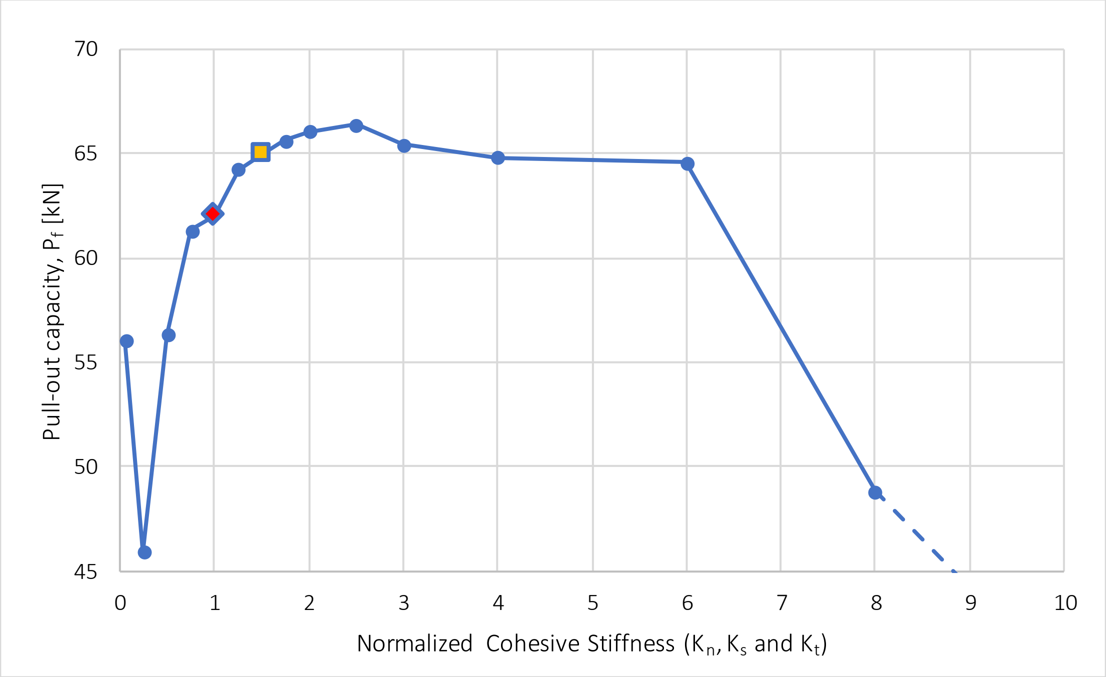

Figure A 2 The predicted pull-out capacity vs normalized cohesive stiffness for PUR with an anchorage length of 160 mm. The reference case is marked by a red diamond. The simulation corresponding to a normalized cohesive stiffness of 1.5 times the reference value is marked by a yellow square.

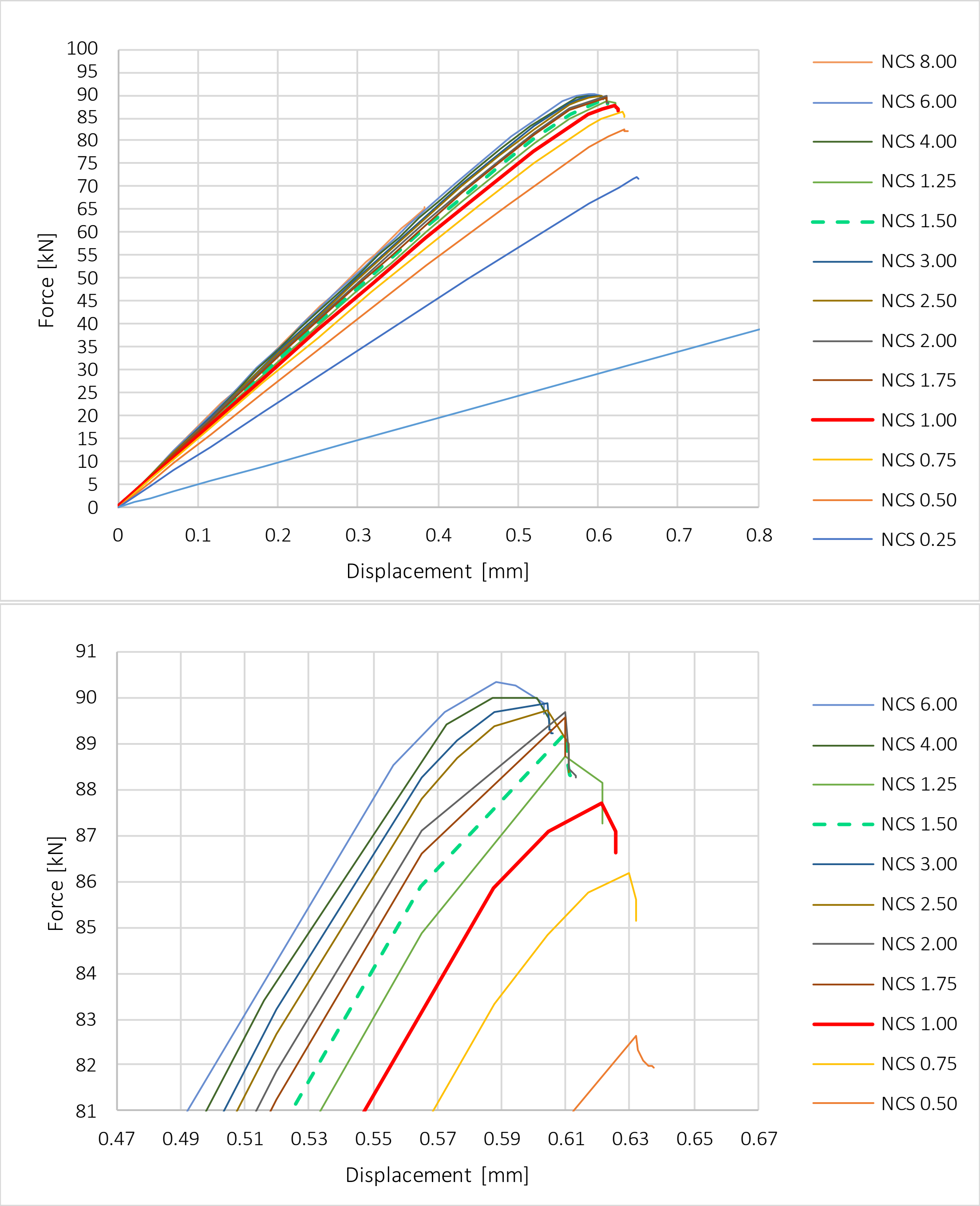

Figure A 3 The force vs displacements for the different cohesive stiffness simulations for PUR with an anchorage length of 320 mm. Run 6, corresponding to a normalized cohesive stiffness of 1.5 times the reference value is marked by the dashed curve.

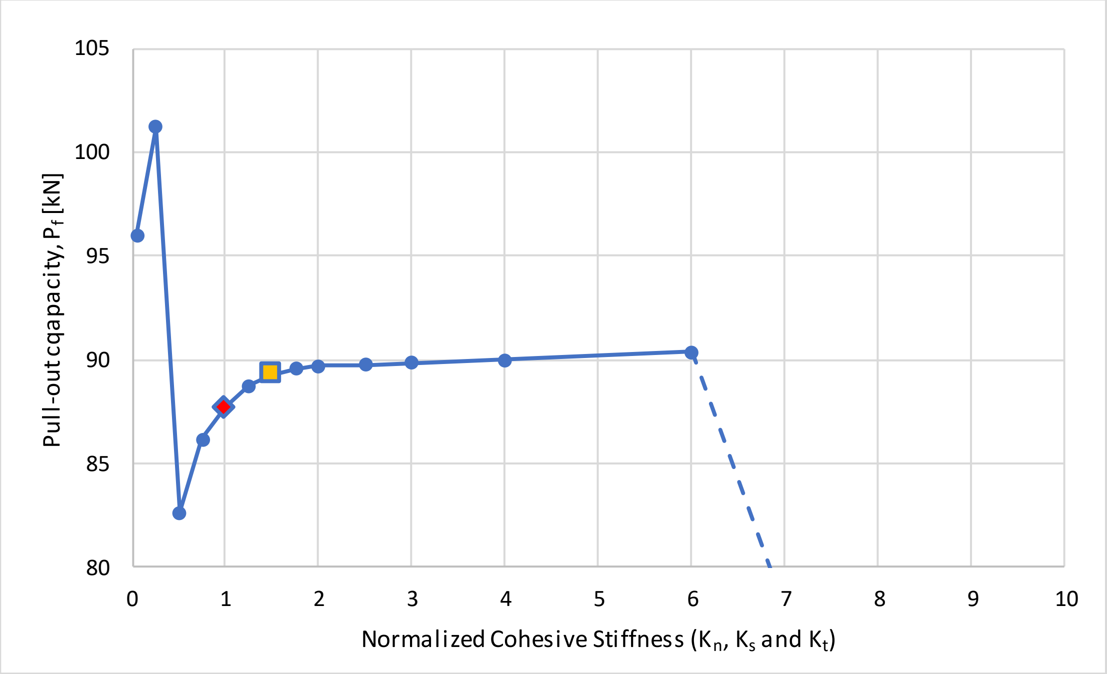

Figure A 4 The predicted pull-out capacity vs normalized cohesive stiffness for PUR with an anchorage length of 320 mm. The reference case is marked by a red diamond. The simulation corresponding to a normalized cohesive stiffness of 1.5 times the reference value is marked by a yellow square.

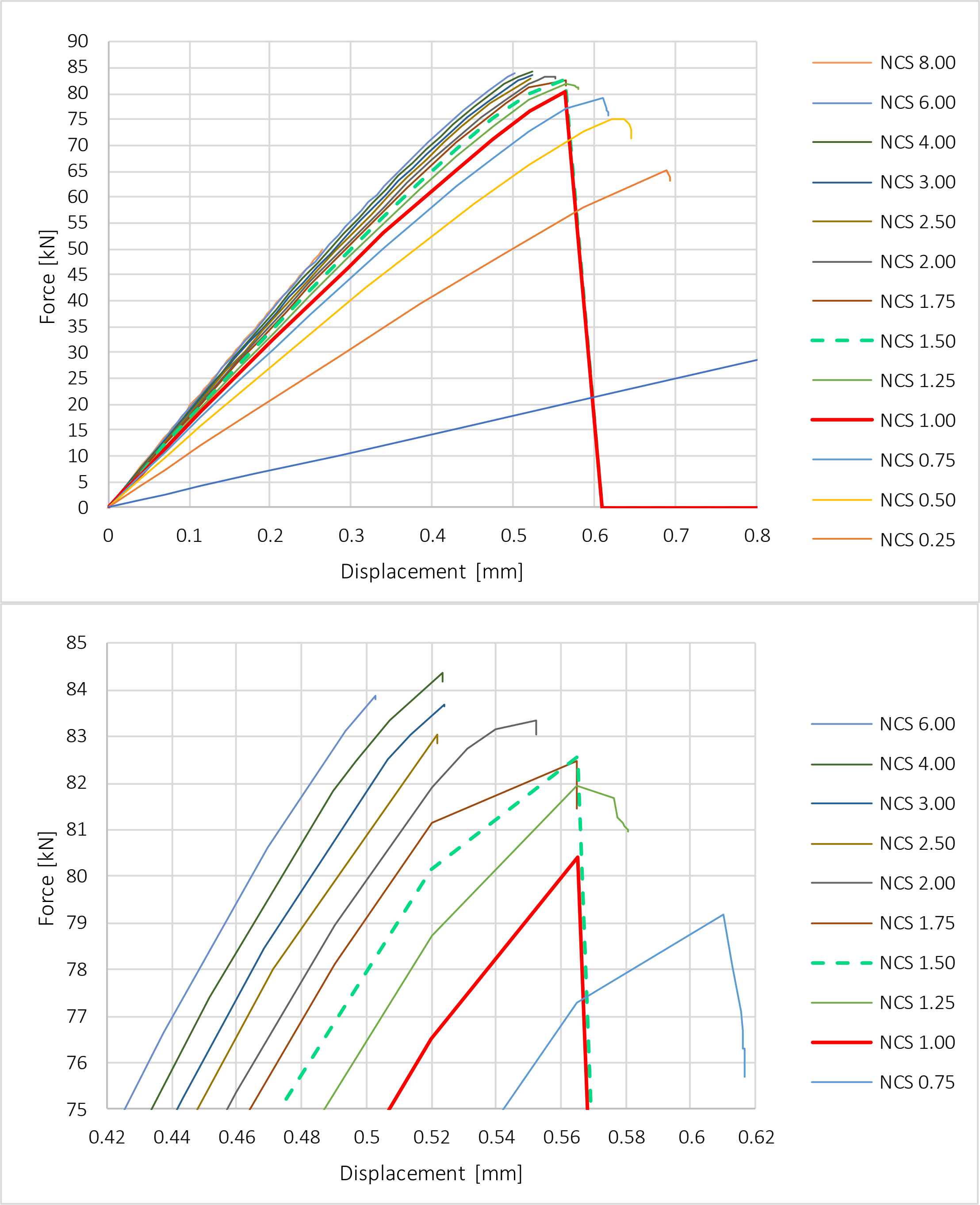

Figure A 5 The force vs displacements for the different cohesive stiffness simulations for EPX with an anchorage length of 160 mm. Run 6, corresponding to a normalized cohesive stiffness of 1.5 times the reference value is marked by the dashed curve.

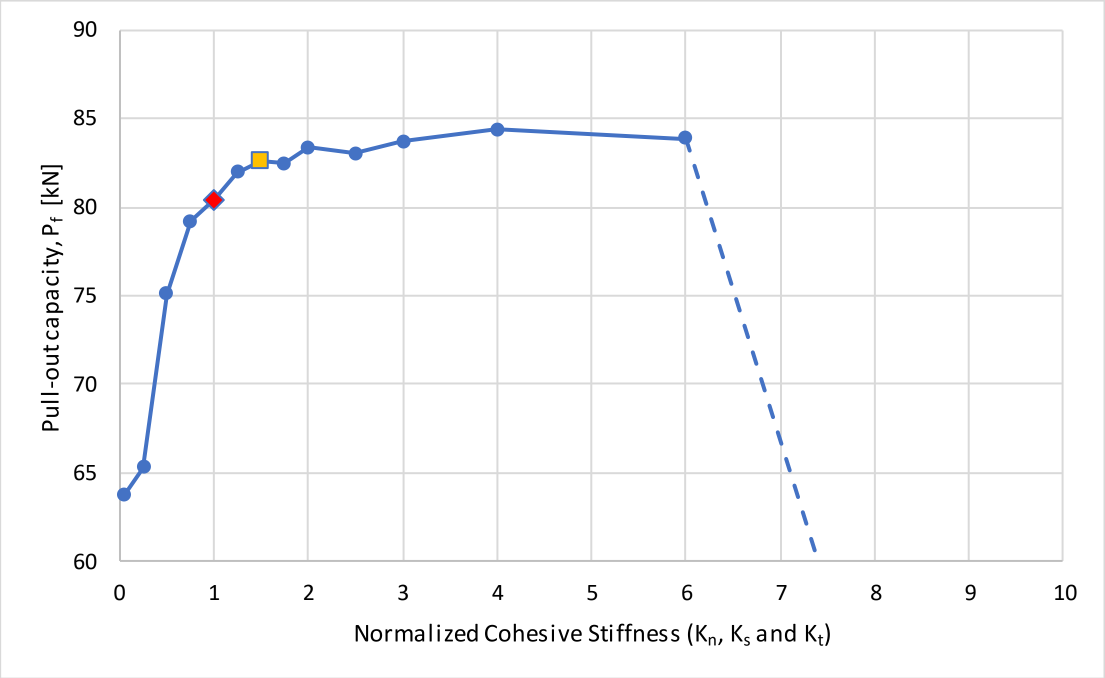

Figure A 6 The predicted pull-out capacity vs normalized cohesive stiffness for EPX with an anchorage length of 160 mm. The reference case is marked by a red diamond. The simulation corresponding to a normalized cohesive stiffness of 1.5 times the reference value is marked by a yellow square.

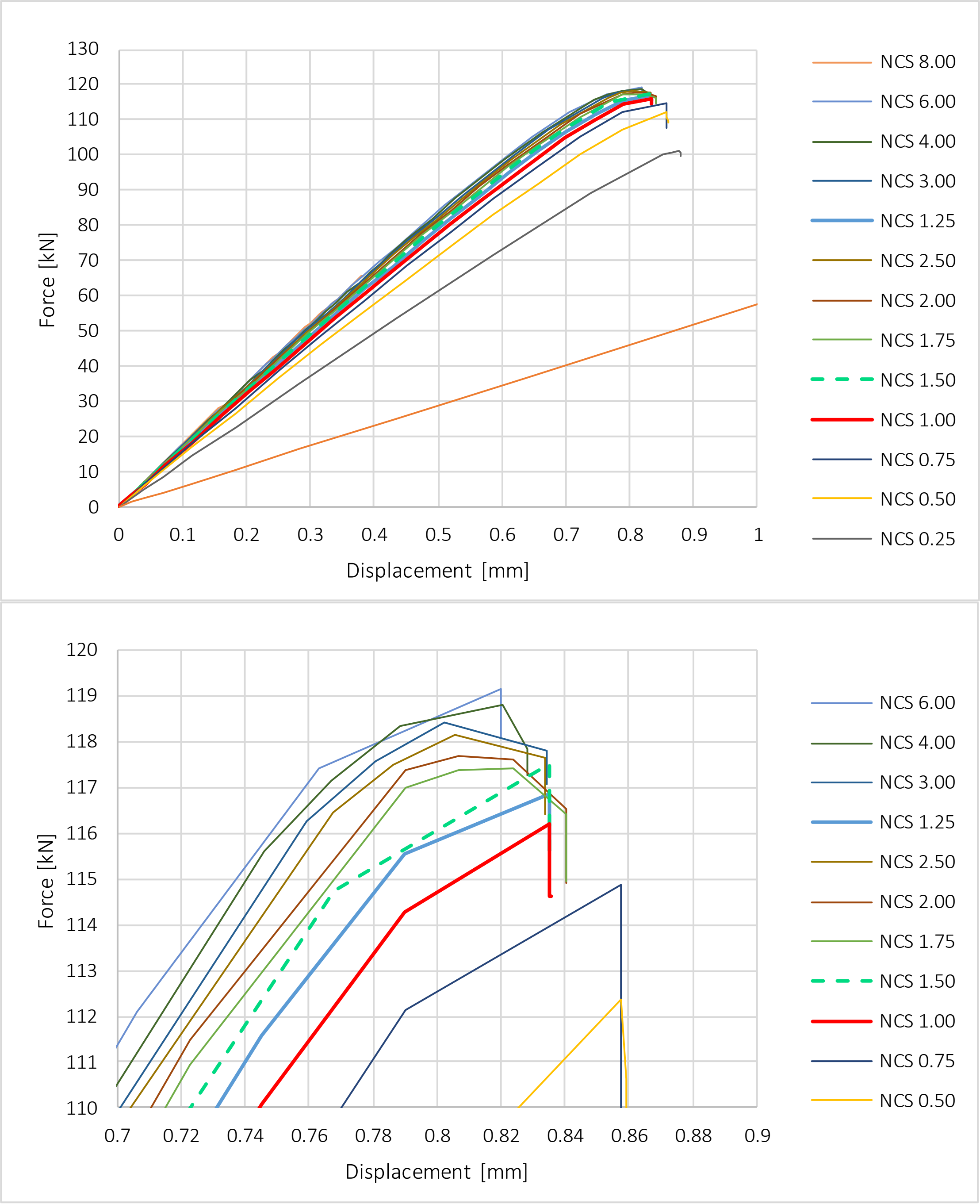

Figure A 7 The force vs displacements for the different cohesive stiffness simulations for EPX with an anchorage length of 320 mm. Run 6, corresponding to a normalized cohesive stiffness of 1.5 times the reference value is marked by the dashed curve.

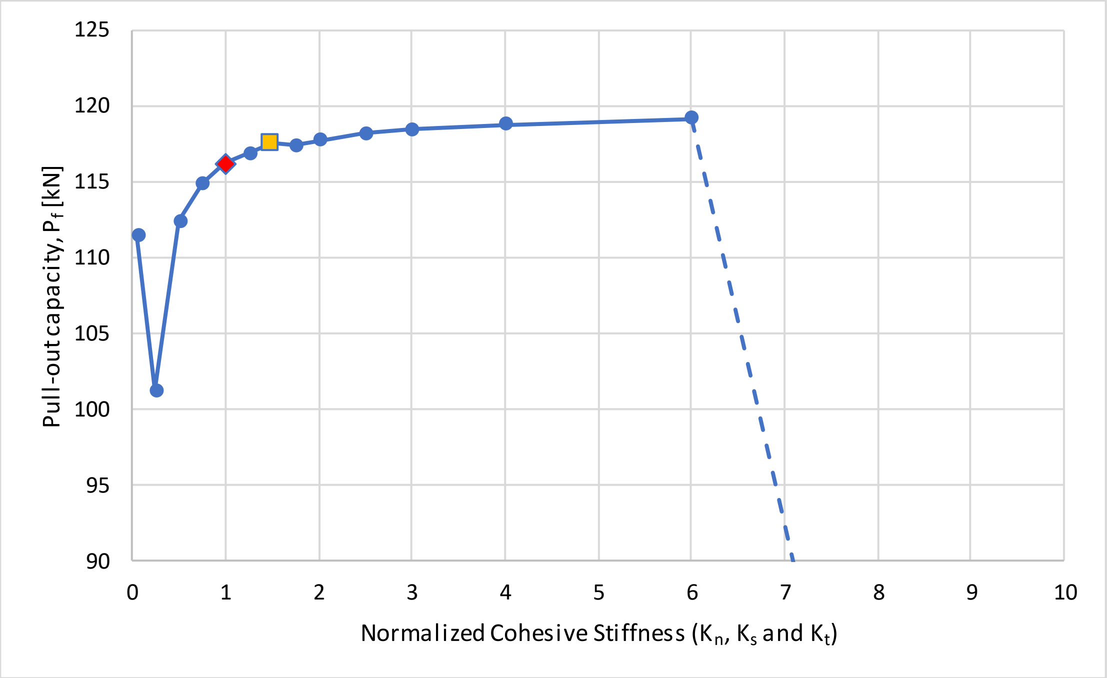

Figure A 8 The predicted pull-out capacity vs normalized cohesive stiffness for EPX with an anchorage length of 320 mm. The reference case is marked by a red diamond. The simulation corresponding to a normalized cohesive stiffness of 1.5 times the reference value is marked by a yellow square.

Appendix B – Overview of Mesh Configurations

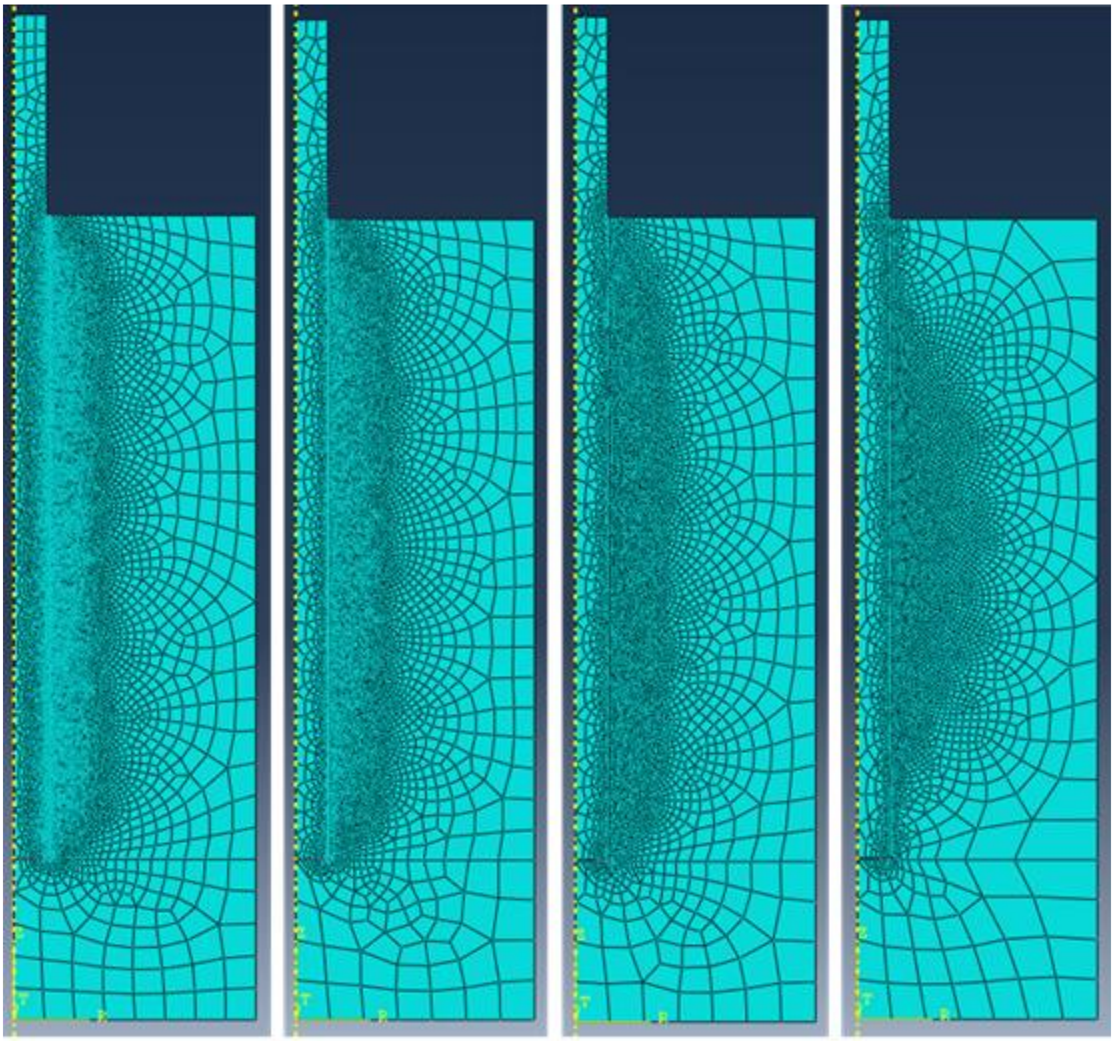

Fine
48.7k
elements

Coarse
21.0k
elements

Coarser
9.1k
elements

Coarsest
6.1k
elements

Figure B 1 The four different mesh densities used for investigation of the influence of mesh density.

Appendix C – Derivation of Correction Factor

The concept of the following derivation of the correction factor, *$1/(1-e^{\varpi})$*, have been presented in (Bocciarelli et al., 2008).

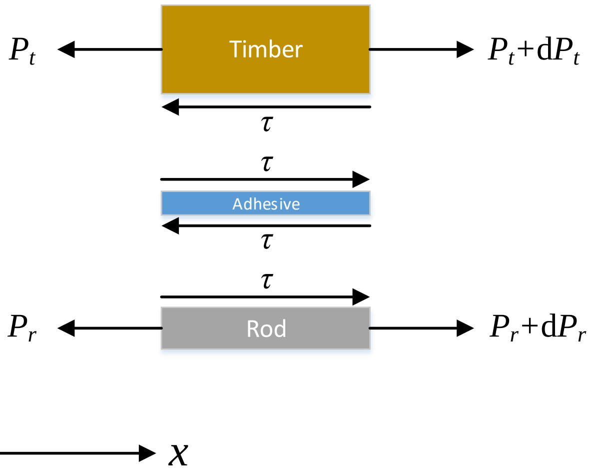

Figure C 1 A differential element of the specimen under loading.

Equilibrium equation:

$$P_r + P_t = P_0 \tag{C.1}$$

Axial strain in each part:

$$\begin{aligned} \mathrm{d}\delta_r &= \frac{P_r \mathrm{d}x}{EA_r} \\ \mathrm{d}\delta_t &= \frac{P_t \mathrm{d}x}{EA_t} \end{aligned} \tag{C.2}$$

Shear strain in the adhesive:

$$\tau = G_a \gamma_a = \frac{G_a}{t_a}(\delta_t - \delta_r) \tag{C.3}$$

Differentiation of the above equation, one time, and substituting equation (C.2):

$$\tau' = \frac{G_a}{t_a}\left(\frac{P_t}{EA_t} - \frac{P_r}{EA_r}\right) \tag{C.4}$$

Also, the equilibrium condition of the timber differential element as well as the rod differential element result in:

$$\tau = \frac{1}{\pi d} P_t' \tag{C.5}$$

$$\tau = -\frac{1}{\pi d} P_r' \tag{C.6}$$

Replacing equations (C.1) and (C.5), after one times differentiating, into equation (C.4):

$$P_t'' - \omega^2 P_t = -\frac{\pi d G_a}{t_a}\frac{P_0}{EA_r} \tag{C.7}$$

where

$$\omega = \sqrt{\frac{\pi d G_a}{t_a}\left(\frac{1}{EA_r} + \frac{1}{EA_t}\right)} \tag{C.8}$$

Solution of the above equation:

$$P_t = c_1 \exp(-\omega x) + c_2 \exp(\omega x) + \frac{EA_t P_0}{EA_t + EA_r} \tag{C.9}$$

For a sufficiently long anchorage length, the shear stress suddenly decreases, and obviously the last term in the solution (C.9) must vanish; (i.e. $c_3=0$):

$$P_t = \frac{EA_t P_0}{EA_t + EA_r} + c_1 \exp(-\omega x) \tag{C.10}$$

And consequently, from equation (C.1):

$$P_r = \frac{EA_r P_0}{EA_t + EA_r} - c_1 \exp(-\omega x) \tag{C.11}$$

Also, at the edge location of the connection ($x = 0$), the axial force in rod is equal to $P_r=P_0$, whereas $P_t=0$ should be zero. Any of these two conditions requires to set:

$$c_1 = -\frac{EA_t P_0}{EA_t + EA_r} \tag{C.12}$$

Substituting equation (C.12) into equations (C.10) and (C.1):

$$P_t = \frac{EA_t P_0}{EA_t + EA_r}\left[1 - \exp(-\omega x)\right] \tag{C.13}$$

$$P_r = \frac{EA_r P_0}{EA_t + EA_r}\left[1 + \frac{EA_t}{EA_r}\exp(-\omega x)\right] \tag{C.14}$$

Now, differentiating any of equations (C.5) or (C.6) one time and replacing the results into equation (C.13) or (C.14) lead to the shear stress distribution at the adhesive near the edge as follows:

$$\tau = \frac{\omega EA_t P_0}{\pi d (EA_t + EA_r)} \exp(-\omega x) = \tau_{\max} \exp(-\omega x) \tag{C.15}$$

In a similar manner, one can write an expression for the shear stress distribution near the end of the anchorage (i.e. at $x = L$), as follows:

$$\tau^{*} = \frac{\omega E A_r P_0}{\pi d (E A_t + E A_r)} \exp[-\omega(L-x)] = \tau^{*}_{\max} \exp[-\omega(L-x)] \tag{C.16}$$

Therefore, the complete shear stress function may be represented as summation of equations (C.15) and (C.16):

$$\tau_{\text{adhesive}} = \tau + \tau^{*} \tag{C.17}$$

It is expected that the adhesive shear stress resultant around the steel bar to be equivalent to the pull-out load P_0. However, the integration of the shear stress gives:

$$\int_0^L \pi d \tau_{\text{adhesive}} \mathrm{d}x = [1-\exp(-\omega L)]P_0 = \alpha P_0 \tag{C.18}$$

For a long anchorage length, equation (C.18) is equivalent to P_0, but not for a small length. To get the exact value P_0 from Eq. (C.18), the shear stress function should be modified using the coefficient $1/(1-e^{\varpi})$.